Full Vehicle State Estimation Using a Holistic Corner-based Approach

by

Ehsan Hashemi

A thesis
presented to the University of Waterloo
in fulfillment of the
thesis requirement for the degree of
Doctor of Philosophy
in
Mechanical and Mechatronics Engineering

Waterloo, Ontario, Canada, 2017

Examining Committee Membership The following served on the Examining Committee for this thesis. The decision of the Examining Committee is by majority vote.

External Examiner	NAME: Goldie Nejat Title: Associate Professor, Mechanical Engineering
Supervisor(s)	NAME: Amir Khajepour Title: Professor, Mechanical Engineering
Internal Member	NAME: William M. Melek Title: Professor, Mechanical Engineering
Internal Member	NAME: Baris Fidan Title: Associate Professor, Mechanical Engineering
Internal-external Member	NAME: Dana Kulic Title: Associate Professor, Electrical Engineering

I hereby declare that I am the sole author of this thesis. This is a true copy of the thesis, including any required final revisions, as accepted by my examiners.

I understand that my thesis may be made electronically available to the public.

Abstract

Vehicles' active safety systems use different sensors, vehicle states, and actuators, along with an advanced control algorithm, to assist drivers and to maintain the dynamics of a vehicle within a desired safe range in case of instability in vehicle motion. Therefore, recent developments in such vehicle stability control and autonomous driving systems have led to substantial interest in reliable road angle and vehicle states (tire forces and vehicle velocities) estimation. Advances in applications of sensor technologies, sensor fusion, and cooperative estimation in intelligent transportation systems facilitate reliable and robust estimation of vehicle states and road angles. In this direction, developing a flexible and reliable estimation structure at a reasonable cost to operate the available sensor data for the proper functioning of active safety systems in current vehicles is a preeminent objective of the car manufacturers in dealing with the technological changes in the automotive industry.

This thesis presents a novel generic integrated tire force and velocity estimation system at each corner to monitor tire capacities and slip condition individually and to address road uncertainty issues in the current model-based vehicle state estimators. Tire force estimators are developed using computationally efficient nonlinear and Kalman-based observers and common measurements in production vehicles. The stability and performance of the time-varying estimators are explored and it is shown that the developed integrated structure is robust to model uncertainties including tire properties, inflation pressure, and effective rolling radius, does not need tire parameters and road friction information, and can transfer from one car to another.

The main challenges for velocity estimation are the lack of knowledge of road friction in the model-based methods and accumulated error in kinematic-based approaches. To tackle these issues, the lumped LuGre tire model is integrated with the vehicle kinematics in this research. It is shown that the proposed generic corner-based estimator reduces the number of required tire parameters significantly and does not require knowledge of the road friction. The stability and performance of the time-varying velocity estimators are studied and the sensitivity of the observers' stability to the model parameter changes is discussed. The proposed velocity estimators are validated in simulations and road experiments with two vehicles in several maneuvers with various driveline configurations on roads with different friction conditions. The simulation and experimental results substantiate the accuracy

and robustness of the state estimators for even harsh maneuvers on surfaces with varying friction.

A corner-based lateral state estimation is also developed for conventional cars application independent of the wheel torques. This approach utilizes variable weighted axles' estimates and high slip detection modules to deal with uncertainties associated with longitudinal forces in large steering. Therefore, the output of the lateral estimator is not altered by the longitudinal force effect and its performance is not compromised. A method for road classification is also investigated utilizing the vehicle lateral response in diverse maneuvers.

Moreover, the designed estimation structure is shown to work with various driveline configurations such as front, rear, or all-wheel drive and can be easily reconfigured to operate with different vehicles and control systems' actuator configurations such as differential braking, torque vectoring, or their combinations on the front or rear axles. This research has resulted in two US pending patents on vehicle speed estimation and sensor fault diagnosis and successful transfer of these patents to industry.

Acknowledgements

First and foremost, I would like to thank my supervisor, Prof. Amir Khajepour, for his support, expertise, passion for research, encouragement, and guidance.

I also would like to acknowledge the financial support of Automotive Partnership Canada, Ontario Research Fund and General Motors. Special thanks to Dr. Bakhtiar Litkouhi, Dr. Shih-ken Chen, and Dr. Alireza Kasaiezadeh in GM Research and Development Center in Warren, MI, for their technical support and valuable inputs. I'd like to thank the technicians in the Mechatronic Vehicle Systems laboratory, Jeff Graansma, Jeremy Reddekopp, and Kevin Cochran for helping me in the road experiments.

I am deeply grateful to my friends and my family whose support is truly appreciated. Most importantly, none of this would have been possible without the love and patience of my wife, Pegah Pezeshkpour, and the many years of her support that provided the foundation for this work. My special thanks to my gorgeous son whose love has been my motivation throughout this endeavor.

My whole experience would not have been as rewarding without the help of my colleagues, Mohammad Pirani, Milad Jalalaiyazdi, Saeid Khosravani, and Reza Zarringhalam, for their technical assistance and the stimulating discussions.

Table of Contents

List of Tables x

List of Figures xi

1 Introduction 1

1.1 Motivation 1

1.2 Objectives 3

1.3 Thesis Outline 5

2 Literature Review and Background 7

2.1 Tire Forces 7

2.2 Tire Force Estimation 11

2.3 Vehicle Velocity Estimation 13

2.4 Road Angles and Condition Estimation 15

3 Estimation of the Road Angles 18

3.1 Introduction 18

3.2 Sprung Mass Kinematics 19

3.3 Unknown Input Observer for Road Angle Estimation 22

3.4 Road-Body Kinematics . . . 27
3.5 Experimental Results . . . 30
3.6 Summary . . . 36

4 Tire Force Estimation **37**
4.1 Introduction . . . 37
4.2 Longitudinal Force Estimation . . . 40
4.2.1 Observer-based force estimation . . . 40
4.2.2 Kalman-based force estimation . . . 42
4.3 Lateral Force Estimation . . . 44
4.4 Vertical Force Estimation . . . 46
4.5 Simulation and Experimental Results . . . 49
4.5.1 Longitudinal force estimator . . . 50
4.5.2 Lateral and vertical force estimators . . . 54
4.6 Summary . . . 57

5 Vehicle Velocity Estimation **58**
5.1 Introduction . . . 59
5.2 Longitudinal Velocity Estimation . . . 60
5.3 Lateral Velocity Estimation . . . 67
5.3.1 Lateral state estimation for conventional cars . . . 71
5.4 Road Classification based on Lateral Dynamics . . . 79
5.5 Simulation and Experimental Results . . . 87
5.5.1 Longitudinal and lateral velocity estimators . . . 88
5.5.2 Lateral velocity estimator for conventional vehicles . . . 99
5.5.3 Road classification based on vehicle lateral response . . . 102
5.6 Summary . . . 106

6 Conclusions and Future Work **108**

6.1 Conclusions and Summary 108

6.2 Future Work 111

References **114**

A Parameter Identification and Proofs **128**

List of Tables

3.1 Parameters of the Test Vehicles for Experiments 30

4.1 Force Estimators' Error *NRMS* 56

5.1 Velocity Estimators' Error *NRMS* for AWD and RWD Configurations . . . 102

List of Figures

1.1 Vehicle state estimator and HVC controller 3

2.1 Pure-slip LuGre tire model, normalized forces (a) longitudinal (b) lateral . 10
2.2 Combined-slip LuGre model, normalized tire forces (a) longitudinal (b) lateral 11

3.1 The proposed structure for the road angle estimation 19
3.2 Height sensors and sprung mass kinematics 20
3.3 Roll and pitch models with the road angles 22
3.4 Experimental setup (a) the I/O and hardware layout (b) AWD test vehicle 31
3.5 Acceleration and suspension height measurements on the graded road. . . . 32
3.6 Estimation results for *Case1*, (a) vehicle angles (b) road grade. 33
3.7 Acceleration and suspension height measurements on the banked road. . . 33
3.8 Estimation results for *Case2*, (a) vehicle angles (b) bank angle 34
3.9 Acceleration and suspension height measurements on combined grade/bank 35
3.10 Road experiments, (a) estimated vehicle angles on combined grade/bank (b) estimated road angles 35

4.1 Forces and velocities in (a) planar vehicle model (b) tire coordinates. . . . 39
4.2 Corner-based force estimation structure 40
4.3 (a) pitch model (b) roll model 48

4.4 (a) Electric motors (b) wheel hub sensors for force/moment measurement. . 49
4.5 Simulation results, estimated forces in CarSim (a) acceleration/brake on a road with $\mu = 0.3$ (b) AiT on a slippery road with $\mu = 0.25$ (c) AiT on dry asphalt. 51
4.6 Lane change with brake on wet, AWD vehicle (a) estimated $\hat{F}_x$ at rL (b) wheel torques (c) wheel speeds (d) steering wheel angle, δ_{sw}. 52
4.7 DLC on snow with AWD test vehicle (a) estimated $\hat{F}_x$ at rL (b) rear wheel torques (c) rear wheel speeds (d) steering wheel angle. 52
4.8 BiT and acceleration on snow for FWD case (a) estimated forces at fR with UIO (b) front wheel torques (c) rear wheel speeds (d) steering wheel angle. 53
4.9 Lateral and vertical force estimation, LC for AWD on a dry surface. 54
4.10 Lateral and vertical force estimates, steering on ice then packed snow. . . . 55

5.1 Corner-based state estimation structure 60
5.2 Time-varying observer gains for velocity estimators. 65
5.3 Response of the observer with time-varying gains. 65
5.4 Sensitivity of $\mathcal{SM}$ of the Long. and Lat. error dynamics to model parameters. 70
5.5 Sensitivity of $\mathcal{SM}$ of the longitudinal/lateral error dynamics to σ_{1q}. 70
5.6 Sensitivity of $\mathcal{H}_\infty$ of the Long. and Lat. error dynamics to model parameters. 71
5.7 *Test1* for various road tests, experimental results 75
5.8 *Test2* for different driving scenarios and roads, experimental results 76
5.9 Pure-slip LuGre lateral tire model 80
5.10 Normalized lateral forces, combined-slip model, on a dry road $\theta = 1$ with longitudinal speed $V_x = 20\,[m/s]$. 82
5.11 The structure of the road classifier based on the vehicle's lateral response. . 84
5.12 The general structure of the vehicle state and road angle/condition estimation 86
5.13 Experimental setup (a) hardware layout (b) RWD test vehicle 87

5.14 Estimated Long. velocity in SS and AiT on dry/slippery roads, CarSim. . 88
5.15 Estimated velocities and wheel speeds for AWD, split-μ on ice and dry. . . 89
5.16 Estimated velocities and wheel speeds for AWD, launch on a wet sealer. . . 90
5.17 Longitudinal velocity estimates for the AWD case, LC and steering on snow. 91
5.18 Velocity estimates for LC on snow/ice, for AWD configuration. 91
5.19 Velocity estimates for oval steering with pulsive traction on dry, RWD. . . 92
5.20 Lateral velocity estimates for RWD test vehicle, LC on combined dry/wet. 93
5.21 Lateral velocity estimates for AiT on dry asphalt, AWD configuration. . . 94
5.22 Wheel speed and estimated/measured velocities at wheel centers, AiT on dry. 94
5.23 Launch and AiT on wet sealer and wet asphalt with transition to dry for FWD (a) estimated speed (b) accelerations (c) yaw rate. 95
5.24 Wheel speed and estimated/measured velocities at wheel centers (Wheel C.) for (a) launch on wet sealer then dry (b) AiT on wet/dry, FWD. 96
5.25 Large left turn (TL) with acceleration in RWD configuration on wet/dry. . 97
5.26 Velocity estimates for AWD, BiT on snow and steering on packed snow/ice. 98
5.27 Wheel speed and estimated/measured velocities at wheel centers (Wheel C.) for (a) steering on packed snow/ice (b) BiT and acceleration on snow . . . 98
5.28 Lateral velocity estimates for AWD in an LC on packed snow and ice. . . . 99
5.29 Lateral velocity estimates for FT on dry/wet, RWD 100
5.30 Lateral velocity estimates for DLC on snow, AWD 101
5.31 Road classifier results and measurements for a full turn on dry asphalt, AWD 103
5.32 AiT with high slip on dry asphalt, road classification for AWD 104
5.33 Road classification results for AWD case in an LC on packed snow and ice 104
5.34 Full turns on dry/wet with the AWD vehicle, road classification results . . 105
5.35 AWD vehicle in full turns on dry/wet sealer 106
5.36 Road classification for a mild sine steering on dry asphalt, AWD 106

A.1 Tuned lateral LuGre tire curve based on tire data from CarSim 128

Chapter 1

Introduction

1.1 Motivation

Cars will become vastly safer and more intelligent through the availability of new technologies in sensors, actuators, vehicle dynamic control, and autonomous systems. Studies show that utilizing safety systems such as active Vehicle Dynamics Control (VDC) and Traction Control System (TCS) plays an essential role in stability of vehicles on various road conditions with different speed (for example [1–5]), thus reducing the severity of vehicle accidents. In 2014 the National Highway and Traffic Safety Administration in U.S. estimated VDC (so called Electronic Stability Control, ESC) has saved close to 4000 lives during the 5-year period 2008 to 2012 and would prevent 156000 to 238000 injuries for the period in all types of crashes [6]. The United States Insurance Institute for Highway concluded that vehicles' active safety systems reduce the likelihood of deadly single-vehicle crashes by 58% and single-vehicle rollovers by 79%. Transport Canada has also introduced the new Canada Motor Vehicle Safety Standard 126 which requires a VDC (or ESC) system on all passenger vehicles with a gross weight of 4536 kg or less, and manufactured on or after September 1st, 2011.

Examples of VDC systems already present in passenger vehicles include: anti-lock braking systems, traction control, differential braking, torque vectoring, and active steering. These systems require vehicle states (sideslip angle and speed) and individual tire states

(slip ratio, slip angle, and forces) for robust stability of a vehicle. This need is even more pronounced in a fully autonomous driving system where a human driver is completely out of the vehicle control loop.

Tire forces affect the vehicle's capacity to perform requested maneuvers and can be measured directly with wheel hub sensors; however, such sensors cost tens of thousands of dollars, which prohibits their use in production vehicles. On the other hand, force calculation at each corner (wheel) based on a tire model requires road friction information. Thereby, even accurate slip ratio/angle information from a high precision GPS does not result in forces at each tire. Estimation of longitudinal and lateral tire forces is therefore required. In the literature, these have been estimated using Kalman-based, nonlinear, sliding mode, and unknown input observers. Force estimators are then assimilated with velocity observers to provide inputs to active safety systems of traditional and autonomous vehicles.

Information about longitudinal and lateral velocities is significant contributor in traction and stability control systems. They can be measured with GPS, however, poor accuracy and low bandwidth of available commercial GPSs, particularly for measuring velocity in the lateral direction, and loss of reception and reliability in road tunnels or in urban canyons are primary impediments to their use for active vehicle safety systems. Therefore, reliable velocity estimation that is robust to changing road and environmental conditions, and variations in model parameters have been a major focus in recent research on vehicle stability control and autonomous driving systems.

Figure 1.1 illustrates motivation for having vehicle states in a structure of the integrated holistic vehicle control (HVC)-Estimator.

Two major approaches have been adopted in the literature to tackle velocity estimation problems. One is the modified kinematic-based approach, which implements stochastic estimators or nonlinear observers using acceleration/yaw rate measurements from the Inertial Measurement Unit (IMU). This method does not need tire model information, but instead sensor bias and noise need to be identified precisely to obtain reliable outcomes. Moreover, this approach requires a method to cope with low-excitation cases, which bring about erroneous estimations. To improve estimation results and address low excitation scenarios, kinematic-based methods could benefit from GPS measurements if reliable data is available.

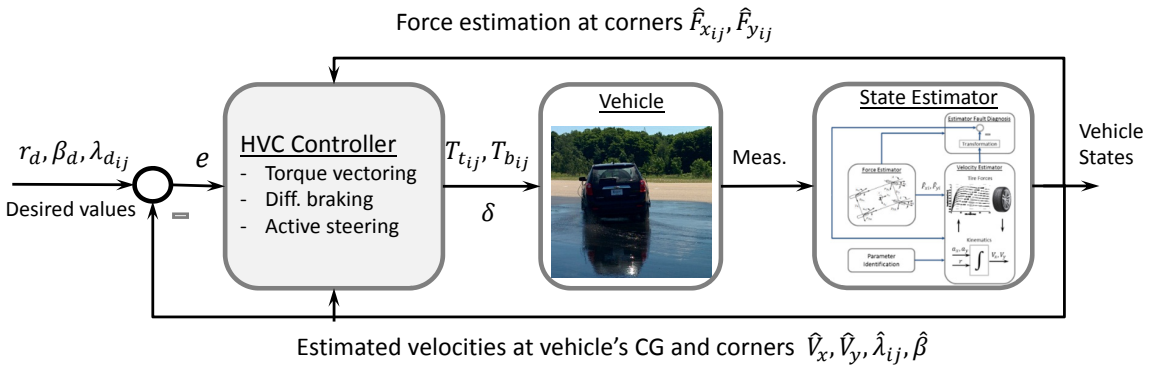

Figure 1.1: Vehicle state estimator and HVC controller

The other velocity estimation practice is model-based and utilizes IMU data (acceleration/yaw rate measurements) and corrects the estimation with tire forces using sliding mode, nonlinear, and stochastic observers. Although this approach seems promising, it requires accurate tire parameters and a good perception of road friction, especially for the tires saturation region, which is not practically feasible. Therefore, developing a holistic corner-based vehicle state estimator using conventional sensor measurement robust to the road friction changes and model uncertainties is desirable and is addressed in this research by designing observers for the consequent time-varying models.

Road grade and bank angles considerably affect the vehicle dynamics and measured accelerations, thus play a key role in the vehicle state estimation and stability. Thereby, road angle estimation is an inherent part of state of the art vehicle state estimators and is tackled in this thesis by implementing unknown input observers on vehicle pitch and roll dynamics.

1.2 Objectives

The main objective of this thesis is to develop a generic corner-based estimation of the vehicle states and road angles robust to the road friction conditions regardless of the vehicles driveline configuration (FWD, RWD, AWD). The following are detailed objectives of this thesis to provide vehicle states and road angles for VDC systems:

The first objective of this thesis is real-time estimation of the road and vehicle angles without using road friction and tire force information. Road and vehicle angles are crucial in accurate estimation of tire forces, vehicle speeds, and hence in longitudinal and lateral slip calculations. The road-body kinematics should be employed to relate the vehicle's frame, body, and road angles and to increase the accuracy. An Unknown input observer module is introduced in this thesis which uses estimated vehicle angles and their rates for the bank/grade estimation.

The second objective of this thesis is to estimate tire forces without having road friction information for active safety systems in the newly developed Holistic Vehicle Control (HVC) paradigm. Kalman-based observers are employed on the longitudinal/lateral vehicle dynamics and wheel dynamics to estimate tire forces in real-time without any road friction data or any limiting assumption on vertical load distribution. This independent corner-based estimation structure meets the requirements of the traction and stability control systems, enhances vehicle safety, and can be transferred from one vehicle to another.

The third objective is to develop reliable real-time holistic velocity estimators at each corner robust to surface friction changes independent of the powertrain configuration in different driving scenarios, especially for combined-slip and low-excitation maneuvers, which are arduous for the current vehicle state estimators. The newly proposed velocity estimator in this research combines both kinematic and dynamic-based methods and incorporates tire deflection states to form a linear parameter-varying (LPV) system in which the road friction and sensor noises are considered to be uncertainties. Road tests confirm the validity of the algorithm on slippery roads as well as normal conditions. The current findings of the friction-independent velocity estimator have important implications on a joint road friction classification and state estimation scheme. A wheel torque-free lateral velocity estimator is also required for conventional vehicle applications and is an objective for the proposed estimators. Moreover, a road friction classifier, which performs in low-excitation regions as well as near-saturation and nonlinear regions, is another objective of this thesis. This road classifier can introduce new bounds on model uncertainties, which results in more accurate and less conservative observers for parameter-varying velocity estimators.

1.3 Thesis Outline

The background and literature review of road angle estimation, tire force estimation, and vehicle velocity estimation is presented in the second chapter of this thesis. The literature on vehicle state estimation is reviewed considering the fact that surface friction information is unavailable in the model-based approaches. The literature review on road condition estimation is also provided in the second chapter.

In the third chapter, a structure is provided for estimation of the road angles. The body angles are estimated using corners' displacements measured by the suspension height sensors installed at four corners. An unknown input observer robust to acceleration noises and road uncertainties is then developed on the roll and pitch dynamics of the vehicle to estimate the road bank and grade using body angles. Knowledge of tire parameters and road friction is not required in the proposed structure. The correlation between the road angle rates and the pitch/roll rates of the vehicle are also investigated to increase the accuracy. Performance of the proposed approach in reliable estimation of the road angles is experimentally demonstrated through vehicle road tests.

In the fourth chapter, a generic corner-based force estimation method to monitor tire capacities is presented. This is entailed for more advanced vehicle stability systems in harsh maneuvers. A nonlinear and a Kalman observer is utilized for estimation of the longitudinal and lateral friction forces. The stability and performance of the time-varying estimators are explored and it is shown that the developed integrated structure is robust to model uncertainties, does not require knowledge of the road friction, and can be transferred from one car to another. Software co-simulations are utilized to test the proposed force estimation method using MATLAB/Simulink and CarSim packages. Road experiments are also conducted on different road surface conditions. The simulations and road experiments demonstrate the effectiveness of the estimation approach in diverse driving conditions.

Chapter five presents a vehicle velocity estimator by integrating the lumped LuGre tire model and the vehicle kinematics to deal with model-based and kinematic-based velocity estimation issues. It is shown that the proposed corner-based estimator does not require knowledge of the road friction, is robust to model uncertainties such as tire parameters and inflation pressure, and can be easily reconfigured to operate with different vehicles. The stability of the time-varying longitudinal and lateral velocity estimators is explored.

An integrated lateral velocity estimator is also developed that is independent of the wheel torques and utilizes wheel speed, accelerations, yaw rate, and steering angle which are common in production vehicles. Moreover, a road friction classification approach is discussed and experimentally verified in low-excitation as well as nonlinear regions in this chapter. A generic joint estimation algorithm is introduced to classify the road friction condition and define tire capacities based on matching vehicle lateral responses to the expected responses on dry and slippery surfaces using pure and combined-slip friction models. The proposed methods are experimentally validated in several maneuvers with low and high levels of excitation and various driveline configurations on dry and slippery surfaces. The results exhibit promising performance of the velocity estimators and road classifier in different test conditions for both electric and conventional vehicles.

Chapter 2

Literature Review and Background

This chapter focuses on different approaches of vehicle state estimation, including kinematic-based and model-based. Tire models and their significance on estimation methods are also provided. Finally, literature review on road angle and condition estimation is presented.

2.1 Tire Forces

Tire-road forces have played a vital role in state of the art developments in the field of vehicle state estimation and control. They are incorporated into the lateral dynamics to estimate vehicle states and analyze the vehicle stability on different roads. Tire curves are represented by three regions including linear, transient, and nonlinear defined by road friction coefficient, normal forces, and cornering stiffness. The generated longitudinal/lateral forces at each tire's patch during traction, braking, and cornering maneuvers are realized to depend on the road condition, slip ratio, slip angle, and normal forces which represent a one-to-one mapping between forces and slip values.

The most widely used static tire model, known as the Magic Formula, was proposed by Pacejka et al. [7], [8], and Uil [9], and provides a semi-experimental approach for tire force calculation. This suggested friction expression is derived heuristically from experimental tests and is generated using specific experimental data that allow independent linear and angular velocity modulation in the steady-state condition. One advantage of this model

is that it does not have differential equations in each form of partial or ordinary, making it an appropriate choice for real-time simulations. This model focuses on the steady-state response of the tires versus slip and is generated based on empirical data. The *Magic Formula* can be described as $Y = D\sin\left[C\tan^{-1}(B\phi)\right] + S_y$ with $\phi = (1-E)(X+S_h) + \left(\frac{E}{B}\right)\tan^{-1}\left[B(X+S_h)\right]$ where Y could be longitudinal/lateral forces or the self-aligning moment, S_h, S_y are horizontal and vertical shifts respectively, B is the stiffness factor, C is the shape factor, D is the peak factor, E is the curvature factor, and Slip ratio/angle are the input to these equations and are denoted by X.

Steady-state assumption in the aforementioned model will not lead to precise outcomes during transient acceleration/barking maneuvers. Therefore, dynamic models seem more reliable for considering the transient phases as examined in [10–12]. Canudas-de-Wit et al. proposed a dynamic tire-road friction model, known as the LuGre, in [13–15], and introduced tire deflection as a state. Pre-sliding and hysteresis loops as well as combined friction characteristics are considered in their model [16].

Compared to other conventional approaches, e.g. Pacejka, the LuGre model utilizes relative velocities $v_{rx} = R_e\omega - v_{xt}$ and $v_{ry} = -v_{yt}$ rather than slip ratio $\lambda = \frac{v_{rx}}{\max\{R_e\omega, v_{xt}\}}$ and slip angle $\alpha = \tan^{-1}\frac{v_{yt}}{v_{xt}}$ where ω is the wheel speed and R_e is the tire's effective rolling radius. Longitudinal and lateral velocities in the tire coordinates are denoted by v_{xt} and v_{yt}. The passivity of the transient LuGre makes it a bounded and stable model and prohibits the divergence of both internal tire states and consequent forces [17]. Accurate force results will be obtained by considering normal force distributions over the contact patch and multiple bristle contact points. The average lumped LuGre model [18] symbolizes the distributed force over the patch line with some simplifications of normal force distribution; representing average deflection of the bristles, the tire internal lateral state $\bar{z}_q$ for each direction $q \in \{x, y\}$ in the average lumped LuGre model relates the relative lateral velocity v_{rq} and tire parameters as:

$$\dot{\bar{z}}_q = v_{rq} - (\kappa_q R_e|\omega| + \frac{\sigma_{0q}|v_{rq}|}{\theta g(v_{rq})})\bar{z}_q, \tag{2.1a}$$

$$\mu_q = \sigma_{0q}\bar{z}_q + \sigma_{1q}\dot{\bar{z}}_q + \sigma_{2q}v_{rq}, \tag{2.1b}$$

in which $\sigma_{0q}, \sigma_{1q}, \sigma_{2q}$ are the rubber stiffness, damping, and relative viscous damping in longitudinal/lateral directions, respectively. The normalized force of the averaged lumped

pure-slip LuGre model for each direction is denoted by μ_q. The force distribution along the patch line is represented by parameter κ_q in the average lumped model and can be a function of time, a constant, or may be approximated by an asymmetric trapezoidal scheme. The suggested value for κ_q in [18] is $\kappa_q = \frac{7}{6L_t}$, where L_t is the tire patch length. The function, $g(v_{rq})$ in the pure-slip model is defined for the longitudinal and lateral directions as $g(v_{rq}) = \mu_{cq} + (\mu_{sq} - \mu_{cq})e^{-|\frac{v_{rq}}{V_s}|^{\bar{\alpha}}}$, in which μ_{cq}, μ_{sq} are the normalized Coulomb friction and static friction, respectively. The Stribeck velocity V_s shows the transition between these two friction states and the tire parameter $\bar{\alpha} = 0.5$ is assumed for this study. In the current study, identification of the LuGre tire parameters was done using the experimental curves of the Chevrolet Equinox standard tires and by utilizing an error cost function and the nonlinear least square method. The tire curve resulting from the parameters identified in the lateral direction is compared with the experimental one in Fig. A.1 in the Appendix. The relative velocities v_{rx}, v_{ry} at the tire coordinates of the LuGre model represent the slip ratio λ and slip angle α in the mostly used tire models such as Burckhardt [19] and Pacejka [8] models. The level of tire and road adhesion is represented by introducing the road classification factor θ which may vary between $0 < \theta \leq 1$ according to dry, wet, and icy conditions. Chen and Wang [20] suggested a recursive least square (RLS) estimator and an adaptive control law with a parameter projection approach for identification of this road classification parameter. Identification of this factor is also addressed in [21] by a sliding mode observer for estimation of the maximum transmissible torque and wheel slip. Steady-state normalized longitudinal and lateral pure-slip LuGre tire forces are shown in Fig. 2.1 for a traction maneuver on roads with different classification numbers $0.2 < \theta < 0.97$, effective radius $R_e = 0.35\,[\mathrm{m}]$, parameters $V_s = 6.2, \bar{\alpha} = 0.5$, tire stiffness $\sigma_{0x} = 630, \sigma_{0y} = 182\,[1/\mathrm{m}]$, rubber damping $\sigma_{1x} = 0.77, \sigma_{1y} = 0.80\,[\mathrm{s/m}]$, relative viscous damping $\sigma_{2x} = 0.0014, \sigma_{2y} = 0.001\,[\mathrm{s/m}]$, load distribution factor $\kappa_x = 8.3, \kappa_y = 12.9$, normalized Coulomb friction $\mu_{cx} = 1.4, \mu_{cy} = 1.2$, and normalized static friction $\mu_{sx} = 0.8, \mu_{sy} = 0.9$.

Equations (2.1a), (2.1b) are developed based on the pure-slip condition, which cannot address the issue of decreasing lateral (or longitudinal) tire capacities due to the longitudinal (or lateral) slip. The combined-slip, i.e. direct correlation between the lateral and longitudinal slips, LuGre model is proposed by Velenis [16], in which the internal state $\bar{z}_q$

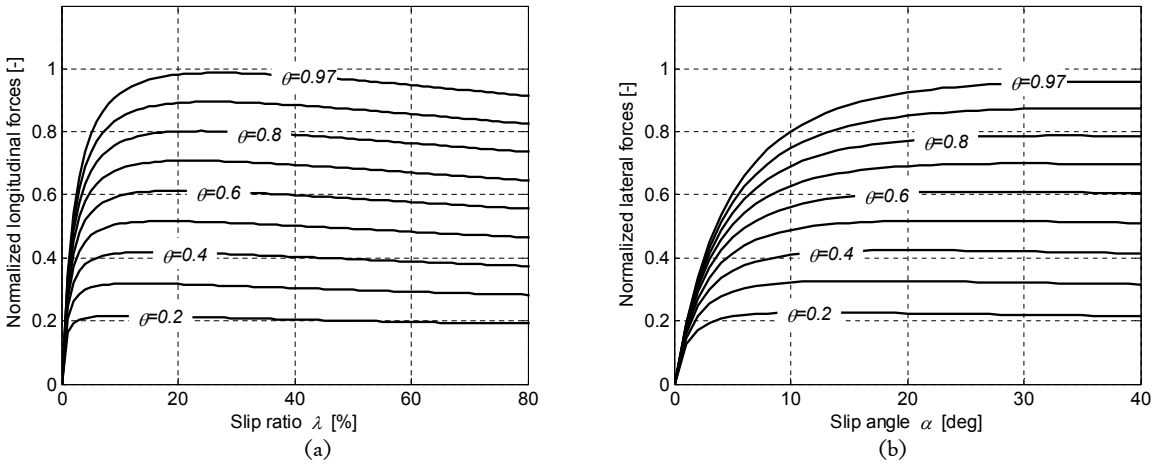

Figure 2.1: Pure-slip LuGre tire model, normalized forces (a) longitudinal (b) lateral

for each direction is described as:

$$\dot{\bar{z}}_q = v_{rq} - C_{0q}\bar{z}_q - \kappa R_e|\omega|\bar{z}_q, \tag{2.2}$$

where $C_{0j} = \frac{||M_c^2\mathbf{v_r}||\sigma_{0q}}{g(\mathbf{v_r})\mu_{cq}^2}$ and $M_c = [\mu_{cx} \quad 0;0 \quad \mu_{cy}]$. The transient function $g(\mathbf{v_r})$ between the Columb and static friction in the combined-slip tire model is introduced as:

$$g(\mathbf{v_r}) = \frac{||M_c^2\mathbf{v_r}||}{||M_c\mathbf{v_r}||} + \left(\frac{||M_s^2\mathbf{v_r}||}{||M_s\mathbf{v_r}||} - \frac{||M_c^2\mathbf{v_r}||}{||M_c\mathbf{v_r}||}\right) e^{-|\frac{||\mathbf{v_r}||}{V_s}|^{0.5}}, \tag{2.3}$$

where $M_s = [\mu_{sx} \quad 0;0 \quad \mu_{sy}]$ and $\mathbf{v_r} = [v_{rx} \quad v_{ry}]^T$. The final form of the normalized friction force $\left(\mu_j = \frac{F_j}{F_{zj}}\right)$ of the averaged lumped LuGre model with $\bar{\mathbf{z}} = [\bar{z}_y \quad \bar{z}_x]^T$ yields [16]

$$\mu = \sigma_0\bar{\mathbf{z}} + \sigma_1\dot{\bar{\mathbf{z}}} + \sigma_2\mathbf{v}_r, \tag{2.4}$$

in which $\mu, \bar{\mathbf{z}}, \mathbf{v}_r \in \mathbb{R}^2$ and can be described both in longitudinal and lateral directions in the combined or unidirectional-slip models. The longitudinal relative velocity is defined by $v_{rx} = \lambda R_e\omega$ and $v_{rx} = \lambda v_{xt}$ for the traction and brake cases, respectively. In addition, the rubber stiffness is $\sigma_0 = [\sigma_{0x} \quad 0;0 \quad \sigma_{0y}]$, the rubber damping is $\sigma_1 = [\sigma_{1x} \quad 0;0 \quad \sigma_{1y}]$, and the relative viscous damping is defined by $\sigma_2 = [\sigma_{2x} \quad 0;0 \quad \sigma_{2y}]$, in which σ_{0q}, σ_{1q} and σ_{2q}, are the rubber stiffness, damping, and relative viscous damping in each direction, $q \in \{x, y\}$. Figure 2.2 illustrates the effect of slip angle on the normalized longitudinal

forces and the effect of longitudinal slip on the normalized lateral forces. It corroborates the decreased tire capacity especially for the lateral direction in case of employing the combined-slip model which is close to real behavior of the tire.

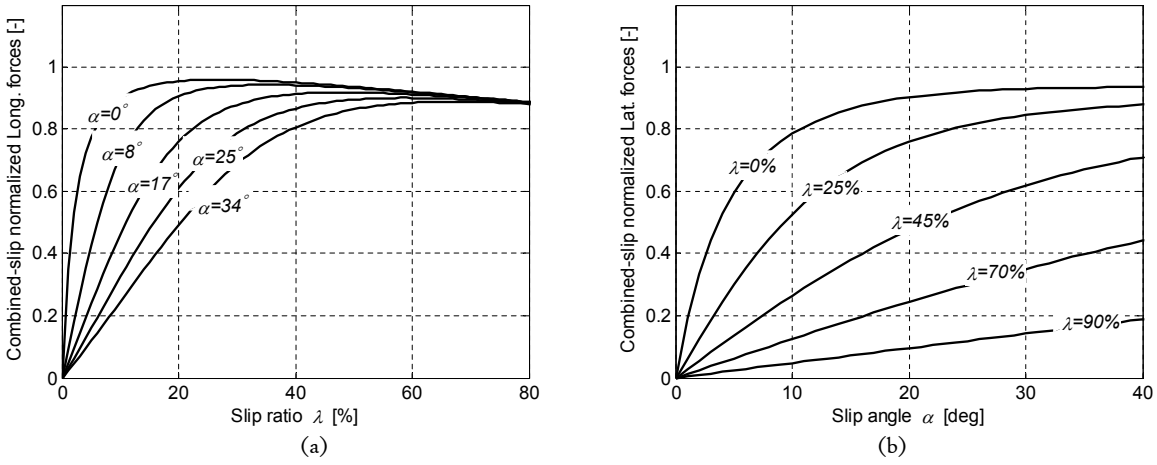

Figure 2.2: Combined-slip LuGre model, normalized tire forces (a) longitudinal (b) lateral

These pure and combined-slip models can be used in road-independent state estimation approaches [22, 23] or incorporated in the lateral dynamics for road classification as will be described in Chapter 5.

2.2 Tire Force Estimation

Tire forces can be measured at each corner with sensors mounted on the wheel hub, but their significant cost, required space, and calibration and maintenance make them completely unfeasible for mass production vehicles. Provided that the tire force calculation needs road friction, even accurate slip ratio/angle information from the GPS will not engender forces at each corner. Hence, estimation of the longitudinal and lateral tire forces would be a remedy.

Several studies first have focused on road friction estimation and identification of tire parameters, in order to estimate longitudinal and lateral tire forces. Alvarez et al. [24] used a parameter adaptation law, a Lyapunov-based state estimator, and the dynamic

LuGre model [18] to estimate the road friction and longitudinal forces during an emergency brake condition. Employing the equivalent output error injection approach, Patel et al. proposed a second-order and third-order sliding mode observers in [25] to estimate the friction coefficient and consequently tire forces during brake on the pseudostatic LuGre [14], dynamic LuGre, and parameter-based friction [26] models. Ghandour et al. [27] developed a force and road friction estimation structure based on an iterative quadratic minimization of the error between the developed lateral force estimator and the Dugoff tire/road interaction model. Rajamani et al. [28] suggested a recursive least square for road identification and a nonlinear observer for longitudinal force estimation having wheel torques and accurate slip-ratio data from GPS. These methods rely on simultaneous road condition identification, which may impose undesirable estimation error produced by the time-varying model parameters.

Estimation of longitudinal and lateral tire forces independent from the road condition may be classified on the basis of wheel dynamics and planar kinetics into the nonlinear, sliding mode, Kalman-based, and unknown input observers. A force estimation method based on the steering torque measurement is introduced in [29,30], which requires additional measurements. Hsu et al. provided a nonlinear observer to estimate tire slip angles as well as the road friction condition in [31] with steering torque measurement.

A high gain observer with inputoutput linearization is proposed by Gao et al. [32] to estimate the lateral states. An extended Kalman filter (EKF) is employed in [33] to estimate tire forces and road friction condition simultaneously, which should handle the low excitation conditions. Baffet et al. [34] proposed a cascaded structure for estimation of the tire forces and vehicle side-slip angle with a sliding mode observer and EKF. Doumiati et al. [35] estimated tire forces with planar kinetics, EKF, and unscented Kalman filter (UKF) [36]. In their approach, longitudinal and lateral force evolution is modelled with a random walk model. They assume that tire forces and force sums on each track are associated according to the dispersion of vertical forces.

Cho et al. [37] estimated lateral tire forces using the vehicle's planar kinetics and a random-walk Kalman filter. A Kalman-based unknown input observer (UIO) is developed by Wang et al. [38, 39] for longitudinal and lateral force estimation with the wheel dynamics, vehicle's planar kinetics, measured wheel speeds, wheel torques, and the yaw rate. Using UKF and the wheel dynamics, Hashemi et al. [22, 40] developed a longitudinal force

estimator robust to road friction changes and uncertainties in the model such as effective rolling radius, tire inflation pressure, measured wheel speed and torques. Similarly, employing UKF for an antilock braking control system, Sun et al. [41] proposed a nonlinear observer robust to the road friction for the slip ratio and longitudinal force estimation. Their approach is tested during brake maneuvers on different road conditions.

2.3 Vehicle Velocity Estimation

Advanced vehicle active safety systems require dependable vehicle states, which may not be accessible by measurements, thus needing to be estimated. One major practical issues that have dominated the vehicle state estimation field is velocity estimation robust to the road friction changes to have slip ratio, slip angles, and vehicle side slip angle for the active safety systems. Longitudinal and lateral velocities make major contributions to traction and stability control systems, respectively and can be measured with GPS, but the poor accuracy of the mostly practiced conventional GPSs and the loss of reception in some areas are primary drawbacks.

Literature has adopted three major approaches for longitudinal/lateral velocity estimation. One is the modified kinematic-based approach, which uses acceleration and the yaw rate measurements from an inertial measurement unit (IMU) and estimates the vehicle velocities employing Kalman-based [42, 43], or nonlinear [44] observers. This method does not employ a tire model, but instead the sensors bias and noise should be identified precisely to have a reliable estimation. In addition, low-excitation cases that lead to erroneous estimation should be handled with this method.

To increase the accuracy of the estimated heading and position, Farrell et al. [45] used the carrier-phase differential GPS, which requires a base tower and increases the cost significantly. To remove noises and address the low excitation scenarios, some kinematic-based methodologies [46, 47] employs accurate GPS, which may be lost and imposes additional costs on commercial vehicles. Yoon and Peng [48] utilizes two low-cost GPS receivers for the lateral velocity estimation and compensates the low update rate issue of conventional GPS receivers by combining the IMU and GPS data using an EKF. They also proposed a vehicle state estimator by combining data of magnetometer, GPS, and IMU in [49] and

utilizing a stochastic filter integrated on the Kalman filter to reject disturbances in the magnetometer.

The other velocity estimation method integrates measured longitudinal/lateral accelerations and uses an observer on tire forces to correct the estimation. This approach requires a good perception of the road friction and a precise tire model. To deal with the varying tire parameters and model uncertainties, model scheduling is introduced in [50, 51] using tire slips. A nonlinear observer is also provided in [52] with simultaneous bank angle estimation to address the unknown tire parameters. An EKF is employed for both longitudinal and lateral vehicle velocity estimation in [53, 54]. EKF has been used in [55] along with the Burckhardt model [19] to estimate the vehicle states and tire model parameters; an EKF with smooth variable structure is also utilized in [56] to estimate tire slip and sideslip angles. Computational complexities of the EKF justify using a reliable approach such as UKF without any need for linearization in system dynamics. Antonov et al. employed a UKF for vehicle state estimation in [57] and provided longitudinal/lateral velocity estimators at each corner. They utilized wheel torques, wheel speeds, and a simplified empirical Magic formula [8] as the tire model, which requires known tire parameters and road friction. Similarly, employing UKF and knowledge of the road condition, Wielitzka et al. [58] and Sun et al. [41] proposed different methods for estimation of the lateral and longitudinal velocities using Magic formula and LuGre [13] tire models respectively.

Zhang et al. propose a sliding-mode observer in [59] to estimate velocities using wheel speed sensors, braking torque and longitudinal/lateral acceleration measurements. Their approach utilizes a sliding-mode observer for the velocity estimation and an EKF for estimation of the Burckhardt tire model's friction parameter. However, this method needs accurate tire parameters in presence of tire wear, inflation pressure, and road uncertainties. A switched nonlinear observer based on a simplified Pacejka tire model is introduced by Sun et al. [60] to provide estimates of longitudinal and lateral vehicle velocities and the tire-road friction coefficient during anti-lock braking. Their approach benefits from switching in specific cases because of unreliability of the measurements, but it relies on a predefined zero slip ratio for the longitudinal velocity measurement.

Other studies focus on the velocity estimation robust to the road condition, but implements additional measurements which are not common for conventional cars or require identification of tire parameters. Hsu et al. proposed a method in [29] and [31] to esti-

mate the road friction condition and sideslip angle using the steering torque sensor, which may not be applicable for all production vehicles. Nam et al. [61] presented a sideslip angle estimation method with a recursive least squares algorithm to improve stability of in-wheel-motor-driven electric vehicles, but their approach uses force measurements from the multisensing hub units, which are not available for all electric and conventional cars. A model-based vehicle lateral state estimator is developed in [62] using a a yaw rate gyroscope, a forward-looking monocular camera, an a priori map of road superelevation and temporally previewed lane geometry. Gadola et al. investigate a Kalman-based lateral vehicle estimation on a single-track car model in [63] with the Magic formula tire model. The derivatives of the lateral forces in their approach, however, may amplify noise effects in the lateral/longitudinal state estimates.

Therefore, developing a holistic vehicle state estimator using conventional sensor measurement (wheel speed, steering angle, and IMU) without using road friction information is desirable and provided in this thesis.

2.4 Road Angles and Condition Estimation

Several studies investigating the vehicle stability control and state estimation have been carried out based on known road angles [57, 64, 65]. Direct measurement of these angles in real-time is not practical for commercial vehicles due to costs. Therefore, recent development in vehicle's active safety systems have underlined the need for real-time estimation of the road bank and grade angles as addressed by many recent studies.

Several studies focus on estimation of road inclinations while assuming the road friction condition is known. A method for dynamic estimation of the road bank angle is discussed in [66], in which the roll and lateral dynamics are used to develop the bank angle estimator. The steady-state approximation of the bank angle is used as a reference to calculate the estimation error and design the observer. This steady-state approximation is obtained using a linear vehicle model by implementing road friction information and tire characteristics. To reduce the effects of inaccuracies in transient conditions, a dynamic factor based on the understeer coefficient in high-friction scenarios is integrated with the observer. Practical problems in terms of stability control associated with estimation stability due to switching

between the steady-state and transient conditions should be investigated. A disturbance observer is developed in [67] to estimate the vehicle roll and bank angle having the tires' cornering stiffness and the vehicle yaw angle. Zhao et al. introduced a sliding mode observer in [68] for the velocity estimation with the road angle adaptation. Their method employs a tire model that requires the road friction and tire parameters. Menhour et al. suggest an unknown input sliding-mode observer in [69] to estimate the road bank angle. Their method employs a linear bicycle handling model for the vehicle, which needs tires' cornering stiffness and road friction information subsequently.

Alternatively, to address the road friction uncertainties, some studies identify the road friction conditions simultaneously, which may be challenging in itself because of the issues arising from lack of excitations, tire models, etc. Grip et al. suggest a nonlinear vehicle sideslip observer in [70] that incorporates time-varying gains and road friction parameters to estimate the longitudinal/lateral velocities and road angles using a tire model. Their method suggests concurrent estimation of the vehicle states, road angles, and the road condition. A time-varying observer is utilized in [71] by Grip et al. for the concurrent estimation of the road bank and the road-tire friction characteristics. They also modulate the observer gains based on a set of practical driving scenarios to improve the performance on low-friction surfaces.

Some approaches do not implement knowledge of the road friction, but do not isolate the vehicle roll/pitch dynamics from the road inclinations. A road angle estimation is proposed by Hahn et al. in [72]. The vehicle pitch/roll induced by the suspension deflection is not separated from the road grade/bank angles. Imsland et al. suggest a nonlinear observer for the bank angle estimation in [52] to accommodate various road conditions and compared their method with an extended Kalman filter from the view point of numerical complexity. An unknown input observer is also proposed in [73] to estimate the lateral states of the vehicle as well as the bank angle. In their study, the road bank angle is assumed to be constant and its time-varying characteristics have not been taken into account in the error dynamics. A proportional integral $\mathcal{H}_\infty$ filter is proposed by Kim et al. in [74]. They modified a bicycle model and made the estimation algorithm more robust against model and measurement uncertainties. In their model, the vehicle roll is not separated from the road bank.

Other literature has offered methods independent from the road friction and has in-

cluded roll/pitch dynamics with additional measurements. Utilizing a tire model and steering torque measurement, Carlson et al. offer a methodology for the separation of the road angles from the induced vehicle angles in [75] to avoid vehicle rollover. Ryu et al. used two-antenna GPS receivers to estimate the road bank and compensate the corresponding roll effect on the vehicle state estimator in [76]. Roll dynamic parameters are also identified in their method. Hsu and Chen in [77] provide a model-based estimation approach for the road angles. Their method combines multiple roll and pitch models and a switching observer scheme. However, knowledge of the vehicle yaw angle, which is not accessible in commercial vehicles is required in their proposed observer.

Some literature attempted to identify the road condition and estimated vehicle states simultaneously. Grip et al. suggest a nonlinear sideslip angle observer in [70, 78] that incorporates time-varying gains and estimates the vehicle states as well as the surface friction using a tire model. Their method should cope with the noises and uncertainties imposed by road identification errors due to the lack of excitation. You et al. [79] introduces an adaptive least square approach to jointly estimate the lateral velocities and tires' cornering stiffness (road friction terms). The road bank angle is also identified in their approach. However, lateral acceleration measurement noises have not been addressed. A sliding-mode observer is provided by Magallan et al. in [21] based on the LuGre tire model [13] to estimate the longitudinal velocity and the surface friction.

To summarize, three main challenges exist in the current studies on the road angle and condition estimation: **a)** unknown tire parameters and road friction conditions; **b)** incorporating effects of the vehicle roll and pitch angles; **c)** using available sensors and available measurements. Therefore, an estimation approach which tackles these challenges will be promising. The proposed road angle estimation approach in this thesis is independent of the road friction, investigates the road-body kinematics to relate the measured angle rates and the rate of change of the road angles, and is experimentally tested in different driving scenarios. In addition, the proposed generic road classifier compares the vehicle's lateral response with the predicted responses on various road frictions both in low-excitation and nonlinear regions and is not sensitive to tire parameters.

Chapter 3

Estimation of the Road Angles

This chapter proposes road bank and grade angle estimators independent of the road friction without limiting assumptions. The proposed estimation scheme operates in different driving scenarios as verified by road test experiments. This chapter is structured as follows. First, estimation of the vehicle body's angles, observer development on the roll/pitch dynamics, and the road-vehicle kinematics are provided. Next, an unknown input observer is proposed for estimation of the road bank and grade angles. Later, the road experiments to verify the approach in various maneuvers and driving conditions are presented.

3.1 Introduction

The proposed estimation structure is depicted in Fig. 3.1. An unknown input observer is developed to estimate the road bank and grade angles. The *Sprung mass kinematic model* provides vehicle body angles $\bar{\phi}_v, \bar{\theta}_v$ for the unknown input estimator.

The body angles are estimated using corners' displacements measured by the suspension height sensors installed at corners. The *Road-body kinematics* module is employed to relate the vehicle's frame, body, and road angles. This module relates the road angle rates and the measured angles rates by the sensors attached to the vehicle body, and provides time derivatives $\dot{\bar{\phi}}_{v\_ij}, \dot{\bar{\theta}}_{v\_ij}$ of the vehicle body angles. The *Unknown input observer* module

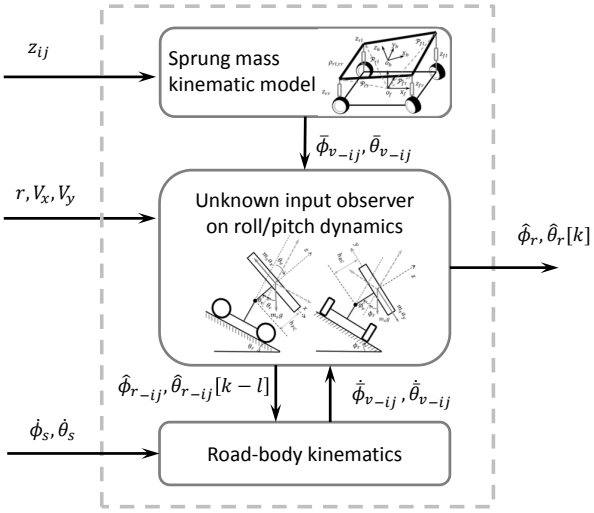

Figure 3.1: The proposed structure for the road angle estimation

uses estimated vehicle angles and their rates for the road bank/grade estimation. Details for each block are presented in the following subsections.

3.2 Sprung Mass Kinematics

The sprung mass kinematics is used to estimate the vehicle's body roll and pitch angles ϕ_v, θ_v using corners' displacements z_{ij}. These displacements are measured by the suspension height sensors installed at corners. A schematic of the sprung mass model and the positions of the suspension height sensors are depicted in Fig. 3.2

The auxiliary coordinates (x_a, y_a, z_a) is a right-handed orthogonal axis system obtained by rotating the Global coordinates about the z_G axis by the vehicle yaw angle ψ. The intermediate axis system (x_i, y_i, z_i) is given by pitch rotation θ about the y_a axis (from the auxiliary coordinates) [80]. The vehicle frame coordinates (x_f, y_f, z_f) is also a right-handed orthogonal axis system located at the center of the frame on undeformed body. Thus, it is parallel to the plane of the road. The subscript b represents the coordinates attached to the vehicle body as can be seen from Fig. 3.2. The sensor position vectors in the frame coordinate system (x_f, y_f, z_f) are described as follows with $i \in \{f, r\}$ (front and

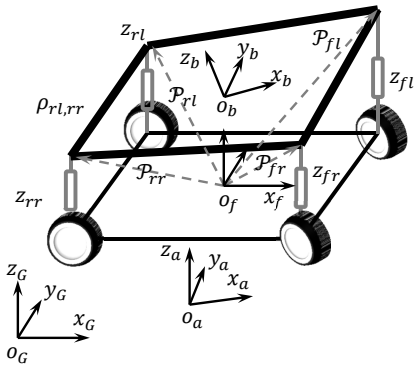

Figure 3.2: Height sensors and sprung mass kinematics

rear tracks):

$$\mathcal{P}_{iL} = [d_i \quad Tr_i/2 \quad z_{iL}]^T, \quad \mathcal{P}_{iR} = [d_i \quad -Tr_i/2 \quad z_{iR}]^T, \tag{3.1}$$

where d_f and d_r are the longitudinal distances between the origin O_f and the front and rear axles, respectively. The front and rear track widths are denoted by Tr_f and Tr_r, respectively. Relative position vectors $\rho_{ij,mn}$ between two corners can be obtained by:

$$\rho_{ij,mn} = \mathcal{P}_{mn} - \mathcal{P}_{ij}, \tag{3.2}$$

The normal vector for the sprung mass plane is then expressed as the cross product of any two relative position vectors:

$$\mathcal{N} = \rho_{ij,mn} \times \rho_{ij,pq}, \tag{3.3}$$

in which the subscripts $ij, mn, pq \in \{fL, fR, rL, rR\}$ represent front-left (fL), front-right (fR), rear-left (rL), and rear-right (rR) corners. Therefore, by using any three suspension height sensor data and corner positions, the respective normal vectors can be written as $\mathcal{N}_{-fL} = \rho_{rL,rR} \times \rho_{rR,fR}$, $\mathcal{N}_{-fR} = \rho_{fL,rL} \times \rho_{rL,rR}$, $\mathcal{N}_{-rL} = \rho_{rR,fR} \times \rho_{fR,fL}$, and $\mathcal{N}_{-rR} = \rho_{fL,rL} \times \rho_{fL,fR}$ where the subscript $-ij$ represents a scenario in which the suspension height provided by sensor ij is not used. Subsequently, components $\mathcal{N}_{-ij} = [\mathcal{N}^x_{-ij} \quad \mathcal{N}^y_{-ij} \quad \mathcal{N}^z_{-ij}]^T$ are used to estimate the vehicle angles. The roll and pitch angles $\bar{\phi}_{v_{-ij}}, \bar{\theta}_{v_{-ij}}$ can be written as follows with incorporation of the corresponding normal vector $\mathcal{N}_{-ij}$:

$$\bar{\phi}_{v_{-ij}} = cos^{-1} \frac{\mathcal{N}^y_{-ij}}{||\mathcal{N}_{-ij}||}, \quad \bar{\theta}_{v_{-ij}} = cos^{-1} \frac{\mathcal{N}^x_{-ij}}{||\mathcal{N}_{-ij}||}. \tag{3.4}$$

Four estimates for the vehicle roll angle, and four estimates for the vehicle pitch angle, can be obtained using different combinations of the suspension sensors, then a weighted average will be used as follows to have reliable estimates in case of existing outlier data due to uneven surfaces at each corner.

The four estimated vehicle's roll and pitch angles from (3.4) (four combinations of set of three corners) are examined to check the possibility of being an outlier because of road disturbances such as bumps and uneven surfaces at each corner. Validity of the vehicle's roll/pitch angles is checked at two stages. First, all four angles $\bar{\phi}_{v_{-ij}}, \bar{\theta}_{v_{-ij}}$ are compared to each other with variance checking scheme to eliminate the one with the largest deviation. Second, for each corner, the residuals of the vehicle angle rates are defined as the difference between the time derivatives of the estimated angles $\dot{\bar{\phi}}_{v_{-ij}}, \dot{\bar{\theta}}_{v_{-ij}}$ at $200[Hz]$and the measured vehicle's angle rates $\dot{\phi}_s, \dot{\theta}_s$:

$$R_{\dot{\bar{\phi}}_{-ij}} = |\dot{\phi}_s - \dot{\bar{\phi}}_{v_{-ij}}|, \quad R_{\dot{\bar{\theta}}_{-ij}} = |\dot{\theta}_s - \dot{\bar{\theta}}_{v_{-ij}}|. \tag{3.5}$$

When there is no disturbance at each corner, all corners' residuals $R_{\dot{\bar{\phi}}_{-ij}}, R_{\dot{\bar{\theta}}_{-ij}}$ fall below a certain threshold $T_q = T_{sq} + T_{eq}(|a_x| + |a_y|)$ where $q \in \{\phi, \theta\}$. The static minimum value for the threshold is denoted by T_{sq}, and T_{eq} introduces the effect of longitudinal/lateral excitations to the threshold. Low-pass filters can also be utilized to smooth the time derivatives of the estimated angles. After isolation of the outliers by the mentioned two tests, weighted vehicle angles $\bar{\phi}_{v_{-ij}}, \bar{\theta}_{v_{-ij}}$ from each combination of the three corner sensors are employed in the estimation of the vehicle's roll/pitch angles as follows [81]:

$$\bar{\phi}_v = \sum_{ij} \gamma_{-ij} \bar{\phi}_{v_{-ij}}, \quad \bar{\theta}_v = \sum_{ij} \gamma_{-ij} \bar{\theta}_{v_{-ij}}, \tag{3.6}$$

where the weight of each three sensor combination is denoted by γ_{-ij} and is set to 0.25 (average of the calculated angles) for the case in which there is no outlier. Whenever a disturbance or an outlier is detected in the suspension height sensor measurement at a corner, three weights will be zero since the subsequent three estimated body angles by such an outlier is not reliable. For instance, when there is a disturbance at the front-right suspension height sensor, its residuals exceed the thresholds T_ϕ, T_θ, thus the only non-zero weight will be γ_{-fR} and all other three weights will be zero. When more than one outlier is identified, the estimated vehicle roll/pitch angles are not valid and the algorithm

incorporates the previously estimated valid body angles. The estimated vehicle angles (3.6) are employed for the unknown input observer to estimate the road angles as will be discussed in the following subsection.

3.3 Unknown Input Observer for Road Angle Estimation

This section presents a methodology to estimate the road angles using unknown input observers (UIO). The problem of constructing an observer for systems with unknown inputs (epitomizing disturbances, faults, and uncertainties) has been widely tackled in literature with realizing full and reduced-order observers [82–85] and turns out to be considerably useful in diagnosing system faults [86–88]. A general form of the UIO is utilized in this section to estimate the unknowns (terms representing the road angles) with implementation of the vehicle body angles and their rates as the outputs. Roll and pitch dynamic models in the ISO coordinates are used for the proposed UIO and graphically illustrated in Fig. 3.3. The road bank and grade angles are denoted by ϕ_r and θ_r respectively.

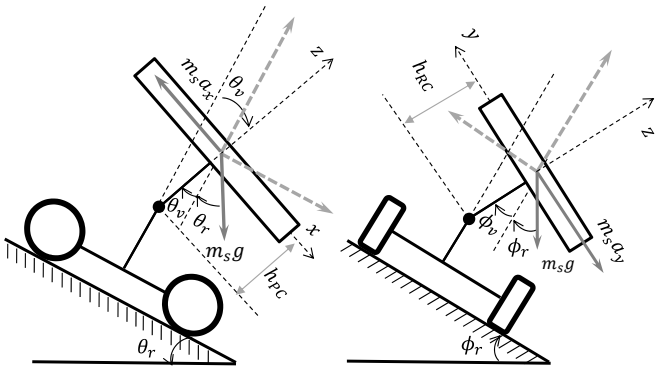

Figure 3.3: Roll and pitch models with the road angles

Employing vehicle kinematics, the roll and pitch dynamics can be expressed as $\dot{x}_\phi = A_\phi x_\phi + B_\phi u_\phi$ and $\dot{x}_\theta = A_\theta x_\theta + B_\theta u_\theta$ where the states are $x_\phi = [\phi_v \quad \dot{\phi}_v]^T$, $x_\theta = [\theta_v \quad \dot{\theta}_v]^T$ [89], and the roll and pitch angles of the sprung mass are denoted by ϕ_v, θ_v. The roll and

pitch dynamics yield:

$$\dot{x}_\phi = \begin{bmatrix} 0 & 1 \\ \frac{-K_\phi}{I_x+m_s h_{rc}^2} & \frac{-C_\phi}{I_x+m_s h_{rc}^2} \end{bmatrix} x_\phi + \begin{bmatrix} 0 \\ \frac{m_s h_{rc}}{I_x+m_s h_{rc}^2} \end{bmatrix} u_\phi, \tag{3.7}$$

$$\dot{x}_\theta = \begin{bmatrix} 0 & 1 \\ \frac{-K_\theta}{I_y+m_s h_{pc}^2} & \frac{-C_\theta}{I_y+m_s h_{pc}^2} \end{bmatrix} x_\theta + \begin{bmatrix} 0 \\ \frac{m_s h_{pc}}{I_y+m_s h_{pc}^2} \end{bmatrix} u_\theta, \tag{3.8}$$

in which road bank and grade angles ϕ_r, θ_r appear in unknown inputs u_ϕ, u_θ. In (3.7) and (3.8), the distances between the roll/pitch axes and the center of gravity are denoted by h_{rc} and h_{pc}. The moments of inertia about the roll and pitch axes parallel to the frame coordinate system are shown by I_x, I_y. Roll/pitch stiffness K_ϕ, K_θ and damping C_ϕ, C_θ are used for derivation of the roll and pitch dynamics. The unknown longitudinal and lateral inputs are denoted by:

$$\begin{aligned} u_\phi &= \dot{V}_y + rV_x + g\sin(\bar{\phi}_v + \phi_r), \\ u_\theta &= -\dot{V}_x + rV_y + g\sin(\bar{\theta}_v + \theta_r), \end{aligned} \tag{3.9}$$

in which ϕ_r and θ_r show the road bank and grade respectively. The vehicle's yaw rate r is measured by the available stock inertial measurement unit (IMU) sensor. The longitudinal and lateral velocities V_x, V_y can be measured by a GPS or can be estimated using linear, nonlinear, or Kalman-based observers provided in literature [22, 23, 33, 41, 57, 64, 90, 91]

Therefore, systems (3.7), (3.8) can be rewritten as $\dot{x}_q = A_q x_q + B_q u_q$ and $y_q = C_q x_q + D_q u_q$ with $q \in \{\phi, \theta\}$ and the state vectors $x_q \in \mathbb{R}^2$, unknown input vector $u_q \in \mathbb{R}$, output $y \in \mathbb{R}^2$, and system matrices A_q, B_q, C_q, D_q of appropriate dimensions where $[B_q \quad D_q]^T$ is full column rank and . The road angles also appear as unknown parameters in roll/pitch dynamics (3.7), (3.8). An unknown input observer [84, 87] is designed to estimate the road bank ϕ_r and road grade θ_r (unknown inputs u_q) using vehicle body's roll/pitch angles $\bar{\phi}_v, \bar{\theta}_v$ and their rates $\dot{\bar{\phi}}_v, \dot{\bar{\theta}}_v$ as measurements. Derivation of the vehicle roll/pitch rates are discussed at the end of the next subsection *Road-body kinematics*.

To develop the observer for practical application, discretization of the systems (3.7), (3.8) is performed by the Step-Invariance method.

Remark 1. *In general, discretization of the continuous-time system* $\dot{x} = Ax + Bu$ *with the output* $y = Cx + Du$ *is done by the zero-order hold (step-invariance) method [92], because of its precision and response characteristics. Input to the continuous-time system is the hold signal* $u_k = u(t_k)$ *for a period between* $t_k \leq t < t_{k+1}$ *with the sample time* T_s*. Then, the discrete-time system has the output matrices* $\bar{C} = C, \bar{D} = D$ *and state/input matrices* $\bar{A} = e^{A(t)T_s}, \bar{B} = \int_0^{T_s} e^{A(t)\tau} B(t) d\tau$

Thus, the discrete-time form of the roll and pitch dynamics yields:

$$\begin{aligned} x_{q_{k+1}} &= \bar{A}_q x_{q_k} + \bar{B}_q u_{q_k} \\ y_{q_k} &= \bar{C}_q x_{q_k} + \bar{D}_q u_{q_k}, \end{aligned} \tag{3.10}$$

The system (3.10) have an L-delay inverse if it is feasible to uniquely recover the unknown input u_{q_k} from the initial state x_0 and outputs up to time step $k + L$ for a positive integer L; the least integer L which leads to L-delay inverse is the inherent delay of the system. The upper bound on the inherent delay is defined as $L \triangleq n - Null(\bar{D}_q) + 1$ in [93]. The output equation from (3.10) can be accumulated for L time steps:

$$\begin{bmatrix} y_{q_0} \\ y_{q_1} \\ y_{q_2} \\ \vdots \\ y_{q_L} \end{bmatrix} = \begin{bmatrix} \bar{C}_q \\ \bar{C}_q \bar{A}_q \\ \bar{C}_q \bar{A}_q^2 \\ \vdots \\ \bar{C}_q \bar{A}_q^L \end{bmatrix} x_0 + \begin{bmatrix} \bar{D}_q & 0 & 0 & \cdots & 0 \\ \bar{C}_q \bar{B}_q & \bar{D}_q & 0 & \cdots & 0 \\ \bar{C}_q \bar{A}_q \bar{B}_q & \bar{C}_q \bar{B}_q & \bar{D}_q & \cdots & 0 \\ \vdots & \vdots & \vdots & \ddots & \vdots \\ \bar{C}_q \bar{A}_q^{L-1} \bar{B}_q & \bar{C}_q \bar{A}_q^{L-2} \bar{B}_q & \bar{C}_q \bar{A}_q^{L-3} \bar{B}_q & \bar{D}_q & \end{bmatrix} \begin{bmatrix} u_{q_0} \\ u_{q_1} \\ u_{q_2} \\ \vdots \\ u_{q_L} \end{bmatrix} \tag{3.11}$$

which can be expressed as:

$$y_{q_{0:L}} = \mathcal{O}_{Lq} x_0 + \mathcal{J}_{Lq} u_{q_{0:L}}, \tag{3.12}$$

where $\mathcal{J}_{Lq}$ is the invertibility matrix of the system (3.10), L is required for recovery of x_{q_0} from the output $y_{q_{0:L}}$, and $\mathcal{O}_{Lq}$ is the observability matrix for the pair $\bar{A}_q, \bar{C}_q$. Observability and invertibility matrices are provided in the Appendix. When the start point is the sample time k, (3.12) yields $y_{q_{k:k+L}} = \mathcal{O}_{Lq} x_k + \mathcal{J}_{Lq} u_{q_{k:k+L}}$.

Without loss of generality, the matrix $\begin{bmatrix} \bar{B}_q \\ \bar{D}_q \end{bmatrix}$ is assumed to be full rank [87] (this can be enforced by a proper transformation on the unknown inputs). Thus, there exists a matrix

$\bar{\mathcal{S}}$ such that $\bar{\mathcal{S}} \begin{bmatrix} \bar{B}_q \\ \bar{D}_q \end{bmatrix} = I_p$. The unknown input observer for a positive arbitrary L results in the following estimator, which provides the states $\hat{x}_{\phi_k}, \hat{x}_{\theta_k}$ as well as unknown inputs $\hat{u}_{\phi_k}, \hat{u}_{\theta_k}$:

$$\hat{x}_{q_{k+1}} = E_q \hat{x}_{q_k} + F_q y_{q_{k:k+L}}, \tag{3.13}$$

$$\hat{u}_{q_k} = \bar{\mathcal{S}} \begin{bmatrix} \hat{x}_{q_{k+1}} - \bar{A}_q \hat{x}_{q_k} \\ y_{q_k} - \bar{C}_q \hat{x}_{q_k} \end{bmatrix}, \tag{3.14}$$

where E_q and F_q are observer gain matrices obtained by pole placement as will be described in the following. The general form of the discrete-time system (3.10) with state vector $x_q \in \mathbb{R}^n$, output $y_q \in \mathbb{R}^m$, and unknown input vector $u_q \in \mathbb{R}^p$ has the observability and invertibility matrices $\mathcal{O}_{Lq} \in \mathbb{R}^{m(L+1)\times n}, \mathcal{J}_{Lq} \in \mathbb{R}^{m(L+1)\times p(L+1)}$ and observer gain matrices $E_q \in \mathbb{R}^{n\times n}, F_q \in \mathbb{R}^{n\times m(L+1)}$ respectively. Thereby, for the discretized form of the systems (3.7), (3.8), the observability matrix, invertibility matrix, and observer gain matrices are $\mathcal{O}_{Lq} \in \mathbb{R}^{2(L+1)\times 2}, \mathcal{J}_{Lq} \in \mathbb{R}^{2(L+1)\times(L+1)}$ and $E_q \in \mathbb{R}^{2\times 2}, F_q \in \mathbb{R}^{2\times 2(L+1)}$ when the vehicle body's roll/pitch angles and their rates $\dot{\phi}_v, \dot{\theta}_v$ are utilized as measurements.

The discrete-time estimation error for the pitch and roll dynamics can be expressed as follows using (3.10), (3.12), and the unknown input observer (3.13):

$$\begin{aligned} e_{q_{k+1}} &= \hat{x}_{q_{k+1}} - x_{q_{k+1}} \\ &= E_q \hat{x}_{q_k} + F_q y_{q_{k:k+L}} - \bar{A}_q x_{q_k} - \bar{B}_q u_{q_k} \\ &= E_q e_{q_k} + F_q \mathcal{J}_{Lq} u_{q_{k:k+L}} + (E_q - \bar{A}_q + F_q \mathcal{O}_{Lq}) x_{q_k} - \bar{B}_q u_{q_k} \end{aligned} \tag{3.15}$$

where the smallest L_q with upper bound $L_q < n - Null(\bar{D}_q) + 1$ should be determined such that $rank(\mathcal{J}_{Lq+1}) - rank(\mathcal{J}_{Lq}) = p$. In order to have asymptotic stability on the error dynamics (3.15) regardless of x_{q_k} and inputs, E_q should be stable, i.e. $|\lambda_i(E_q)| < 1, \forall i \in \{1, ..n\}$, and F_q should simultaneously satisfy the following [87]:

$$F_q \mathcal{J}_{Lq} = [\bar{B}_q \quad 0...0], \tag{3.16}$$

$$F_q \mathcal{O}_{Lq} + E_q - \bar{A}_q = 0. \tag{3.17}$$

The matrix F_q is obtained from $F_q = M_q V$ where $V = [0 \quad 0; I_p \quad 0]$ and $M_q = [\bar{M}_q \quad \bar{B}_q]$. The matrix $\bar{M}_q$ is chosen by a pole placement such that matrix $E_q = \bar{A}_q - \bar{B}_q \breve{W}_q - \bar{M}_q \bar{W}_q$ is stable. The matrix $W_q = [\bar{W}_q \quad \breve{W}_q]^T$ is defined as $W_q \triangleq V\mathcal{O}_{Lq}$ in which $\breve{W}_q$ has p rows.

The stability of the state estimation error dynamics (3.15), system equations (3.10) and the estimated unknown input (3.14) guarantees that $\hat{u}_{q_k} \to u_{q_k}$ as $k \to \infty$

Remark 2. *An unknown input observer with delay L_q can be designed for the system (3.10) if and only if the system is strongly detectable [84]. This is equivalent to the following conditions:*

$$rank(J_{Lq}) - rank(J_{Lq-1}) = p, \tag{3.18}$$

$$rank\left(\begin{bmatrix} A_q - zI_n & B_q \\ C_q & D_q \end{bmatrix}\right) = p + n \quad \forall z \in \mathbb{C}, |z| \geq 1. \tag{3.19}$$

Remark 3. *The systems (3.7) and (3.8) with the discretized form (3.10) and two measurements (roll/pitch and their rates) is strongly detectable. Thus, a UIO can be designed for this system.*

The road bank angle $\hat{\phi}_r$ is obtained as follows employing the estimated unknown input $\hat{u}_\phi$ from (3.14), the roll input definition (3.9) and the vehicle's roll angle from (3.6):

$$\hat{\phi}_{r_k} = \sin^{-1} \frac{\hat{u}_{\phi_k} - \dot{V}_{y_k} - r_k V_{x_k}}{g} - \bar{\phi}_{v_k}. \tag{3.20}$$

Similarly, the unknown input observer (3.14) is employed for estimation of the road grade $\hat{\theta}_r$, which appears as an unknown input to the pitch dynamics (3.8). Given the vehicle's pitch angle from (3.6), the pitch input definition (3.9) and the estimated unknown input $\hat{u}_\theta$ from (3.14), the road grade is estimated as:

$$\hat{\theta}_{r_k} = \sin^{-1} \frac{\hat{u}_{\theta_k} + \dot{V}_{x_k} - r_k V_{y_k}}{g} - \bar{\theta}_{v_k}. \tag{3.21}$$

The two measurements: roll/pitch angles from the suspension height sensors and their rates are used for the road grade and bank angle estimation employing the unknown input

observer (3.14) and equations (3.20), (3.21). To calculate the roll/pitch angle rates, taking time derivatives of the vehicle angles (3.6) is not a proper choice since it generates oscillations due to measurement noises. Filtering such noises usually imposes undesirable delays. Thus, implementing available measurements (roll/pitch rates) from the IMU seems more promising. In order to use the measured roll/pitch rates from the sensor attached to the sprung mass, transformation between the vehicle's frame coordinate and the body coordinate should be investigated. The following section focuses on the road-vehicle kinematics in order to relate the measured angle rates, vehicle body motion, and the rate of change of the road bank and grade angles.

3.4 Road-Body Kinematics

Euler angles ψ, θ, ϕ are utilized in this section to transform from the global coordinates (x_G, y_G, z_G) to the vehicle frame axis system shown in Fig. 3.2. These angles are successive rotations about z_G, y_a and x_f respectively. Using the rotation matrices, the angular velocity of the frame relative to the global axis system can be described by $\dot{\Gamma}_f = R_f^G \dot{\Gamma}$ where $\dot{\Gamma}_f = [\dot{\phi}_f \quad \dot{\theta}_f \quad \dot{\psi}_f]^T$ is the rotation rate of the frame relative to the global coordinates defined in the vehicle frame-fixed coordinates, and $\dot{\Gamma} = [\dot{\phi} \quad \dot{\theta} \quad \dot{\psi}]^T$ represents the rate of Euler angles. Defining $\dot{\Phi} = [\dot{\phi}, 0, 0]^T, \dot{\Theta} = [0, \dot{\theta}, 0]^T$, and $\dot{\Psi} = [0, 0, \dot{\psi}]^T$, one can write the rotation matrix R_f^G as:

$$R_f^G = R_{x_f,\phi}\dot{\Phi} + R_{x_f,\phi}R_{y_a,\theta}\dot{\Theta} + R_{x_f,\phi}R_{y_a,\theta}R_{z_G,\psi}\dot{\Psi}, \tag{3.22}$$

in which $R_{x_f,\phi}$ shows the third rotation by an angle ϕ about the x_f axis, $R_{y_a,\theta}$ is the second rotation by an angle θ about the y_a axis, and $R_{z_G,\psi}$ represents the first rotation by an angle ψ about the z_G axis. Substituting rotation matrices in (3.22) yields:

$$R_f^G = \begin{bmatrix} 1 & 0 & -S\theta \\ 0 & C\phi & S\phi C\theta \\ 0 & -S\phi & C\phi C\theta \end{bmatrix} \tag{3.23}$$

in which $C* = \cos(*)$ and $S* = \sin(*)$. Road angles are defined between the vehicle frame and the auxiliary axis system (x_a, y_a, z_a) [80]. Therefore, the angular velocity of the vehicle

frame relative to the auxiliary coordinates represents the rate of change of the road angles $\dot{\Gamma}_r = [\dot{\phi}_r \quad \dot{\theta}_r \quad \dot{\psi}_r]^T$. Transformation $(R_{y_a,\theta})^T$ from the intermediate coordinates (x_i, y_i, z_i) to the auxiliary one is used as follows to relate the road and Euler angle rates:

$$\dot{\Gamma}_r = (R_{y_a,\theta})^T \dot{\Phi} + \dot{\Theta} = \begin{bmatrix} C\theta & 0 & 0 \\ 0 & 1 & 0 \\ -S\theta & 0 & 0 \end{bmatrix} \dot{\Gamma} \tag{3.24}$$

Substituting $\dot{\Gamma} = (R_f^G)^{-1}\dot{\Gamma}_f$ into (3.24) results in:

$$\begin{aligned} \dot{\Gamma}_r &= \begin{bmatrix} C\theta & S\phi S\theta & C\phi S\theta \\ 0 & C\phi & -S\phi \\ -S\theta & -S\phi S\theta \tan\theta & -C\phi S\theta \tan\theta \end{bmatrix} \dot{\Gamma}_f \\ &= R_r^f \dot{\Gamma}_f, \end{aligned} \tag{3.25}$$

in which the rotation matrix R_r^f represents the transformation between the road and frame angles. The third component $\dot{\psi}_r$ can be neglected since the yaw rate of the road is not the concern for this study. Therefore, (3.25) is reduced to:

$$\dot{\Gamma}_r = \begin{bmatrix} C\theta & S\phi S\theta & C\phi S\theta \\ 0 & C\phi & -S\phi \end{bmatrix} \dot{\Gamma}_f = \chi_r^f \dot{\Gamma}_f, \tag{3.26}$$

where $\dot{\Gamma}_r = [\dot{\phi}_r \quad \dot{\theta}_r]^T$ shows the rate of the change of the road grade and bank angles. Afterward, employing the pseudo inverse $(\chi_r^f)^{-1}$, one can express the frame rotation rates as $\dot{\Gamma}_f = (\chi_r^f)^{-1}\dot{\Gamma}_r$ from (3.26). The pitch and roll rate sensors are mounted on the body sprung mass which has an orthogonal axis system (x_b, y_b, z_b). This body-fixed coordinate system is obtained by consecutive rotations of ϕ_v, θ_v around the x_f and y_f axes of the vehicle frame coordinates, respectively. The measured rotation rate signal, $\dot{\Gamma}_s = [\dot{\phi}_s \quad \dot{\theta}_s \quad \dot{\psi}_s]^T$ is affected by the rotation rates of the body-fixed coordinate $\dot{\Gamma}_v = [\dot{\phi}_v \quad \dot{\theta}_v \quad \dot{\psi}_v]^T$, and the frame rotation rate as $\dot{\Gamma}_s = \dot{\Gamma}_v + R_b^f \dot{\Gamma}_f$. Rotation matrix R_b^f is from the frame-fixed axes to the body-fixed axes and is a function of the vehicle roll/pitch angles ϕ_v, θ_v about the frame-fixed x axis:

$$R_b^f = \begin{bmatrix} C\theta_v & S\phi_v S\theta_v & -C\phi_v S\theta_v \\ 0 & C\phi_v & S\phi_v \\ S\theta_v & -C\theta_v S\phi_v & C\phi_v C\theta_v \end{bmatrix} \tag{3.27}$$

The relationship between the pitch/roll rate sensor measurements, vehicle pitch/roll rate, and road angle rates can be described using (3.26) as:

$$\dot{\Gamma}_s = \dot{\Gamma}_v + R_{br}\dot{\Gamma}_r \tag{3.28}$$

where the rotation between the road and the body-fixed axes is denoted by the rotation matrix $R_{br} = R_b^f(\chi_r^f)^{-1}$. An implication of (3.28) is that the road angle rates should be taken into account for estimation of the vehicle angle rates $\dot{\Gamma}_v$.

Conclusively, replacing ϕ_v, θ_v with the calculated vehicle roll/pitch angles $\bar{\phi}_v, \bar{\theta}_v$ from (3.6), one can summarize the relation between the estimated vehicle angle rates $\dot{\hat{\Gamma}}_{v_{-ij}}$, estimated road angle rates $\dot{\hat{\Gamma}}_{r_{-ij}}$, and the sensor measurement $\dot{\hat{\Gamma}}_{s_{-ij}}$, in a scenario without using the suspension height sensor ij as:

$$\begin{aligned}
\dot{\bar{\phi}}_{v_{-ij}} &= \dot{\phi}_s - R_1(\bar{\phi}_{v_{-ij}}, \bar{\theta}_{v_{-ij}})\dot{\hat{\phi}}_{r_{-ij}} \\
\dot{\bar{\theta}}_{v_{-ij}} &= \dot{\theta}_s - R_2(\bar{\phi}_{v_{-ij}}, \bar{\theta}_{v_{-ij}})\dot{\hat{\theta}}_{r_{-ij}}
\end{aligned} \tag{3.29}$$

where R_1, R_2 are components of $R_{br} = [R_1 \quad R_2]^T$. The estimation on the roads with the combined bank and grade angles can be achieved with (3.29) which presents the relation between the frame, body, and road angles. Equation (3.29) implies that the time derivatives of the vehicle angle rates $\dot{\bar{\phi}}_{v_{-ij}}, \dot{\bar{\theta}}_{v_{-ij}}$ can be calculated with the measured vehicle angle rates $\dot{\phi}_s, \dot{\theta}_s$ and the rate of change of the road angles. Assuming the road angles change smoothly, the road angle rates are obtained by the time derivative of the estimated ones $\bar{\phi}_{r_{-ij}}[k-l], \bar{\theta}_{r_{-ij}}[k-l]$ over l previous time steps. This is shown in Fig. 3.1, in which the estimated road angles over l previous time steps and measured body's angle rates are utilized in the *Road-body kinematics* to estimate the vehicle angle rates. Substituting the rates (3.29) and allocating the weights γ_{-ij}, the roll/pitch rates of the vehicle is expressed as follows:

$$\dot{\bar{\phi}}_v = \sum_{ij} \gamma_{-ij}\dot{\bar{\phi}}_{v_{-ij}}, \quad \dot{\bar{\theta}}_v = \sum_{ij} \gamma_{-ij}\dot{\bar{\theta}}_{v_{-ij}}. \tag{3.30}$$

The average weight ($\gamma_{-ij} = 0.25$) is used when there is no outlier. Whenever, a disturbance exist at the corner mn, the residuals (3.5) exceed the thresholds T_q and an outlier is detected. Therefore, three weights related to that corner are set to zero and the only

non-zero weight will be γ_{-mn}. Consequently, the vehicle roll/pitch rates (3.30) are utilized as measurements for the unknown input observers (3.13) and (3.14) described in the previous subsection. The unknown input observer and sprung-mass kinematics proposed and experimentally in this thesis is utilized to develop a fault diagnosis approach for suspension height sensors in [94].

The next section includes road tests to validate the proposed UIO (3.14) with measurements (3.6) and (3.30) on different roads with separate or combined bank/grade angles.

3.5 Experimental Results

Several experiments have been carried out on an electrified Chevrolet Equinox sport utility vehicle (SUV) with all-wheel-independent-drive configuration (AWD) and the specifications listed in Table 3.1 to verify the proposed estimation scheme. In addition to this AWD vehicle, specifications of another rear-wheel-drive test vehicle which will be used for validation of the velocity and force estimators in the next chapters are listed in the same table.

Table 3.1: Parameters of the Test Vehicles for Experiments

Parameter	Unit	AWD Vehicle	RWD Vehicle	Description
m, m_s	[kg]	$2260, 1989$	$2043, 1810$	Total & sprung mass
I_x, I_y, I_z	[kg.m^2]	$967, 2710, 4650$	$710, 2644, 4160$	Vehicle moments of inertia
I_w	[kg.m^2]	1.68	1.7	Wheel moment of inertia
d_f, d_r	[m]	$1.41, 1.43$	$1.40, 1.44$	Front/rear axles to CG
R_e	[m]	0.34	0.33	Effective radius
h_{rc}, h_{pc}	[m]	$0.54, 0.54$	$0.55, 0.55$	Roll/pitch axis height
K_ϕ, K_θ	[N/m]	$(1.51, 2.08) \times 10^5$	the same	Roll/pitch stiffness
C_ϕ, C_θ	[N.s/m]	$(0.63, 2.52) \times 10^4$	the same	Roll/pitch damping
Tr_f, Tr_r	[m]	$1.62, 1.56$	$1.60, 1.58$	Front/rear track width

The AWD vehicle's roll, pitch, and yaw rates as well as the longitudinal and lateral acceleration are measured with a 6-axis IMU (and GPS) system RT2000. The *Road Angle*

Estimator module requires longitudinal and lateral velocities, which can be measured using the GPS or estimated by the *Velocity Estimator* module as shown in Fig. 3.4-a. Four suspension height measurement sensors (from Delphi Co.) are installed at four wheel positions to measure vertical displacements of each corner and estimate vehicle body's angles of the electrified Chevrolet Equinox test vehicle shown in Fig. 3.4-b. Measured signals are communicated using a CAN-bus. Real-time acquisition and processing of sensory information and the developed algorithm is realized using the dSPACE® MicroAutobox. The dSPACE compiles measurements for MATLAB/Simulink, and the controller provides control signals for the dSPACE as well. Visualization of the experiment results is performed through the ControlDesk and MATLAB/Simulink. The sampling frequency for the experiment is set to be 200 [Hz]. Most of the tests are performed with two passengers in the car, but the nominal vehicle mass, from Table 3.1, is used for verification of the developed estimators in this thesis; there are cases with four passengers that has been specified clearly.

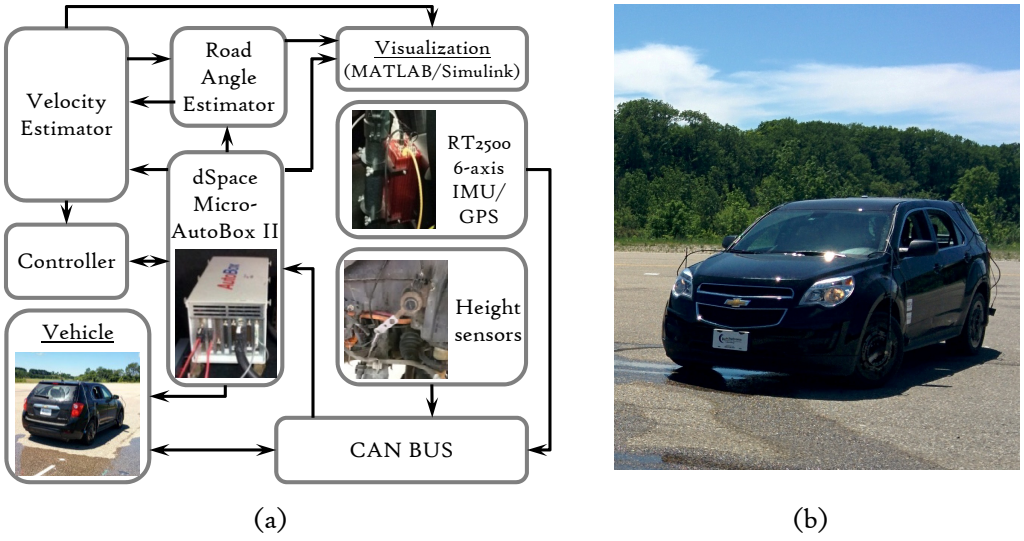

Figure 3.4: Experimental setup (a) the I/O and hardware layout (b) AWD test vehicle

Performance of the estimator is experimentally examined in three cases on roads with different bank and grade conditions; the inherent delay for both roll and pitch dynamics in the observer is $L_q = 1$, the static thresholds $T_{s\phi} = 0.02, T_{s\theta} = 0.04$ and excitation

thresholds $T_{e\phi} = 0.0015, T_{e\theta} = 0.0019$ are also used for the road experiments.

Case 1: Acceleration/brake on the graded road

Real-time performance the estimator in a maneuver with minor steering and successive acceleration and brake on a graded road is investigated in this section. Longitudinal and lateral accelerations for this maneuver are depicted in Fig. 3.5 which shows excitations in the longitudinal direction.

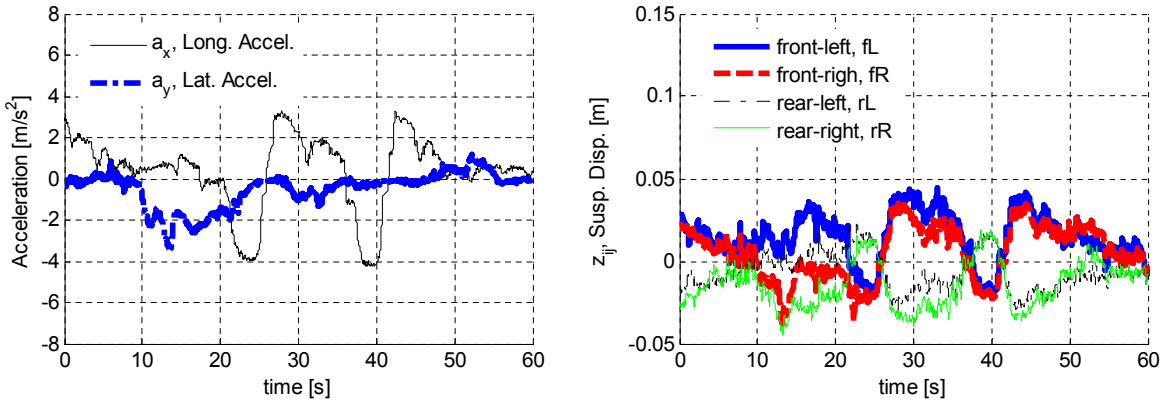

Figure 3.5: Acceleration and suspension height measurements on the graded road.

Suspension height sensor measurements are also shown in Fig. 3.5 that confirms several body pitch excitations due to the successive acceleration and brake.

Estimated vehicle body angles $\bar{\phi}_v, \bar{\theta}_v$ are illustrated in Fig. 3.6-a. There is no disturbance/outlier and the averaging method is used by the algorithm for the vehicle pitch/roll angle estimation. The estimated road grade in the ISO coordinate system is shown in Fig. 3.6-b, which exhibits correspondence with the measured actual grade in spite of harsh excitations on the vehicle body angles observed in Fig. 3.6-a.

This substantiates that the suggested unknown input observer can accurately estimate the road grade regardless of the longitudinal (body pitch) excitations.

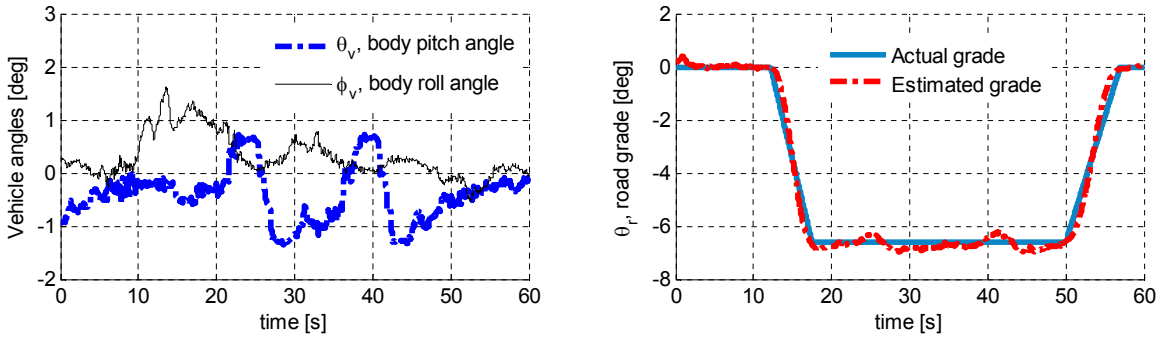

Figure 3.6: Estimation results for *Case1*, (a) vehicle angles (b) road grade.

Case 2: Normal driving on a banked road

To distinguish between the estimated bank and grade on different roads and check the performance of the suggested estimator, a normal driving scenario with steering and lateral excitation is performed on a banked road. Figure 3.7 illustrates the longitudinal/lateral accelerations and the displacements of each corner for this maneuver.

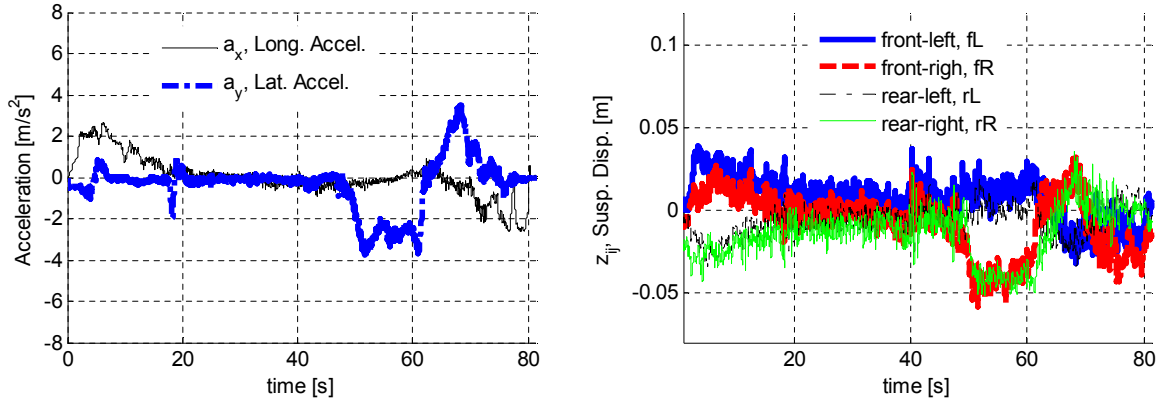

Figure 3.7: Acceleration and suspension height measurements on the banked road.

Variations in the lateral acceleration after $t = 50\,[\mathrm{s}]$ are caused by the road bank angle and the lateral excitation. Such a coupling makes the task of accurate real-time bank estimation more challenging. The suspension height displacement measurements depicted

in Fig. 3.7 have large fluctuations, but the suggested vehicle angle estimators (3.6) reject outliers and provide smooth vehicle roll and pitch angles as demonstrated in Fig. 3.8-a. Finally, the proposed estimator detects the road bank around the region of $t = 50\,[\mathrm{s}]$ as illustrated in Fig. 3.8-b.

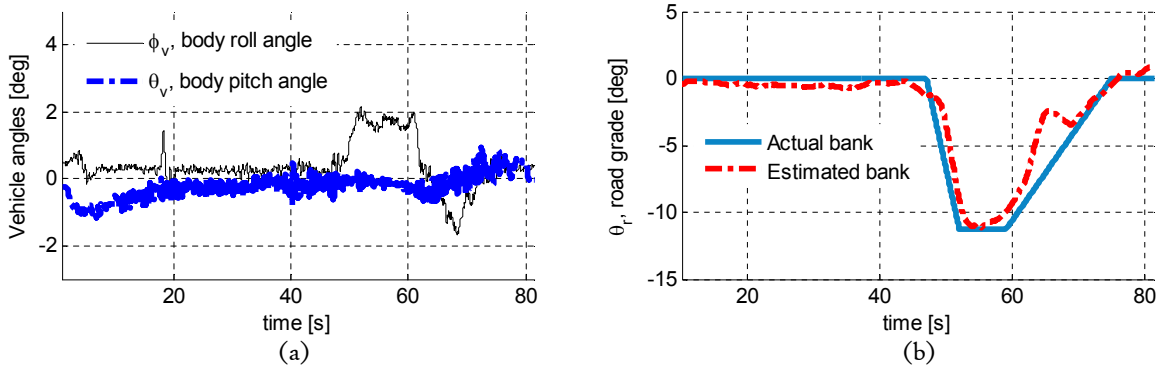

Figure 3.8: Estimation results for *Case2*, (a) vehicle angles (b) bank angle

The estimation results shown in Fig. 3.8-b confirms that even with the presence of the vehicle body angles around $t = 5$ and $t = 20\,[\mathrm{s}]$, the developed estimator can successfully differentiate between the road and the body angles generated by lateral excitations and does not provide any road bank. The observed deviations around $t = 65\,[\mathrm{s}]$ may be contributed to improper selection of E_q, F_q matrices and estimated vehicle velocities.

Case 3: Steering on a combined grade/bank

Performance of the unknown input observer on the roads with combined bank and grade angles is investigated in this case study. The maneuver includes driving on a graded road, lateral excitations by steering, and steering on a road with combined bank and grade. Estimating the road angles in this maneuver is challenging since the lateral excitations by the driver is performed on the combined banked/graded road. Figure 3.9 illustrates suspension height displacements and lateral/longitudinal excitations of the vehicle between $t = 35$ and $t = 92\,[\mathrm{s}]$, which includes both the driver and road excitations.

Measured suspension height displacements in Fig. 3.9 depicts lateral and longitudinal excitations and no outlier is detected. Successive excitations between $t = 60$ and $t = 70\,[\mathrm{s}]$

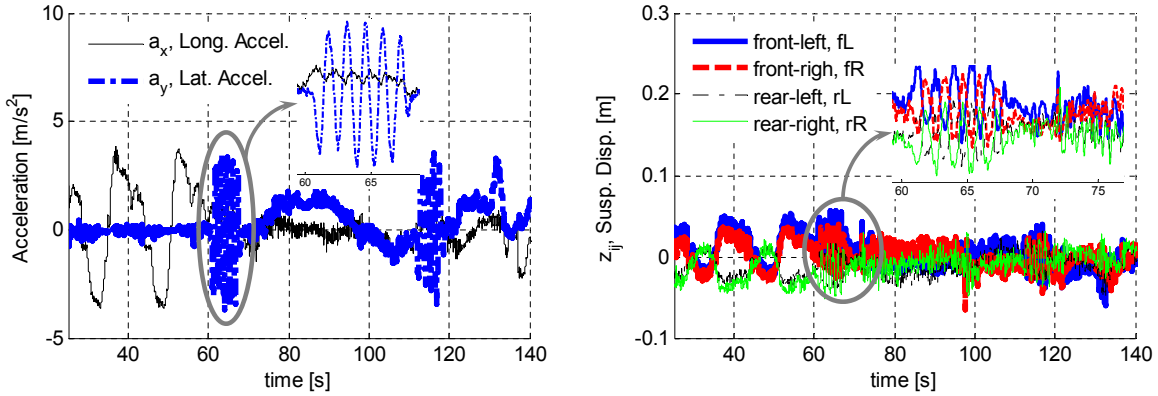

Figure 3.9: Acceleration and suspension height measurements on combined grade/bank

are because of the sine steering on the graded road. The results of the calculated vehicle angles $\bar{\phi}_v, \bar{\theta}_v$ are shown in Fig. 3.10-a.

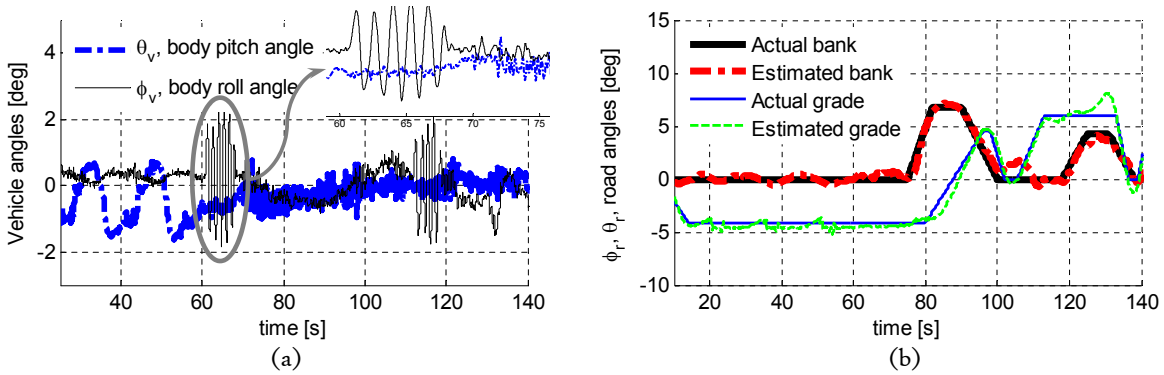

Figure 3.10: Road experiments, (a) estimated vehicle angles on combined grade/bank (b) estimated road angles

Despite the fact that the lateral excitations happened on the road with inclinations, the proposed unknown input observer can detect the road angles and distinguish between the body and road angles as depicted in Fig. 3.10-b. In spite of several pitch excitation (acceleration and brake) for $t \leq 60\,[\mathrm{s}]$, the proposed UIO distinguishes between the road grade and vehicle body pitch angles and detect the road grade. Thus, the body pitch/roll does not affect this method significantly and are implemented as inputs in (3.20) and (3.21)

to identify the road angles.

The experiments on various roads and with different drivers' inputs demonstrates that the proposed UIO can reject the outliers due to uneven road conditions at each corner and estimate the road angles. However, there are some errors for the combined bank and grade cases which may be due to errors in estimated vehicle velocities and inappropriate selection of the UIO gain matrices for the coupled roll and pitch dynamics that can be addressed in future.

3.6 Summary

In this chapter, a method for estimation of the road angles was proposed and the developed real-time estimation structure was experimentally tested for estimation of road bank and grade angles. The suggested algorithm does not require any information about the road friction, tire forces, and tire parameters. It includes an unknown input observer on the roll and pitch dynamics of the vehicle. Observer gain matrices were designed to guarantee a fast convergence rate and satisfy (3.16) and (3.17). Road disturbances and outliers were isolated in the provided method using a dynamic threshold based on the longitudinal and lateral excitations of the vehicle.

Incorporating road-body kinematics helped to increase the accuracy by defining the correlation between the road angle rates and the pitch/roll rates of the vehicle and the developed correlated kinematics can be used in any vehicle. Road angle estimation in maneuvers with high excitation on banked/graded roads, fast convergence and robustness against harsh excitations, road disturbances, and outliers are among the advantages of the proposed methodology. The road experiments confirmed that the proposed algorithm can estimate separate and combined bank/grade road angles in various driving conditions.

Chapter 4

Tire Force Estimation

Tire forces exhibit the vehicle's capacity to perform requested maneuvers and provide information about the stability of the vehicle. Tire forces can be measured at each corner using wheel force/moment sensors, but their cost impact and maintenance are their major drawbacks to be used for production vehicles. Therefore, estimation of the longitudinal, lateral, and vertical tire forces using measurements available on current production vehicles, yet robust to different road conditions has been the main focus of related literature in recent years, and the topic of this chapter. In the following, corner-based longitudinal force estimation methodologies and their stability are first discussed using a nonlinear and a Kalman observer on the wheel dynamics. The lateral force estimator on the vehicle planar kinetics is then introduced by employing an unscented Kalman filter. Vertical force estimation at each corner are estimated employing the roll and pitch effects of the vehicle sprung mass. Road experiments and co-simulation between MATLAB/Simulink and CarSim packages are performed to check the performance of the approach in diverse driving and on different road conditions.

4.1 Introduction

Developing longitudinal, lateral, and vertical tire force estimators using conventional sensor measurement (wheel speed, accelerations, steering angle, and wheel torques) robust to

the road friction changes is desirable. Such estimation structures are presented and experimentally verified in this section. Longitudinal and lateral force estimation significantly contributes to dynamic-based velocity estimators ([22,57,58]) and stability control systems ([61,95,96]). Neglecting the bearing's viscous damping, one can write the wheel dynamic equation as follows with $i \in \{f, r\}$ (front and rear axles) and $j \in \{L, R\}$ (left and right tires):

$$F_{x_{ij}} = \frac{1}{R_e}(T_{t_{ij}} - I_w \dot{\omega}_{ij}) + \mathbf{w}_x, \tag{4.1}$$

where R_e is the wheel effective rolling radius, T_t represents the total effective torque on the wheel, F_x is the longitudinal tire force, $\dot{\omega}$ is the wheel acceleration, I_w is the wheel's moment of inertia and $\mathbf{w}_x$ represents uncertainties in the model including the effective radius, torque, etc.

Model-based stability control systems and lateral velocity estimators use lateral forces at each corner. The sum of longitudinal/lateral forces at each axle i.e. $F_{x_i} = \sum_j F_{x_{ij}}$ and $F_{y_i} = \sum_j F_{y_{ij}}$ are utilized for the longitudinal and lateral dynamics:

$$\begin{aligned} m\check{a}_x &= F_{x_f}\cos\delta - F_{y_f}\sin\delta + F_{x_r} + \mathbf{w}_{f_x} \\ m\check{a}_y &= F_{y_f}\cos\delta + F_{x_f}\sin\delta + F_{y_r} + \mathbf{w}_{f_y} \end{aligned} \tag{4.2}$$

in which δ is the steering angle (with parallel steering in front wheels) and $\mathbf{w}_{f_x}, \mathbf{w}_{f_y}$ represent longitudinal and lateral uncertainties due to the acceleration measurement, geometry, and forces. The measured longitudinal and lateral accelerations include the kinematics of the vehicle's CG V_x, V_y, vehicle's body pitch/roll angles θ_v, ϕ_v, and road grade/bank angles θ_r, ϕ_r. Therefore, acceleration measurements a_x, a_y are corrected with the road and body's roll/pitch angles as

$$\check{a}_x = a_x - g\sin\theta_t, \quad \check{a}_y = a_y - g\sin\phi_t \tag{4.3}$$

where $\theta_t = \theta_v + \theta_r$ and $\phi_t = \phi_v + \phi_r$.

The derivative of the yaw rate r is also related to the sum of forces at each axles as:

$$\begin{aligned} I_z\dot{r} &= (F_{y_f}\cos\delta + F_{x_f}\sin\delta)d_f \\ &\quad + (\bar{F}_{x_f}\cos\delta - \bar{F}_{y_f}\sin\delta)\frac{T_{r_f}}{2} - F_{y_r}d_r + \bar{F}_{x_r}\frac{T_{r_r}}{2} + \mathbf{w}_r, \end{aligned} \tag{4.4}$$

in which T_{r_f}, T_{r_r} are the length of front and rear tracks respectively as shown in Fig. 4.1-a. Forces and relative velocities in the tire coordinates are also depicted in Fig. 4.1-b. The distances from the front and rear axles' to CG are denoted by d_f, d_r, uncertainties due to the CG location, yaw rate measurement, and forces are represented by $\mathbf{w}_r$, and $\bar{F}_{x_i} = F_{x_{iR}} - F_{x_{iL}}, \bar{F}_{y_i} = F_{y_{iR}} - F_{y_{iL}}$.

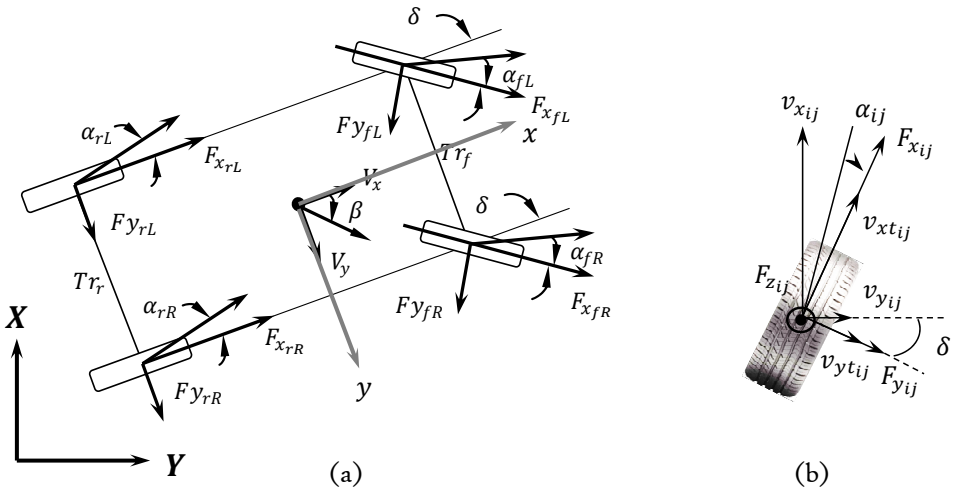

Figure 4.1: Forces and velocities in (a) planar vehicle model (b) tire coordinates.

The corner-based state estimation structure is illustrated in Fig. 4.2, in which the estimated vehicle angles from the *Roll/Pitch Est.* module are fed to the *Vertical Force Est.* block. The *Longitudinal/Lateral Force Est.* module incorporates torques and the wheel speeds at each corner for the longitudinal force estimation. It uses longitudinal/lateral accelerations as well as the yaw rate for the lateral force estimation and does not require the road condition. Measured accelerations by IMU attached to the sprung mass are corrected with the vehicle's body pitch and roll angles from *Pitch/Roll Angle Est.* to include only the kinematics of the motion. These corrected values are then used for the vertical and lateral force estimators.

The developed force estimation structure are experimentally tested and the results confirm good performance such that it can be utilized in vehicle's active safety systems or model-based velocity estimators.

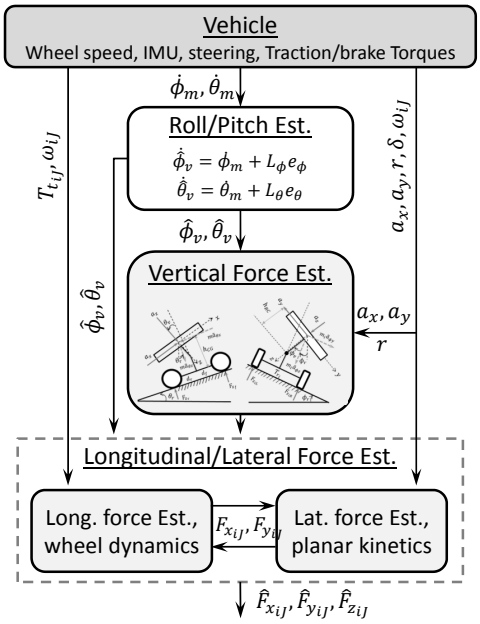

Figure 4.2: Corner-based force estimation structure

4.2 Longitudinal Force Estimation

Provided that the longitudinal tire force calculation needs road friction, even accurate slip ratio information from the GPS will not provide forces at each corner. Hence, estimation of tire forces independent of road conditions would be a remedy. Longitudinal force estimation independent of the road friction may be classified on the basis of wheel dynamics into the nonlinear and sliding mode observers [25, 34, 89], Kalman-based estimation [35, 40], and unknown input observers [38, 97]. This section provides two computationally efficient nonlinear observers for the longitudinal force estimation on various road friction conditions.

4.2.1 Observer-based force estimation

The corner-based estimation approach proposed in this subsection for the longitudinal force estimation, uses a PID state observer [98, 99] that has also been used in other applications.

The longitudinal force estimate is expressed as:

$$\hat{F}_{x_{ij}} = \frac{T_{t_{ij}} - I_w \dot{\omega}_{ij}}{R_e} - k_1 \tilde{\omega}_{ij} + k_3 \int \tilde{F}_{x_{ij}} dt \tag{4.5}$$

where k_1, k_3 are design parameters. The estimated wheel speed $\hat{\omega}$ at each corner ij is described as:

$$\dot{\hat{\omega}}_{ij} = \frac{1}{I_w}(T_{t_{ij}} - R_e \hat{F}_{x_{ij}} + k_2 \int \tilde{\omega}_{ij} dt + R_e k_3 \int \tilde{F}_{x_{ij}} dt) \tag{4.6}$$

in which k_2 is a design parameter, $\tilde{\omega}_{ij} = \omega_{ij} - \hat{\omega}_{ij}$, and $\tilde{F}_{x_{ij}} = F_{x_{ij}} - \hat{F}_{x_{ij}}$ is the longitudinal force estimation error.

Theorem 1. *The error dynamics for the longitudinal estimator (4.5) on the wheel dynamics with time-varying parameter ω_{ij} is asymptotically bounded by $\sup_{t\geq 0} \frac{|\dot{\mathbf{w}}_x|}{k_3}$.*

Proof. : Subtracting the longitudinal force (4.1) from the estimated longitudinal force (4.5) leads to the estimation error $\tilde{F}_{x_{ij}}$. This force estimation error can be described as $\tilde{F}_{x_{ij}} = -k_3 \int \tilde{F}_{x_{ij}} dt + k_1 \tilde{\omega}_{ij} + \mathbf{w}_x$. The time derivative of the error dynamic yields $\dot{\tilde{F}}_{x_{ij}} = \mathcal{A}_x \tilde{F}_{x_{ij}} + \mathcal{B}_x \dot{\tilde{\omega}}_{ij} + \dot{\mathbf{w}}_x$ with $\mathcal{A}_x = -k_3$ and $\mathcal{B}_x = k_1$. The discretized form of the longitudinal force error dynamics is:

$$\dot{\tilde{F}}_{x_{ij_{k+1}}} = \bar{\mathcal{A}}_x \tilde{F}_{x_{ij_k}} + \bar{\mathcal{B}}_x \dot{\tilde{\omega}}_{ij_k} + \dot{\mathbf{w}}_{x_k} \tag{4.7}$$

where $\bar{\mathcal{A}}_x, \bar{\mathcal{B}}_x$ are the discretized state and input matrices obtained by step-invariance discretization method described in section 3.3 for real-time implementation. Substituting $\hat{F}_{x_{ij}}$ from (4.5) in (4.6), one can rewrite:

$$\dot{\hat{\omega}}_{ij} = \dot{\omega}_{ij} + \frac{1}{I_w}(R_e k_1 \tilde{\omega}_{ij} + k_2 \int \tilde{\omega}_{ij} dt). \tag{4.8}$$

The deviation of the estimated wheel speed from the measured one is denoted by $\tilde{\omega}$ and incorporated for the force estimation as in (4.5). Subtracting the estimated wheel speed (4.8) from the wheel speed by the wheel dynamics (4.1) results in $I_w \dot{\tilde{\omega}}_{ij} = -R_e \tilde{F}_{x_{ij}} + R_e \mathbf{w}_x - k_2 \int \tilde{\omega}_{ij} - R_e k_3 \int \tilde{F}_{x_{ij}} dt$. Taking time derivative and replacing the error dynamics $\dot{\tilde{F}}_{x_{ij}} = -k_3 \tilde{F}_{x_{ij}} + k_1 \dot{\tilde{\omega}}_{ij} + \dot{\mathbf{w}}_x$ leads to $I_w \ddot{\tilde{\omega}}_{ij} + R_e k_1 \dot{\tilde{\omega}}_{ij} + k_2 \tilde{\omega}_{ij} = 0$ which is in the discretized state space form:

$$\mathbf{x}_{\omega_{k+1}} = \bar{\mathcal{A}}_\omega \mathbf{x}_{\omega_k}, \tag{4.9}$$

with states $\mathbf{x}_\omega = [\tilde{\omega} \quad \dot{\tilde{\omega}}]^T$. The discretized state matrix is $\bar{\mathcal{A}}_\omega = e^{A_\omega T_s}$ where:

$$\mathcal{A}_\omega = \begin{bmatrix} 0 & 1 \\ \frac{-k_2}{I_w} & \frac{-R_e k_1}{I_w} \end{bmatrix}. \tag{4.10}$$

The matrix $\mathcal{A}_\omega$ is Hurwitz and (4.10) is exponentially stable given $k_1, k_2 > 0$, therefore, $\mathbf{x}_\omega \to 0$ (i.e. $\tilde{\omega}_{ij} \to 0$ and $\dot{\tilde{\omega}}_{ij} \to 0$). Thus, the estimation error dynamics (4.7) asymptotically turns to

$$\tilde{F}_{x_{ij_{k+1}}} = \bar{\mathcal{A}}_x \tilde{F}_{x_{ij_k}} + \dot{\mathbf{w}}_{x_k}, \tag{4.11}$$

that is an exponentially stable dynamic for $\forall k_3 > 0$. Moreover, since $\tilde{\omega}_{ij}$ asymptotically converges to zero, by solving (4.11) one can get $\tilde{F}_{x_{ij}}(t) = e^{-k_3 t}\tilde{F}_{x_{ij}}(0) + \frac{\dot{\mathbf{w}}_x}{k_3}$. As $e^{-k_3 t}\tilde{F}_{x_{ij}}(0)$ exponentially converges to zero, $\tilde{F}_{x_{ij}}(t)$ will be asymptotically bounded by $\sup_{t\geq 0} \frac{|\dot{\mathbf{w}}_x|}{k_3}$. □

4.2.2 Kalman-based force estimation

This section utilizes UKF for longitudinal force estimation. Estimation problems can be addressed by UKF for the discrete-time nonlinear system of the form $x_{k+1} = \mathcal{F}(x_k, u_k, f, n_{pk})$, $y_k = \mathcal{H}(x_k, f, n_{mk})$. Parameters f and system states x_k can be estimated recursively from the noisy output y_k. Uncertainties in the process and measurements are incorporated into the nonlinear system definition as n_{pk}, n_{mk}. Proper capturing of nonlinearities contributes to the unscented transformation that defines the Sigma vectors $\mathcal{X} \in \mathbb{R}^{N\times 2N+1}$, ($N$ is the length of the state vector), which are supposed to propagate through the nonlinear system. With some minor changes, UKF can also be employed for parameter estimation instead of state estimation for the vehicle parameter identification [100, 101] and for the longitudinal force estimation [40]. For the force estimation with UKF, the effective torque T_t provides input u_k; the wheel speed is assumed to be the state x_k, and the estimated longitudinal force $\hat{F}_x$ is denoted by the estimated parameter $\hat{f}$. The discrete-time parameter estimation problem can be expressed as $f_{k+1} = f_k + \varrho_k$ and $z_k = \mathcal{G}(x_k, f_k) + \nu_k$, where z_k corresponds to nonlinear observation on f_k and ϱ_k, ν_k represent process and observation noises respectively. In a parameter estimation problem, the estimated mean is updated as $\hat{f}_{mk} = \hat{f}_{k-1}$ and initialized by $\hat{f}_0 = \mathbb{E}[f]$. The moving sample points i.e. sigma vector $F_{k|k-1}$ are generated around the estimated mean $\hat{f}_{mk}$ with the conventional unscented transformation

pattern $F_{k|k-1} = \begin{bmatrix} \hat{f}_{mk} & \hat{f}_{mk} + \bar{\tau}\sqrt{\bar{P}_{f_k}} & \hat{f}_{mk} - \bar{\tau}\sqrt{\bar{P}_{f_k}} \end{bmatrix}$, where square root factorization of the covariance matrix $\bar{P}_{f_k}$ is obtained by Cholesky decomposition at each time step k.

The error covariance matrix of the estimated parameter is initialized with $P_{f_0} = \mathbb{E}\left[(f - \hat{f}_0)(f - \hat{f}_0)^T\right]$ and updated by $\bar{P}_{f_k} = P_{f_{k-1}} + Q_{k-1}$ with incorporation of the process noise covariance Q_{k-1}. Furthermore, $\bar{\tau}$ is a scalar and represents the spread of the sample points far from the mean values of random variables (states). It is defined in [102] as $\bar{\tau} = \sqrt{N + \bar{\eta}}$, where $\bar{\eta}$ is the compound scaling parameter $\bar{\eta} = \bar{\epsilon}^2 N - N$. Spread of the sample points around $\hat{f}_{mk}$ is denoted by $\bar{\epsilon} = \sqrt{3/N}$. Afterward, $\bar{\beta} = 2$ is introduced to employ the prior information on the Gaussian distribution of x. Sample points are supposed to be propagated within the system (wheel dynamics) as $\mathcal{Z}_{k|k-1} = \mathcal{G}(x_k, F_{k|k-1})$, and the estimated function output $\hat{z}_k$ is achievable from $\hat{z}_k = \sum_{i=0}^{2N} W_i^m \mathcal{Z}_{i,k|k-1}$. The weighting parameters are also defined by $W_i^c = W_i^m = \frac{1}{2}(N + \bar{\eta})$ for all sets $i \in \{1, 2, \ldots, 2N\}$. These parameters are $W_0^c = \frac{\bar{\eta}}{N+\bar{\eta}} + 1 - \bar{\epsilon}^2 + \bar{\beta}$ and $W_0^m = \frac{\bar{\eta}}{N+\bar{\eta}}$ for $i = 0$. The updated covariance matrices are given in (4.12) using the measurement noise covariance R_k:

$$
\begin{aligned}
P_{z_k z_k} &= \sum_{i=0}^{2N} W_i^c (\mathcal{Z}_{i,k|k-1} - \hat{z}_k)(\mathcal{Z}_{i,k|k-1} - \hat{z}_k)^T + R_k, \\
P_{f_k z_k} &= \sum_{i=0}^{2N} W_i^c (F_{i,k|k-1} - \hat{f}_{mk})(\mathcal{Z}_{i,k|k-1} - \hat{z}_k)^T.
\end{aligned} \tag{4.12}
$$

The Kalman gain is achievable, by implementing these covariance matrices as $K_k = P_{f_k z_k} P_{z_k z_k}^{-1}$. As a result, the updated parameter and error covariance matrices can be obtained as follows [102]:

$$
\begin{aligned}
P_{fk} &= \bar{P}_{fk} - K_k P_{z_k z_k} K_k^T, \\
\hat{f}_k &= \hat{f}_{mk} + K_k (z_k - \hat{z}_k),
\end{aligned} \tag{4.13}
$$

where $\hat{f}_k$ is the updated longitudinal force estimate $\hat{F}_{x_{ij}}$ at each corner. The UKF moving sigma points through the wheel dynamics reduce the estimation fluctuations, even with the presence of major uncertainties such as the road friction and changes in the effective radius. Outcomes of the UIO and UKF approaches are compared in Section 4.5. Longitudinal force estimation with the observer-based scheme (4.5) is selected and utilized for the lateral force estimation in the next section and velocity estimation in the next Chapter.

4.3 Lateral Force Estimation

Longitudinal forces at each corner i.e. $F_{x_{ij}}$ are assumed to be available from (4.5) in the previous subsection. Set of equations (4.4) together with the longitudinal and lateral dynamics can be solved for the lateral forces $F_{y_{ij}}$ at each corner with the assumption of lateral force distribution based on the normal forces, but this may not address maneuvers in which road friction under each tire is different. To resolve this, a method for the lateral force estimation is proposed in this section that uses longitudinal forces and accelerations a_x, a_y and the yaw rate r measurements from a 3-axis IMU.

The set of equations (4.4) can be rewritten in the following lateral force estimator with states $\mathbf{x}_f = [F_{y_f} \quad F_{y_r} \quad \bar{F}_{y_f}]^T$ and output (measurement) $\mathbf{y}_f = [\check{a}_x \quad \check{a}_y \quad r]^T$ where $\check{a}_x, \check{a}_y$ are the corrected values from (4.3):

$$\begin{aligned} \dot{\mathbf{x}}_f &= \mathcal{A}_f \mathbf{x}_f + \mathbf{w}_f, \\ \mathbf{y}_f &= \mathcal{C}_f(\delta)\mathbf{x}_f + \mathbf{u}_f + \mathbf{v}_f \end{aligned} \tag{4.14}$$

where $\mathcal{A}_f = \mathbf{0}_{3\times 3}$ and uncertainties in the process and measurements are denoted by $\mathbf{w}_f$ and $\mathbf{v}_f$. The output matrix $\mathcal{C}_f(\delta)$ and $\mathbf{u}_f$ are defined as:

$$\begin{aligned} \mathcal{C}_f(\delta) &= \begin{bmatrix} -\frac{1}{m}\sin\delta & 0 & 0 \\ \frac{1}{m}\cos\delta & \frac{1}{m} & 0 \\ \frac{1}{I_z}\cos\delta d_f & -\frac{1}{I_z}d_r & \frac{1}{2I_z}\sin\delta T_{r_f} \end{bmatrix}, \\ \mathbf{u}_f &= \begin{bmatrix} \frac{1}{m}(F_{xf}\cos\delta + F_{xr}) \\ \frac{1}{m}F_{xf}\sin\delta \\ \frac{1}{I_z}(F_{xf}\sin\delta d_f + \bar{F}_{xf}\cos\delta\frac{T_{r_f}}{2} + \bar{F}_{xr}\frac{T_{r_r}}{2}) \end{bmatrix}, \end{aligned} \tag{4.15}$$

The matrix $\mathcal{C}_f(\delta)$ is time-varying and physically bounded (because of the steering angle and its derivative). The observability matrix for the time-varying system (4.14) can be written as [103, 104]:

$$\begin{aligned} \mathcal{O}_n &= [\tau_1 \quad \tau_2 ... \quad \tau_n]^T \\ \tau_1 = \mathcal{C}_f, \quad \tau_{i+1} &= \tau_i \mathcal{A}_f(t) + \dot{\tau}_i, \end{aligned} \tag{4.16}$$

Observability of the system (4.14) is confirmed by holding the full rank condition $rank(\mathcal{O}_3) = 3$ for the operating regions of the steering angle and its time derivatives except for the case where $\delta = 0, k\pi$ for integer values of k. For the case where $\delta = 0$ we have $rank(\mathcal{C}_f) = 2$. However, in this case there is no lateral force applied to the tire. Moreover, situations $\delta = k\pi$ do not take place, due to the fact that the maximum value of the steering angle is much less than $\pi/2$.

Stability of the estimator: Observability is a sufficient condition for implementation of an optimal variance filter (such as a Kalman estimator). Therefore, a Kalman-based observer can be employed on system (4.14) with the discretized form of:

$$\begin{aligned} \mathbf{x}_{f_{k+1}} &= \bar{\mathcal{A}}_{f_k}\mathbf{x}_{f_k} + \mathbf{w}_{f_k} \\ \mathbf{y}_{f_k} &= \bar{\mathcal{C}}_{f_k}\mathbf{x}_{f_k} + \mathbf{u}_{f_k} + \mathbf{v}_{f_k}, \end{aligned} \tag{4.17}$$

which have the noise covariances $Q_{f_k} = \mathbb{E}[\mathbf{w}_{f_k}, \mathbf{w}_{f_k}{}^T], R_{f_k} = \mathbb{E}[\mathbf{v}_{f_k}, \mathbf{v}_{f_k}{}^T]$ for the model and measurements, respectively. The discretized forms of state and output matrices are denoted by $\bar{\mathcal{A}}_{f_k}, \bar{\mathcal{C}}_{f_k}$. Process and measurement noises are assumed to be uncorrelated $\mathbb{E}[\mathbf{w}_{f_k}, \mathbf{v}_{f_k}{}^T] = 0$ and have zero mean $\mathbb{E}[\mathbf{w}_{f_k}] = \mathbb{E}[\mathbf{v}_{f_k}] = 0; \forall k \in \mathbb{N}$.

The discrete-time Kalman observer suggests the following prediction with correction to estimate the states defined by $\hat{\mathbf{x}}_{f_{k+1|j}} \triangleq \mathbb{E}[\mathbf{x}_{f_k}|\mathbf{y}_{f_j}]$ using a sequence of measurements y_j:

$$\hat{\mathbf{x}}_{f_{k+1|k}} = \bar{\mathcal{A}}_{f_k}\hat{\mathbf{x}}_{f_{k|k-1}} + K_k(\mathbf{y}_{f_k} - \bar{\mathcal{C}}_{f_k}\hat{\mathbf{x}}_{f_{k|k-1}}), \tag{4.18}$$

where the optimal Kalman gain is $K_k = \bar{\mathcal{A}}_{f_k}P_{k|k-1}\bar{\mathcal{C}}_{f_k}^T(\bar{\mathcal{C}}_{f_k}P_{k|k-1}\bar{\mathcal{C}}_{f_k}^T + R_{f_k})^{-1}$ and error covariance $P_{k+1|k} \triangleq cov(\hat{\mathbf{x}}_{f_{k+1}} - \hat{\mathbf{x}}_{f_{k+1|k}})$ forms a discrete time-varying Riccati equation (4.19) for both zero and non-zero state initialization $\hat{\mathbf{x}}_{f_{0|-1}} = \mathbb{E}[\mathbf{x}_{f_0}]$:

$$P_{k+1|k} = \bar{\mathcal{A}}_{f_k}P_{k|k-1}\bar{\mathcal{A}}_{f_k}^T + Q_{f_k} - K_k\bar{\mathcal{C}}_{f_k}P_{k|k-1}\bar{\mathcal{A}}_{f_k}^T, \tag{4.19}$$

where the state covariance is initialized as $P_{0|-1} \triangleq cov(\mathbf{x}_{f_0}) = \mathbb{E}\left[(\mathbf{x}_{f_0} - \hat{\mathbf{x}}_{f_{0|-1}})(\mathbf{x}_{f_0} - \hat{\mathbf{x}}_{f_{0|-1}})^T\right]$. The estimation error is defined by $\mathbf{e}_{f_{k+1|j}} \triangleq \mathbf{x}_{f_{k+1}} - \hat{\mathbf{x}}_{f_{k+1|j}}$, which yields:

$$\mathbf{e}_{f_{k+1|k}} = (\bar{\mathcal{A}}_{f_k} - K_k\bar{\mathcal{C}}_{f_k})\mathbf{e}_{f_{k|k-1}} - K_k\mathbf{w}_{f_k} + \mathbf{v}_{f_k}. \tag{4.20}$$

The observability of the system (4.14) results in stability of the presented model-based estimation and consequently the error dynamics (4.20); thus, errors of the state mean have bounded variance.

The unscented Kalman filter (UKF) [36, 105] is utilized on the discretized from of (4.17) for the lateral force estimation at each corner to include non-Gaussian noises and to have more smooth estimation because of having mean values for propagated sample points within the system. The UKF employs a transformation to include nonlinear characteristics of the system $\mathbf{x}_{f_{k+1}} = \mathcal{F}(\mathbf{x}_{f_k}, \mathbf{u}_{fk}, \mathbf{w}_{f_k})$ and $\mathbf{y}_{f_k} = \mathcal{G}(\mathbf{x}_{f_k}, \mathbf{v}_{f_k})$ with process and measurement uncertainties $\mathbf{w}_{f_k}, \mathbf{v}_{f_k}$ and the covariance matrices Q_{f_k}, R_{f_k} in a recursive estimation procedure.

The Procedure 1 illustrates the lateral force estimation with UKF in which the proper capturing of nonlinearities contributed to the unscented transformation that defines Sigma vectors $\mathbf{\Sigma} \in \mathbb{R}^{N \times 2N+1}$ (N is the length of the state vectors) around $\mathbf{x}_k$. This propagation yields nonlinear stochastic characteristics of the random variables and results in getting the posterior mean and covariance up to second-order approximation [102, 106]. The square root factorization of the covariance matrix $\mathbf{P}_{k-1}$ is obtained by Cholesky decomposition at each time step k. Spread of the sigma points far from the mean values of random variables (states) are shown by the scalar $\bar{\tau}$. Scalars $\bar{\tau}, \bar{\eta}, \bar{\epsilon}$ and weights W_i^c, W_i^m for $i \in \{0, 1, 2, \ldots, 2N\}$ are defined in Section 4.2. The parameter $\bar{\beta} = 2$ is also introduced to employ the prior information on the distribution of states $\mathbf{x}_f$. Optimality and convergence of the UKF state estimation method is also discussed in [105].

4.4 Vertical Force Estimation

Vertical forces are required for the stability control and roll-over prevention systems. Estimation of the vertical forces at each corner is addressed in this subsection using lateral and longitudinal vehicle dynamics and the sprung mass angles. The effects of the vehicle body's vertical motion and the roll/pitch angles are not commonly considered in the existing vertical force estimation methods [35, 37]. To address this issue, the vertical force estimator module is developed in this section using lateral and longitudinal vehicle dynamics and incorporation of the vehicle angles ϕ_v, θ_v from [107]. The sprung mass roll and pitch angles ϕ_v, θ_v are not achievable by integration over the roll and pitch rate signals $\dot{\phi}_m, \dot{\theta}_m$ because of sensor noises and accumulate error problem. Rehm provided a linear observer with low-pass filtering in [107] to estimate the vehicle body's roll/pitch angles

Procedure 1: LATERAL FORCE ESTIMATION by UKF

// Systems: (The discretized estimator (4.17))

$\mathbf{x}_{f_{k+1}} = \mathcal{F}(\mathbf{x}_{f_k}, \mathbf{u}_{fk}, \mathbf{w}_{f_k}) = \bar{\mathcal{A}}_{f_k}\mathbf{x}_{f_k} + \mathbf{w}_{f_k}$

$\mathbf{y}_{f_k} = \mathcal{G}(\mathbf{x}_{f_k}, \mathbf{v}_{f_k}) = \bar{\mathcal{C}}_{f_k}\mathbf{x}_{f_k} + \mathbf{u}_{f_k} + \mathbf{v}_{f_k}$

// Sample points in system dynamics:

$\mathbf{\Sigma}_{k-1} = [\hat{\mathbf{x}}_{f_{k-1}} \quad \hat{\mathbf{x}}_{f_{k-1}} + \bar{\tau}\sqrt{\mathbf{P}_{k-1}} \quad \hat{\mathbf{x}}_{f_{k-1}} - \bar{\tau}\sqrt{\mathbf{P}_{k-1}}]$

$\mathbf{\Sigma}_{k|k-1} = \mathcal{F}(\mathbf{\Sigma}_{k-1}, \mathbf{u}_{f_{k-1}})$

$\mathbf{\Lambda}_{k|k-1} = \mathcal{G}(\mathbf{\Sigma}_{k|k-1}, \mathbf{\Sigma}_{k-1})$

// Optimal prediction of the mean, output, and covariance:

$\hat{\mathbf{x}}_{mk} = \sum_{i=0}^{2N} W_i^m \mathbf{\Sigma}_{i,k|k-1}$, $\hat{\mathbf{y}}_{mk} = \sum_{i=0}^{2N} W_i^m \mathbf{\Lambda}_{i,k|k-1}$

$\mathbf{P}_{mk} = \sum_{i=0}^{2N} W_i^c (\mathbf{\Sigma}_{i,k|k-1} - \hat{\mathbf{x}}_{mk})(\mathbf{\Sigma}_{i,k|k-1} - \hat{\mathbf{x}}_{mk})^T + Q_{f_k}$

// Modified covariance matrices:

$\mathbf{P}_{\tilde{\mathbf{x}}_{f_k}\tilde{\mathbf{y}}_{f_k}} = \sum_{i=0}^{2N} W_i^c (\mathbf{\Sigma}_{i,k|k-1} - \hat{\mathbf{x}}_{mk})(\mathbf{\Lambda}_{i,k|k-1} - \hat{\mathbf{y}}_{mk})^T$

$\mathbf{P}_{\tilde{\mathbf{y}}_{f_k}\tilde{\mathbf{y}}_{f_k}} = \sum_{i=0}^{2N} W_i^c (\mathbf{\Lambda}_{i,k|k-1} - \hat{\mathbf{y}}_{mk})(\mathbf{\Lambda}_{i,k|k-1} - \hat{\mathbf{y}}_{mk})^T + R_{f_k}$

// State and covariance update:

$K_k = \mathbf{P}_{\tilde{\mathbf{x}}_{f_k}\tilde{\mathbf{y}}_{f_k}} \mathbf{P}^{-1}_{\tilde{\mathbf{y}}_{f_k}\tilde{\mathbf{y}}_{f_k}}$

$\hat{\mathbf{x}}_{f_k} = \hat{\mathbf{x}}_{mk} + K_k(\mathbf{y}_{f_k} - \hat{\mathbf{y}}_{mk})$

$\mathbf{P}_k = \mathbf{P}_{mk} - K_k \mathbf{P}_{\tilde{\mathbf{y}}_{f_k}\tilde{\mathbf{y}}_{f_k}} K_k^T$

---

as $\dot{\hat{\phi}}_v = \dot{\phi}_m + L_\phi e_\phi, \dot{\hat{\theta}}_v = \dot{\theta}_m + L_\theta e_\theta$ by compensation over the error between the filtered estimates and the stationary roll/pitch values i.e. e_ϕ, e_θ and the observer gains L_ϕ, L_θ

Normal forces at each axle/tire and the longitudinal, lateral, and vertical components of the accelerations in SAE vehicle chassis coordinates i.e $\underline{a}_{\theta x}, \underline{a}_{\theta z}$ and $\underline{a}_{\phi y}, \underline{a}_{\phi z}$ are schematically illustrated in Fig. 4.3.

The longitudinal and vertical acceleration components of the longitudinal dynamics are defined as

$$\begin{aligned} \underline{a}_{\theta x} &= a_x \cos\theta_v + a_z \sin\theta_v \\ \underline{a}_{\theta z} &= a_z \cos\theta_v - a_x \sin\theta_v, \end{aligned} \tag{4.21}$$

The measured longitudinal and vertical accelerations a_x, a_z by an IMU attached to the sprung mass are affected by the vehicle pitch angle θ_v, and the road grade angle θ_r. Normal

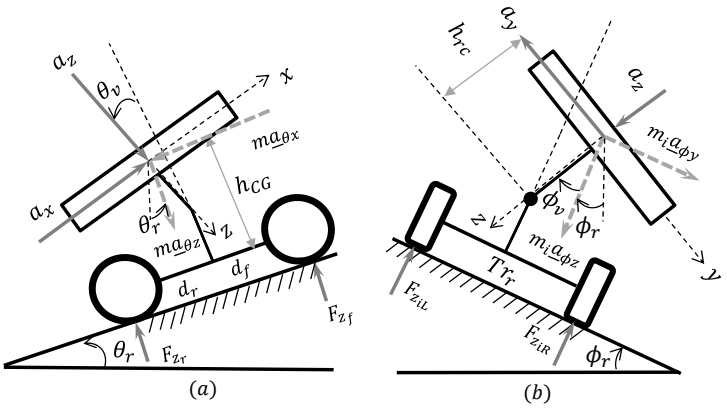

Figure 4.3: (a) pitch model (b) roll model

forces at front and rear axles, thus can be calculated by:

$$\begin{aligned} F_{z_f} &= -\frac{m}{d_f + d_r}(h_{CG}\tilde{a}_{\theta x} - d_r \underline{a}_{\theta z}) \\ F_{z_r} &= \frac{m}{d_f + d_r}(h_{CG}\tilde{a}_{\theta x} + d_f \underline{a}_{\theta z}), \end{aligned} \tag{4.22}$$

in which the height of the vehicle's center of gravity is h_{CG}. Similarly, the lateral and vertical acceleration components of the lateral dynamics are defined by:

$$\begin{aligned} \underline{a}_{\phi y} &= a_y \cos\phi_v + a_z \sin\phi_v \\ \underline{a}_{\phi z} &= a_z \cos\phi_v - a_y \sin\phi_v, \end{aligned} \tag{4.23}$$

The measured lateral acceleration a_y contains the vehicle roll ϕ_v angle and the road bank angle ϕ_r. Defining equivalent masses at each axle $m_i = \frac{F_{z_i}}{g}, i \in \{f, r\}$ with F_{z_f}, F_{z_r} from (4.22), one can express normal forces in the left and right sides of the vehicle as:

$$\begin{aligned} F_{z_{iL}} &= \frac{m_i}{Tr_i}\left[\underline{a}_{\phi z}(\frac{Tr_i}{2} - h_{rc}\sin\phi_v) - \underline{a}_{\phi y}h_{CG}\right] \\ F_{z_{iR}} &= \frac{m_i}{Tr_i}\left[\underline{a}_{\phi z}(\frac{Tr_i}{2} + h_{rc}\sin\phi_v) + \underline{a}_{\phi y}h_{CG}\right], \end{aligned} \tag{4.24}$$

in which h_{rc} is the height of the roll center. The velocity estimator in the next chapter requires normalization of the longitudinal/lateral forces. Thus, estimated forces should be

normalized as (4.25)

$$\mu_{x_{ij}} = F_{x_{ij}}/F_{z_{ij}} \quad \mu_{y_{ij}} = F_{y_{ij}}/F_{z_{ij}}, \tag{4.25}$$

at each corner ij using calculated vertical forces in the vehicle coordinate frame. Finally, the proposed force estimation approaches are verified in simulations and experimentally validated on various road conditions using a full-size test vehicle with AWD and FWD powertrain configurations.

4.5 Simulation and Experimental Results

Experimental and simulation results are presented in this section to validate the proposed force estimators on the AWD instrumented SUV with the specifications given in Table 3.1. The Controller & Estimator module requires longitudinal and lateral accelerations, yaw rate, wheel speed as well as the wheel torques, which are measured by CAN-bus communication using an IMU, regular ABS wheel speed sensors, and electric actuators (Fig. 4.4-a) respectively. The sampling time for the experiment is set to be 0.005 [s].

(a) (b)

Figure 4.4: (a) Electric motors (b) wheel hub sensors for force/moment measurement.

To validate the estimated forces, this vehicle is equipped with additional sensors for direct measurement of tire forces and moments at each corner as shown in as shown in

Fig. 4.4-b. Different driveline configurations are used to verify the force estimators. The AWD test vehicle has the capability of being used as a front-wheel-drive and its powertrain can be set to the FWD for some tests with high-slip conditions.

4.5.1 Longitudinal force estimator

In Fig. 4.5-a forces estimated by both the UKF and the unknown input observer (UIO) are compared with the CarSim tire forces on a slippery road for a maneuver with successive accelerator and brake pedal requests. The simulation occurs on a slippery road with $\mu = 0.3$, and the initial longitudinal velocity of the vehicle is $V_{x_0} = 30\,[\text{kph}]$.

The proposed force estimation methods are independent of the road condition exhibit and smooth performance for such maneuver with successive sign changes of the slip-ratio. An acceleration-in-turn (AiT) maneuver on dry and slippery roads is simulated in the CarSim and results are graphically illustrated in Fig. 4.5-b. For the AiT driving scenario, the accelerator is applied to 100% at $t = 2\,[\text{s}]$ and continues till $t = 4\,[\text{s}]$. It is released between 4 and 6 [s] and pushed up to 100% again as a step signal till $t = 11\,[\text{s}]$, then it is linearly reduced to zero at $t = 15\,[\text{s}]$. A steering angle $\delta_{sw} = 1\,[\text{rad}]$ is imposed between $t = 2 - 12\,[\text{s}]$ as well and the steering ratio is $r_\delta = 16.7$. The performed combined-slip AiT maneuver is harsh, but the developed UKF by weighted averaging of the sigma points' and the suggested UIO handle the oscillations in the transient regions resulted from imposing and releasing torques on wheels. The fluctuations observed in the CarSim's force profile curves are attributed to the requested acceleration with high magnitude.

Several road experiments such as lane change with brake, double lane change, and brake-in-turn scenarios are conducted on dry and slippery surfaces to show the performance of the force estimators. The selected gains for these road experiments are $k_1 = 1.78$, $k_2 = 11.4$ and $k_3 = 50.6$ and the experimental results are presented in the following.

In order to assess the proposed approach in road experiments with combined-slip conditions, in which the tire capacities are reduced due to high slip ratio as well the high slip angles in each longitudinal/lateral direction, a lane change (LC) maneuver with brake at the end is performed by the AWD vehicle with torque vectoring as the control scheme on a wet surface with $\mu \approx 0.45$. Experimental results of the force estimation at the rear-left wheel in this maneuver are demonstrated in Fig. 4.6 and compared with the measurement.

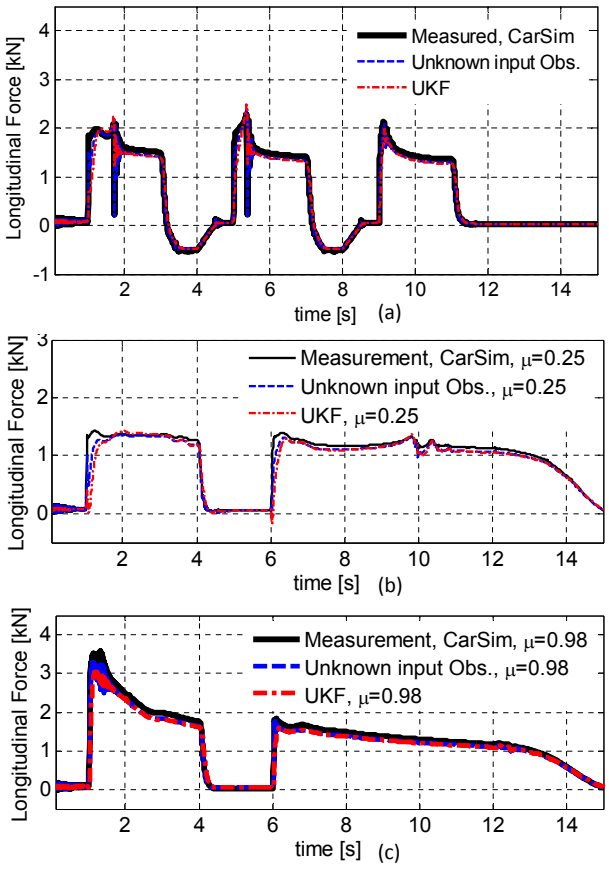

Figure 4.5: Simulation results, estimated forces in CarSim (a) acceleration/brake on a road with $\mu = 0.3$ (b) AiT on a slippery road with $\mu = 0.25$ (c) AiT on dry asphalt.

The Effective torque $T_{t_{rj}}$ and the wheel speed ω_{rj} of the rear wheels are also depicted in Fig. 4.6.

The outcomes show that the developed longitudinal observer can address oscillations due to slippery surfaces in the transient regions. The vehicle speed in this LC with brake on wet road (i.e. Fig. 4.6) changed from 10.9 to 9.6 [m/s] at $t = 11.3$ [s] then decreased to $V_x = 7.3$ [m/s] at the end.

Another test, a double lane change (DLC) maneuver, with high slip and lateral excitation is conducted on a snowy surface with the AWD test vehicle and force estimation results of UIO and the proposed UKF approach are compared in Fig. 4.7 for the rear left

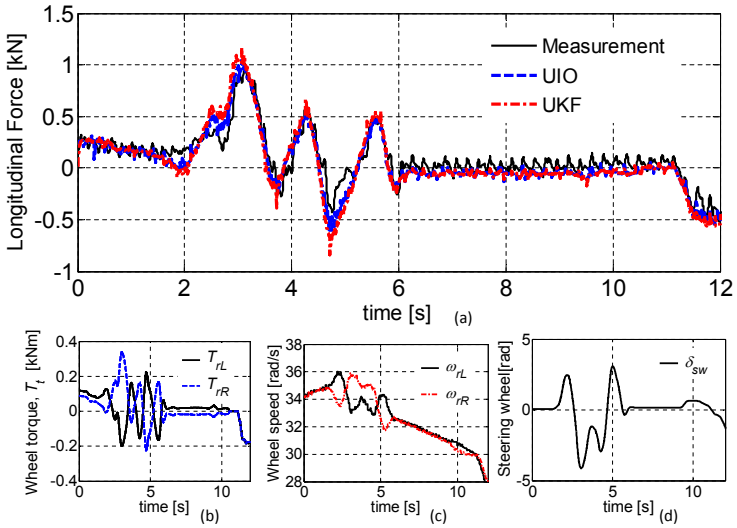

Figure 4.6: Lane change with brake on wet, AWD vehicle (a) estimated $\hat{F}_x$ at rL (b) wheel torques (c) wheel speeds (d) steering wheel angle, δ_{sw}.

wheel. The force peak values in the DLC maneuver (Fig. 4.7) on snow is higher than the wet surface (Fig. 4.6), which shows that the driving on the wet road was not very severe.

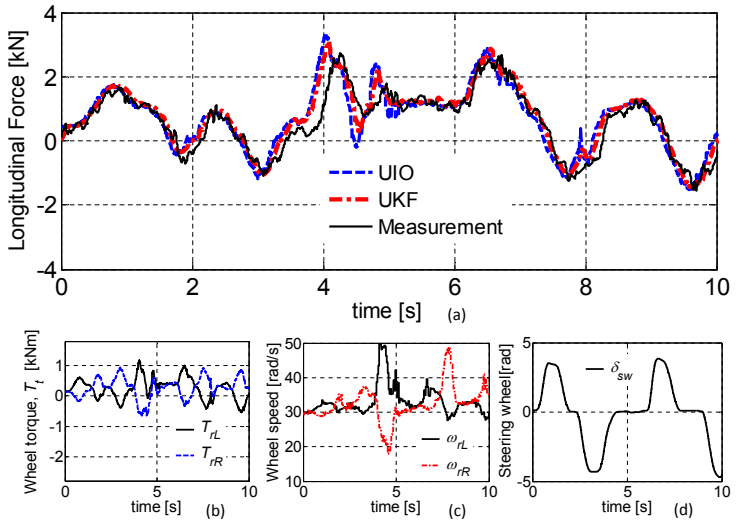

Figure 4.7: DLC on snow with AWD test vehicle (a) estimated $\hat{F}_x$ at rL (b) rear wheel torques (c) rear wheel speeds (d) steering wheel angle.

There is a certain level of correspondence between the outcomes of the two estimation methods and the measurements, even with presence of high slips.

A brake-in-turn (BiT) maneuver accompanied by hard acceleration on the packed snow (with $\mu \approx 0.3$) is also done with winter tires and the UIO force estimation approach is validated by the filtered measurements in Fig. 4.8 at the front-right wheel. For this maneuver the driveline configuration is FWD, tires changed to winter-type with effective rolling radius $R_e = 0.352$[m], and the vehicle started from $V_x = 8.4\,[\mathrm{m/s}]$ and stopped at $t = 10.5\,[\mathrm{s}]$, then accelerated to $3.1\,[\mathrm{m/s}]$ at the end of the experiment.

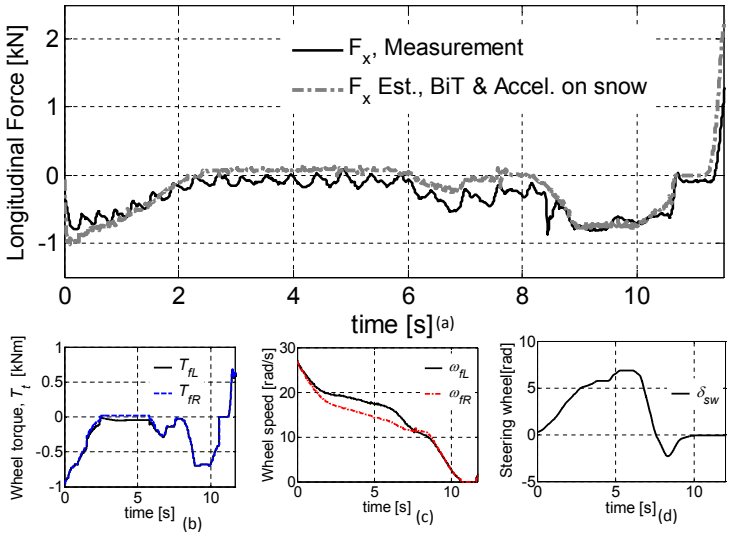

Figure 4.8: BiT and acceleration on snow for FWD case (a) estimated forces at fR with UIO (b) front wheel torques (c) rear wheel speeds (d) steering wheel angle.

The fluctuations observed in the filtered force profile measurement are attributed to the low-stick characteristics of the packed snow. Uncertainties in the effective radius and wheel speed derivative are tackled by tuning the observer gains k_1, k_3 and the observer provides smooth outcomes. The suggested longitudinal observers (4.5) exhibits consistent results for other road experiments on various road frictions as can be seen in Table 4.1.

4.5.2 Lateral and vertical force estimators

Performance of the lateral and vertical force estimators on dry and slippery surfaces is examined in several road experiments with the process and measurement noise covariance matrices $Q_f = 0.13^2\, I_{3\times3}, R_f = 0.012^2\, I_{3\times3}$ for the lateral case. Results of the proposed force estimator in a lane change on the dry road for the AWD case is presented in Fig. 4.9 and compared with the measurement. The measured accelerations and yaw rate are also provided to show the the test conditions. The vehicle speed is $V_x = 12$[m/s] at the beginning of the maneuver.

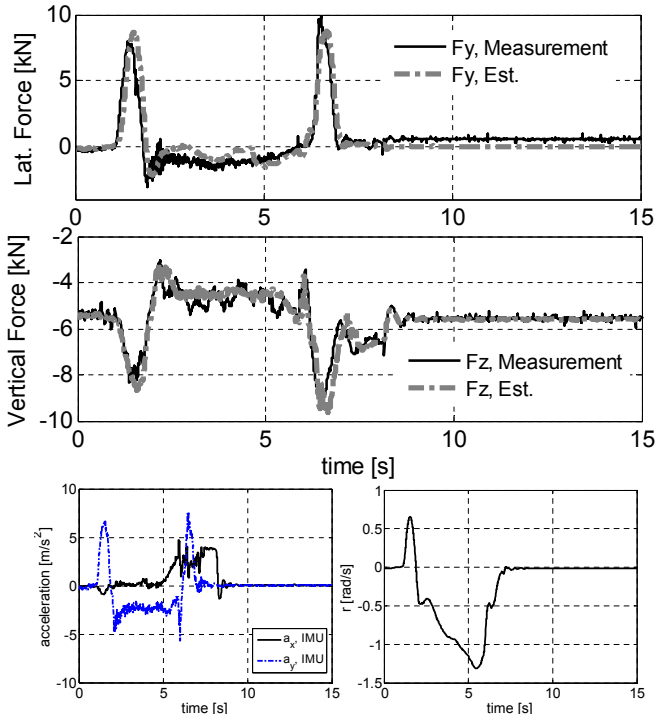

Figure 4.9: Lateral and vertical force estimation, LC for AWD on a dry surface.

This test has been done with four passengers in the car, but the nominal vehicle total and sprung masses from Table 3.1 is used for the force estimators; experimental results from Fig. 4.9 confirm that the designed force estimator (by tuning the process and measurement covariance matrices in the UKF approach) is robust to reasonable changes in the mass (up to four passengers). To check the outcomes of the lateral and vertical force estimators

in laterally excited maneuvers, a harsh steering on an icy road is done for the AWD test vehicle and the results of the front-left corner are illustrated for in Fig. 4.10. The maneuver ended up on a surface with packed snow which is highly slippery itself with $\mu \approx 0.3$. The vehicle longitudinal velocity is $6.1 \leq V_x \leq 7.7\,[\mathrm{m/s}]$ for this test.

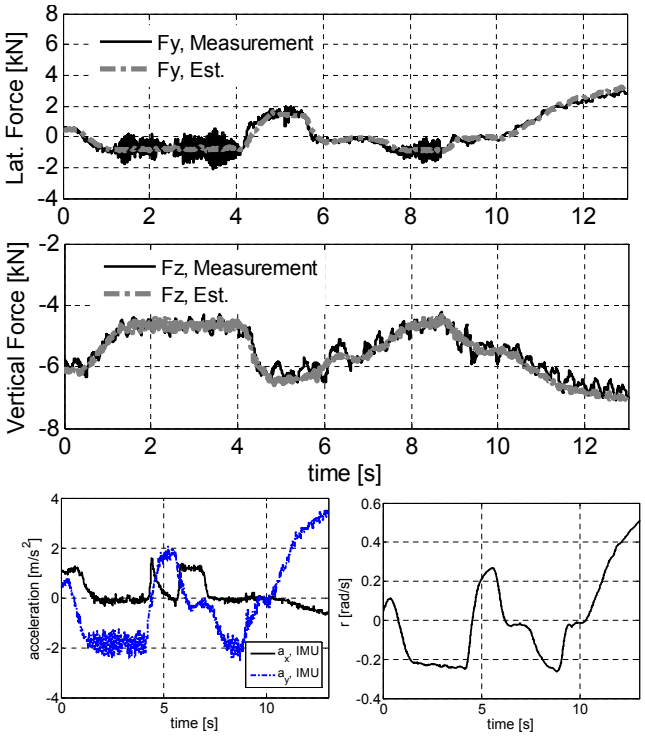

Figure 4.10: Lateral and vertical force estimates, steering on ice then packed snow.

Accuracy of the force estimators are evaluated in different maneuvers with the normalized root mean square of the error, *NRMS*, defined by $\bar{\varsigma} = \frac{\sqrt{\sum_{i=1}^{N_p}(\hat{p}_i - p_i)^2/N_p}}{p_m}$ where the measured and estimated signals are denoted by p and $\hat{p}$ respectively, N_p is the number of collected signal samples during a driving scenario (DLC, AiT, BiT, etc.), and $p_m = \max_{i=1\ldots N_p} |p_i|$ shows the maximum value of the measured signal. The normalized root mean square of the error of the longitudinal force estimators, $\bar{\varsigma}_{x1}, \bar{\varsigma}_{x2}$ (for UIO and UKF), lateral force estimator, $\bar{\varsigma}_y$, and vertical force estimator, $\bar{\varsigma}_z$, in different driving scenarios and on various road frictions are listed in Table 4.1; the maneuvers with four passengers in the car are marked by * in Table 4.1.

Table 4.1: Force Estimators' Error *NRMS*

Estimated	LC on wet/dry *		DLC on dry		BiT/Accel on snow	
forces	$\bar{\varsigma}_{x1}[\%]$	$\bar{\varsigma}_{x2}[\%]$	$\bar{\varsigma}_{x1}[\%]$	$\bar{\varsigma}_{x2}[\%]$	$\bar{\varsigma}_{x1}[\%]$	$\bar{\varsigma}_{x2}[\%]$
$F_{x_{fL}}$	4.05	3.85	5.76	6.10	4.77	5.01
$F_{x_{fR}}$	3.91	4.02	5.18	5.32	6.28	6.23
$F_{x_{rL}}$	4.17	4.53	5.24	4.97	6.04	6.41
$F_{x_{rR}}$	4.30	5.11	5.47	5.25	6.36	7.19
	$\bar{\varsigma}_{y}[\%]$	$p_m[\text{kN}]$	$\bar{\varsigma}_{y}[\%]$	$p_m[\text{kN}]$	$\bar{\varsigma}_{y}[\%]$	$p_m[\text{kN}]$
$F_{y_{fL}}$	6.03	6.38	2.94	10.13	5.56	3.18
$F_{y_{fR}}$	5.11	6.54	3.19	9.98	6.82	1.19
$F_{y_{rL}}$	5.24	4.08	3.86	9.20	6.17	2.74
$F_{y_{rR}}$	4.65	4.18	2.73	8.53	7.08	1.42
	$\bar{\varsigma}_{z}[\%]$	$p_m[\text{kN}]$	$\bar{\varsigma}_{z}[\%]$	$p_m[\text{kN}]$	$\bar{\varsigma}_{z}[\%]$	$p_m[\text{kN}]$
$F_{z_{fL}}$	3.34	12.77	2.06	12.90	3.88	9.10
$F_{z_{fR}}$	2.72	12.41	3.44	12.36	3.03	7.06
$F_{z_{rL}}$	2.15	10.02	1.91	10.75	3.54	7.19
$F_{z_{rR}}$	1.93	10.14	2.24	10.62	2.92	6.82

Table 4.1 shows that the *NRMS* of the estimated longitudinal forces by UIO is better than the UKF and it is less than 6.37% for the performed maneuvers on dry, wet, and snowy roads. Therefore, the UIO approach is selected as the longitudinal force estimator for the velocity estimation in Section 5.2 because of its superior performance even in the presence of uncertainties such as in road conditions, which may vary from icy to dry (i.e. $0.1 \leq \theta \leq 0.97$) in the tire model, effective radii with $\pm 5\%$ variation, and corrupted measurements of wheel speed and torque with variance $R_\omega = 0.18$ and $R_{T_t} = 32$ respectively.

Table 4.1 also substantiates that the *NRMS* of the estimated longitudinal forces is less than 7.2% for the performed maneuvers on dry, wet, and snowy roads. This normalized error is $\bar{\varsigma}_y \leq 6.9\%$ for the lateral forces and $\bar{\varsigma}_z \leq 3.9\%$ for the vertical forces respectively. These values confirm effectiveness of the algorithm for the corner-based force estimation on dry and slippery roads. Observed errors between the measured and estimated forces in

Table 4.1 for the force estimators may have several sources such as camber angle, which has not been modeled in the estimation algorithm. Moreover, inaccurate inertial parameters and uncertainties in the CG location contribute to such errors.

4.6 Summary

In this chapter, longitudinal, lateral, and vertical tire-free force estimators were developed using robust nonlinear and Kalman-based observers and common measurements without any limiting assumption on the lateral force distribution proportional to the vertical loads on a track.

The longitudinal force estimators uses total torques and wheel speeds at each corner. The UKF-based lateral force estimator employs vehicle lateral dynamics, acceleration measurements, steering, and the yaw rate. Vertical forces at each corner from are obtained by load transfer, vehicle angles and accelerations; vertical forces are employed for normalization of the longitudinal and lateral forces for the velocity estimators in the next Chapter. These estimators were experimentally tested on two vehicles in different driving scenarios and on roads with various friction conditions.

The holistic corner-based structure of the longitudinal/lateral force estimators advantageously suits requirements of the stability and traction control systems and can be utilized in such systems and with a cascaded structure for any model-based velocity estimators.

Chapter 5

Vehicle Velocity Estimation

Longitudinal and lateral velocities make major contributions to traction (wheel slip) control and stability (vehicle yaw rates, and side slip angles) control systems, respectively. They can be measured with GPS, but the poor accuracy of the mostly practiced conventional GPSs and the loss of reception in some areas are primary drawbacks that highlight the importance of the vehicle velocity estimation. This chapter presents a method for velocity estimation at each corner on various road friction conditions. This is entailed for more demanding advanced vehicle active safety systems and especially in full autonomous driving in harsh maneuvers.

A novel parameter-varying observer for the velocity estimation, robust to road friction and tire parameter changes, is introduced which treats acceleration measurement noises and the road condition as uncertainties. The combined kinematic and model-based algorithm for estimation of the velocities (sideslip angles and slip ratios) has a modular structure which can employ any force estimation module.

A lateral velocity estimator is developed in this chapter for conventional vehicles without wheel torque information by an integrated tire-kinematic scheme. This algorithm also utilizes adaptive weighted axle estimates and high slip angle detection to cope with high-slip conditions during large steering. Moreover, the newly introduced velocity estimator can be utilized in many road identification approaches [28, 33, 108, 109]. However, those references usually employ the slip ratio/angle measurement from accurate GPS data, that is not available for production vehicles. An approach for road classification using vehicle

lateral responses on different roads based on pure and combined-slip models is investigated in this chapter.

The suggested longitudinal and lateral state estimators are provided in sections 5.2 and 5.3. The stability, performance, and robustness of the linear parameter-varying estimators' error dynamics is also explored in these sections. Lateral state estimation for conventional vehicles is discussed in Section 5.3. Road classification based on the vehicle lateral response and vehicle speed is discussed in Section 5.4. Section 5.5 presents simulation and experimental results used to verify the approach on different road conditions, with varied tire type and inflation pressure, and in various maneuvers with high and low longitudinal/lateral excitations. Finally, summary is provided.

5.1 Introduction

As conferred in section 2.3, because of difficulties in dealing with time-varying tire parameters and unknown road conditions, conventional kinematic-based velocity estimators employ acceleration measurement and rely on GPS data intermittently. Linear, Kalman-based, or nonlinear observers are used in such kinematic methods [43, 44, 47] without using a tire model. Solving the longitudinal $\dot{V}_x = a_x + rV_y + \vartheta_x$ and lateral $\dot{V}_y = a_y - rV_x + \vartheta_y$ kinematics with removing bias and noises ϑ_x, ϑ_y by using GPS, the kinematic methods estimate the longitudinal and lateral velocities V_x, V_y. However, using an accurate GPS device and unavailability of reliable signals in many circumstances imposes extra costs and uncertainties for production vehicles. On the other hand, the performance of the velocity estimators based on tire forces is practically limited because of uncertain road friction and tire parameters, especially for saturation regions. Consequently, the kinematic approach is combined with the LuGre model's internal states at each corner in this section to tackle these issues.

The corner-based state estimation structure is illustrated in Fig. 5.1, in which the estimations from *Longitudinal Force Est* and *Lateral Force Est* modules are fed to the observer-based velocity estimators. Longitudinal, lateral, and vertical force estimators, discussed in Chapter 4, are developed using nonlinear and Kalman-based observers. In the newly proposed *Longitudinal Velocity Est* and *Lateral Velocity Est* modules, kinematic-

based approach is combined with the internal tire states considering road friction and measurement noises as uncertainties. The longitudinal and lateral velocity estimators use accelerations, yaw rate, steering angle, roll dynamics, estimated tire forces, and provide slip angle/ratio at each tire. Measured accelerations by IMU attached to the sprung mass are corrected with the vehicle's body pitch and roll angles from *Pitch/Roll Angle Est* to include only the kinematics of the motion. These corrected values are then used for the normal force and velocity estimators.

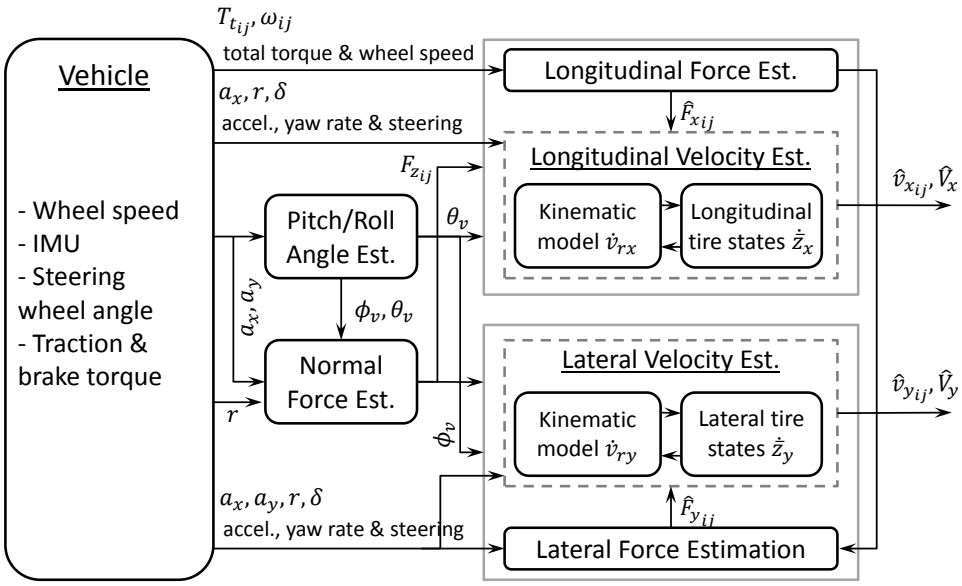

Figure 5.1: Corner-based state estimation structure

The proposed approach is experimentally validated on various road conditions using full-size test vehicles with different driveline configurations and control actuation.

5.2 Longitudinal Velocity Estimation

The average lumped LuGre model [18] is utilized in this study to estimate velocities because of its accuracy and the dynamics on its internal states. The internal state $\dot{\bar{z}}_q = v_{rq} - (\kappa_q R_e|\omega| + \frac{\sigma_{0q}|v_{rq}|}{\theta g(v_{rq})})\bar{z}_q$ for each direction $q \in \{x, y\}$ in the pure-slip model is utilized in

this section; the unknown road friction term $\frac{\sigma_{0q}|v_{rq}|}{\theta g(v_{rq})}\bar{z}_q$ and changes in the rolling radius are unknown, considered as uncertainty terms. The LuGre model's internal states (2.1a) can be written in the presence of uncertainty $\Omega_z(t)$ as follows at each corner (tire) for the longitudinal direction:

$$\dot{\bar{z}}_x = v_{rx} - \kappa_x R_e|\omega|\bar{z}_x + \Omega_{zx}. \tag{5.1}$$

Uncertainty Ω_{zx} is replaced with the road friction term $\frac{\sigma_{0x}|v_{rx}|}{\theta g(v_{rx})}\bar{z}_x$ and is bounded. Moreover, the derivative of the relative velocity is also corrupted due to the sensor noise and bias [110]:

$$\dot{v}_{rx} = R_e\dot{\omega} - \dot{v}_{xt} + \Omega_{ax}, \tag{5.2}$$

in which $\dot{\omega}$ is the wheel's rotational acceleration and $\dot{v}_{xt}$ represents the longitudinal acceleration in the tire coordinate system. $\dot{v}_{xt}$ is obtained from first, transformation of the corrected acceleration $\check{a}_x + rV_y$ from CG to corners where $\check{a}_x$ from (4.3) only contains the kinematic part, then, projection of the corner's acceleration into the tire coordinates. The term Ω_{ax} shows the deviation of the measured relative acceleration $R_e\dot{\omega} - \dot{v}_{xt}$ from $\dot{v}_{rx}$ because of the sensor noises. Establishing these equations allow the development of an observer to incorporate both tire deflections (5.1) and relative velocities (5.2) concurrently [91]. The general form of the system dynamics is given as follows:

$$\begin{aligned}\begin{bmatrix}\dot{\bar{z}}_x\\ \dot{v}_{rx}\end{bmatrix} &= \begin{bmatrix}-\kappa_x R_e\omega & 1\\ 0 & 0\end{bmatrix}\begin{bmatrix}\bar{z}_x\\ v_{rx}\end{bmatrix} + \begin{bmatrix}0\\1\end{bmatrix}(R_e\dot{\omega} - \dot{v}_{xt}) + \mathbf{\Omega}_x\\ &= A_x(\omega)\mathbf{x} + B_x u_x + \mathbf{\Omega}_x,\end{aligned} \tag{5.3}$$

in which $\mathbf{\Omega}_x = [\Omega_{zx} \quad \Omega_{ax}]^T$ and states are $\mathbf{x} = [\bar{z}_x \quad v_{rx}]^T$. Substituting $\dot{\bar{z}}_x$ from (5.1) into the normalized longitudinal force equation of the pure-slip LuGre model (2.1b), one can rewrite the output equation as:

$$\begin{aligned}\mu_x &= [(\sigma_{0x} - \sigma_{1x}\kappa_x R_e\omega) \quad (\sigma_{1x} + \sigma_{2x})]\mathbf{x} + \sigma_{1x}\Omega_{zx}\\ &= C_x(\omega)\mathbf{x} + \sigma_{1x}\Omega_{zx}.\end{aligned} \tag{5.4}$$

Thereby, the estimated output can be written as $\hat{\mu}_x = C_x(\omega)\hat{\mathbf{x}}$. Using the modified longitudinal kinematics (5.3) the following observer is proposed for the velocity estimation:

$$\dot{\hat{\mathbf{x}}} = A_x(\omega)\hat{\mathbf{x}} + B_x u_x + \mathbf{L}_x(\mu_x - \hat{\mu}_x), \tag{5.5}$$

where $\mathbf{L}_x = [L_{1x} \quad L_{2x}]^T$ is the observer gain matrix and μ_x represents the normalized longitudinal forces discussed in Chapter 4. Taking into account that the systems dynamic is time-varying with respect to the wheel speed, the suggested estimation method must be designed for the corresponding uncertain LPV system.

The bounded time-varying parameter is the wheel speed $\omega : \mathbb{R}_{\geq 0} \to \mathcal{S}_p$ where $\mathcal{S}_p$ is the set of vertices of the parameter interval $[\omega_l, \omega_u]$ and the parameter varying state transition matrix is $A_x(\omega) \in \mathbb{R}^{2\times 2}$. The error dynamics $\dot{\mathbf{e}}_x = \dot{\mathbf{x}} - \dot{\hat{\mathbf{x}}}$ from (5.3) and (5.5) yields:

$$\begin{aligned}\dot{\mathbf{e}}_x &= (A_x(\omega) - \mathbf{L}_x C_x)\mathbf{e}_x - \mathbf{L}_x \sigma_{1x} \Omega_{zx} + \mathbf{\Omega}_x \\ &= A_{e_x}(\omega)\mathbf{e}_x + \underbrace{\begin{bmatrix} 1 - L_{1x}\sigma_{1x} & 0 \\ -L_{2x}\sigma_{1x} & 1 \end{bmatrix}}_{B_{e_x}} \mathbf{\Omega}_x,\end{aligned} \tag{5.6}$$

Estimator's stability analysis

The objective of this subsection is to show that the error dynamics (5.6) is affinely quadratically stable over all possible trajectories of ω. The state matrix $A_{e_x}(\omega)$ is said to be affinely dependent on the parameter ω when known and fixed matrices A_{0x} and A_{1x} exist such that $A_{e_x}(\omega) = A_{0x} + \omega A_{1x}$. The error dynamic matrix for both lateral and longitudinal directions $q \in \{x, y\}$ is introduced as:

$$\begin{aligned}A_{e_q} &= \begin{bmatrix} -L_{1q}\sigma_{0q} & -L_{1q}p_{1q} \\ -L_{2q}\sigma_{0q} & -L_{2q}p_{1q} \end{bmatrix} + \omega \begin{bmatrix} \kappa_q R_e p_{2q} & 0 \\ \kappa_q R_e L_{2q}\sigma_{1q} & 0 \end{bmatrix} \\ &= A_{0q} + \omega A_{1q}\end{aligned} \tag{5.7}$$

where $p_{1q} = \sigma_{1q} + \sigma_{2q}$ and $p_{2q} = L_{1q}\sigma_{1q} - 1$. The bounded time-varying parameter and its time derivatives are in the sets $\omega_p \in [\omega_l, \omega_u]$ and $\dot{\omega}_p \in [\dot{\omega}_l, \dot{\omega}_u]$, respectively.

A linear system like (5.6) is affinely quadratically stable over all possible trajectories of the parameter vector $\omega(t)$ if $A_{e_x}(\omega_m)$ is stable (ω_m is the average value of ω over the parameter span) and there exists an affine positive definite Lyapunov function

$$V(e_x, \omega) = e_x^T P(\omega) e_x, \tag{5.8}$$

with $P(\omega) = P_0 + \omega P_1 > 0$ such that $dV(\omega, \dot{\omega})/dt < 0$ for all initial conditions x_0 and the additional multi-convexity constraint $A_{1x}^T P_1 + P_1 A_{1x} \geq 0$ holds [111]. The condition $\dot{V} < 0$ resembles $A_{e_x}^T(\omega_p)P(\omega_p) + P(\omega_p)A_{e_x}(\omega_p) + \frac{dP(\omega_p)}{dt} < 0$ that yields

$$A_{e_x}^T(\omega_p)P(\omega_p) + P(\omega_p)A_{e_x}(\omega_p) + P(\dot{\omega}_p) - P_0 < 0, \tag{5.9}$$

for all $(\omega, \dot{\omega}) \in \mathcal{S}_p \times \mathcal{S}_r$ where $\mathcal{S}_r$ is the set of corners of the rate in $[\dot{\omega}_l, \dot{\omega}_u]$. This is because $\frac{dP(\omega_p)}{dt} = P(\dot{\omega}_p) - P_0$ from $P(\omega_p) = P_0 + \omega_p P_1$. The affine quadratic stability condition implements the variation rate $\dot{\omega}(t)$, which makes it less conservative than the quadratic stability criteria. The error dynamics is affinely quadratically stable for the two sets of observer gains $L_{1x} \in [0.5, 0.9], L_{2x} \in [60, 210]$, obtained by several simulations and experimental tests on different road conditions and the vehicle parameters listed in Table 3.1. Stability of the system (5.6) will be guaranteed with the substitution of the operating regions $|\omega| \leq 180[rad/s]$ and $|\dot{\omega}| \leq 800[rad/s^2]$, which is practical for this case according to the sampling frequency $200[Hz]$ i.e. $T_s = 0.005[s]$ and measurement errors in the wheel speed. Given the vehicle parameters listed in Table 3.1, the tire rubber stiffness $\sigma_{0x} = 632.1[1/m]$, rubber damping $\sigma_{1x} = 0.76[s/m]$, relative viscous damping $\sigma_{2x} = 0.0016[s/m]$, load distribution factor $\kappa_x = 8.32$, observer gains $L_{1x} = 0.68, L_{2x} = 183.1$ and the affinely dependent form of (5.7), considering a polytope with bounds on $\dot{\omega}$ to solve (5.9) yields the following numeric values for the symmetric matrix $P(\omega)$:

$$P(\omega) = \begin{bmatrix} 1.2176 - 0.0011\omega & 115.35 - 0.2227\omega \\ 115.35 - 0.2227\omega & 80379.0 - 67.969\omega \end{bmatrix}. \tag{5.10}$$

Estimator's performance analysis

The objective is to find the observer gains such that the ratio of the estimation error to the disturbance energy is minimized considering the fact that the process disturbance Ω_{zx} and the measurement disturbance Ω_{ax} are bounded. Given a compact set $\omega \in [\omega_l, \omega_u]$ and a bounded rate of variation of $|\dot{\omega}| < \zeta_\omega$, for some $\zeta_\omega > 0$ the system (5.6) is robustly exponentially stable if there exist a continuously differentiable positive definite matrix $P(\omega)$

and a matrix $\chi(\omega)$ such that the following LMI holds:

$$\begin{bmatrix} \varphi(\omega) & P(\omega)+\chi(\omega)B_{e1} & C_e^T \\ * & -\gamma I & 0 \\ * & * & -\gamma I \end{bmatrix} < 0, \tag{5.11}$$

where the symmetric terms are denoted by $*$ and φ is:

$$\varphi(\omega) = [A_x^T(\omega) - C_x^T(\omega)\mathbf{L}_x^T]P(\omega) + P(\omega)[A_x(\omega) - \mathbf{L}_x C_x(\omega)] + \frac{\partial P}{\partial \omega}\dot{\omega}. \tag{5.12}$$

In order to isolate the observer gain effect, B_{e_x} can be written as $B_{e_x} = I_{2\times 2} + \mathbf{L}_x B_{e1}$, in which $B_{e1} = [\sigma_{1x} \quad 0]$. The induced $\mathcal{L}_2$ norm from the input disturbance to the output error is less than the performance level $\gamma > 0$. The LMI (5.11) is obtained by taking derivative of the Lyapunov function $V(e_x, \omega) = e_x^T P(\omega) e_x$, imposing the condition $\varphi(\omega) < 0$, and using the Bounded Real Lemma. Employing $\chi(\omega) = P(\omega)\mathbf{L}_x$, one can rewrite:

$$\varphi(\omega) = A_x^T P + P A_x - \chi C_x - C_x^T \chi^T + \frac{\partial P}{\partial \omega}\dot{\omega} \tag{5.13}$$

The LMI (5.11) guarantees that $\dot{V} + \mathbf{e}_x^T \mathbf{e}_x - \gamma^2 \mathbf{\Omega}_x^T \mathbf{\Omega}_x < 0$. The set of gains will be calculated by $\mathbf{L}_x = P(\omega)^{-1}\chi(\omega)$. The infinite dimensional parameter-varying LMI (5.11) with $\varphi(\omega)$ from (5.13) can explicitly be expressed in a finite dimensional problem with the parametric matrices and using appropriate basis functions. The positive definite matrix P and matrix φ are defined as $P(\omega) := \sum_{i=0}^{f} P_i \omega^i$ and $\varphi(\omega) := \sum_{i=0}^{f} \varphi_i \omega^i$ respectively and the set $\omega = [0 \quad 140]$ is gridded to $\mathcal{N}_{gr} = 140$ points. The time-varying observer gains L_1, L_2 form solved LMIs by YALMIP package [112] are depicted in Fig. 5.2-a for the longitudinal observer and the vehicle parameters provided in Table 3.1.

The condition for getting the $\mathcal{H}_\infty$ performance can be checked graphically by plotting $||H(j\omega)||$ for different values of the vehicle wheel speed. The corresponding frequency responses of the LPV system with time-varying observer gains are illustrated in Fig. 5.3 for different wheel speeds.

Figure 5.3 shows non-expansive characteristics of the error dynamics (5.6) (with worst-case gain $\gamma_{wc} < 1$) and demonstrates diminishing uncertainties with the allocated time-varying gains in all channels even for measurement noise rejection in the second channel of the observer at low frequencies ($\gamma_{wc} = 0.998$).

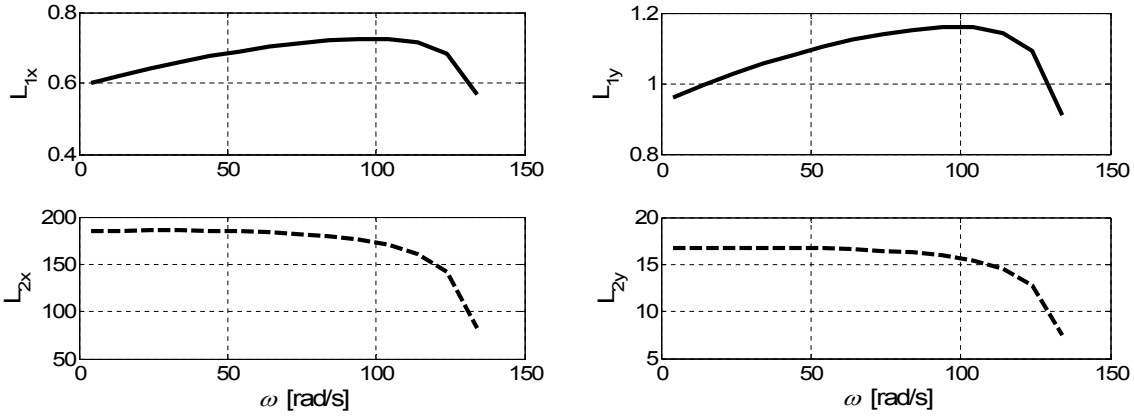

(a) longitudinal estimator (b) lateral estimator

Figure 5.2: Time-varying observer gains for velocity estimators.

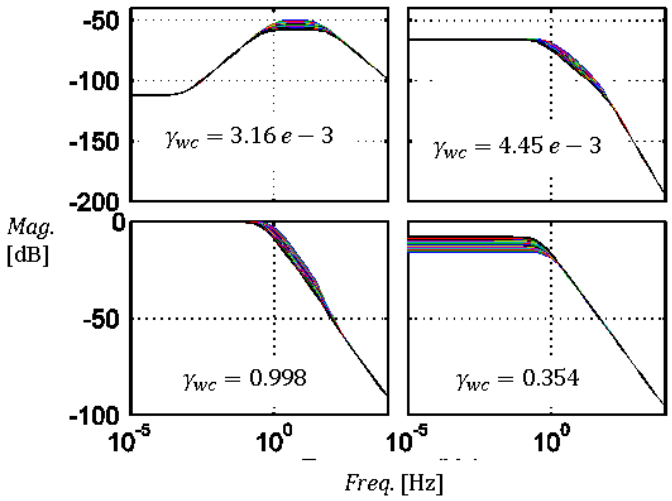

Figure 5.3: Response of the observer with time-varying gains.

The estimated relative longitudinal velocities $\hat{v}_{rx_{ij}}$ at each corner from (5.5) are used for the longitudinal velocity estimation at the tire coordinates as $\hat{v}_{xt_{ij}} = R_e\omega_{ij} - \hat{v}_{rx_{ij}}$. Afterward, each corner's longitudinal velocity in the vehicle coordinates $\hat{v}_{x_{ij}}$ yields:

$$\hat{v}_{x_{ij}} = \hat{v}_{xt_{ij}}\cos\delta - \hat{v}_{yt_{ij}}\sin\delta \tag{5.14}$$

in which δ is the steering angle at corners and the estimated lateral velocity at each corner's tire coordinates is denoted by $\hat{v}_{yt_{ij}}$. In order to increase the accuracy of the corners' velocity estimates, suspension compliance can be considered as investigated in [113]. The corner-based lateral velocity estimation will be described in the next subsection.

To tackle the high slip conditions and provide a smooth estimation with removing outliers, weighted estimated longitudinal velocities at each corner are used for the estimation of the vehicle speed, $\hat{V}_x$. Specifically, each axles' longitudinal velocities are defined by $\hat{v}_{x_f}$ and $\hat{v}_{x_r}$ that are the mean values between $\hat{v}_{x_{fL}}, \hat{v}_{x_{fR}}$ for the front axle and $\hat{v}_{x_{rL}}, \hat{v}_{x_{rR}}$ for the rear axle respectively. Then, the longitudinal velocity of the vehicle $\hat{V}_x$ at CG is achievable by adaptive weighted velocity mapping method, which is allocating adaptive weights $\mathcal{W}_x^f, \mathcal{W}_x^r$ to each axle as $\hat{V}_x = \mathcal{W}^f \hat{v}_{x_f} + \mathcal{W}^r \hat{v}_{x_r}$. Adaptive weights are defined with respect to the maximum slip ratio of each axle as functions:

$$\mathcal{W}_x^i = \mathcal{W}_{s_x} + \bar{\mathcal{W}}_x \tan^{-1}[\rho_{\mathrm{w}_x}(\lambda_{a_m} - \lambda_{\mathrm{w}_{th}})], \tag{5.15}$$

and $\mathcal{W}_x^{-i} = 1 - \mathcal{W}_x^i$ where $i \in \{f, r\}$ and $-i$ represents another axle i.e. $-i \in \{r, f\}$. The weight range coefficient is $\bar{\mathcal{W}}_x = (\bar{\mathcal{W}}_{u_x} - \bar{\mathcal{W}}_{l_x})/\pi$ where upper and lower bounds on the allocated weights are expressed by $\bar{\mathcal{W}}_{u_x}, \bar{\mathcal{W}}_{l_x}$. The slip ratio threshold at which the weight of each axle are the same is denoted by $\lambda_{\mathrm{w}_{th}}$. The maximum slip ratio of axles are used to allocate a smaller weight to an axle with higher slip ratio; it is achievable by

$$\lambda_{a_m} = \max\{\Sigma_i^x, \Sigma_{-i}^x\}, \tag{5.16}$$

where $\Sigma_i^x = |\lambda_{iL}| + |\lambda_{iR}|$ is defined for an axle and $\Sigma_{-i}^x = |\lambda_{-iL}| + |\lambda_{-iR}|$ is written for another axle. The shape of the axle's weight function can change with the parameters ρ_{w_x} and the static weight $\mathcal{W}_{s_x}$. Afterward, the calculated velocity at CG is remapped again to each corner to have slip ratios for the stability and traction control systems. The combined kinematics-tire approach for velocity estimation and the adaptively weighted track estimates are employed to develop a longitudinal velocity estimator in [114], which can be used for various driveline configurations independent from the wheel torques.

5.3 Lateral Velocity Estimation

The LuGre output equation for the lateral direction can be described as follows with states $\mathbf{x}_l = [\bar{z}_y \quad v_{ry}]^T$:

$$\begin{aligned}\mu_y &= [(\sigma_{0y} - \sigma_{1y}\kappa_y R_e\omega) \quad (\sigma_{1y} + \sigma_{2y})]\mathbf{x}_l + \sigma_{1y}\Omega_{zy} \\ &= C_y(\omega)\mathbf{x}_l + \sigma_{1y}\Omega_{zy}. \end{aligned} \tag{5.17}$$

Employing the lateral LuGre internal state from (2.1a) and the relative lateral acceleration $\dot{v}_{ry} = -\dot{v}_{yt} + \Omega_{ay}$ with the projected lateral acceleration $\dot{v}_{yt}$ in the tire coordinate system, the newly proposed lateral dynamics can be developed. $\dot{v}_{yt}$ is obtained from first, transformation of the corrected acceleration $\check{a}_y - rV_x$ from CG to corners where $\check{a}_y$ from (4.3) only includes the kinematic part, then, projection of the corner's acceleration into the tire coordinates. Therefore, (5.3) can be rewritten for the lateral direction as:

$$\dot{\mathbf{x}}_l = A_y(\omega)\mathbf{x}_l + B_y u_y + \mathbf{\Omega}_y. \tag{5.18}$$

using state and input matrices similar to the longitudinal case $A_y = [-\kappa_y R_e\omega \quad 1; 0 \quad 0], B_y = B_x$ and $u_y = -\dot{v}_{yt}$. Uncertainties in the lateral states are denoted by $\mathbf{\Omega}_y = [\Omega_{zy} \quad \Omega_{ay}]^T$. The state estimator can be expressed as follows for the lateral direction:

$$\dot{\hat{\mathbf{x}}}_l = A_y(\omega)\hat{\mathbf{x}}_l + B_y u_y + \mathbf{L}_y(\mu_y - \hat{\mu}_y), \tag{5.19}$$

in which $\mathbf{L}_y = [L_{1y} \quad L_{2y}]^T$. The error dynamics is then developed as:

$$\dot{\mathbf{e}}_y = A_{e_y}(\omega)\mathbf{e}_y + \underbrace{\begin{bmatrix} 1 - L_{1y}\sigma_{1y} & 0 \\ -L_{2y}\sigma_{1y} & 1 \end{bmatrix}}_{B_{e_y}} \mathbf{\Omega}_y, \tag{5.20}$$

where $A_{e_y} = (A_y - \mathbf{L}_y C_y)$. The error dynamics (5.20) for the proposed lateral velocity estimator represents a linear parameter-varying system and its stability can be investigated using the affine quadratic stability criteria discussed in the previous subsection.

Stability and performance of the Lateral estimator

The error dynamics (5.20) is affinely quadratically stable over all possible trajectories of ω. Analogous to the longitudinal case, the state matrix $A_{e_y}(\omega)$ can be written in the affine

form $A_{e_y}(\omega) = A_{0y} + \omega A_{ly}$ with the fixed matrices A_{0y} and A_{1y} from (5.7). $A_{e_y}(\omega_m)$ is stable and there exists an affine positive definite Lyapunov function $V(e_y, \omega) = e_y^T P(\omega) e_y$ with $P(\omega) = P_0 + \omega P_1 > 0$ such that $dV(\omega, \dot{\omega})/dt < 0$ for all initial conditions x_{l0} and the additional multi-convexity constraint $A_{1y}^T P_1 + P_1 A_{1y} \geq 0$ holds. The condition $\dot{V} < 0$ resembles

$$A_{e_y}^T(\omega_p) P(\omega_p) + P(\omega_p) A_{e_y}(\omega_p) + P(\dot{\omega}_p) - P_0 < 0 \tag{5.21}$$

The error dynamics is affinely quadratically stable for the two sets of observer gains $L_{1y} \in [0.8, 1.3], L_{2y} \in [6, 19]$, obtained by several road experiments. Given the tire specifications $\sigma_{0y} = 181.5[1/m]$, $\sigma_{1y} = 0.81[s/m]$, $\sigma_{2y} = 0.001[s/m]$, $\kappa_y = 12.84$, observer gains $L_{1y} = 1.11, L_{2y} = 16.7$, the vehicle parameters in Table 3.1, and the affinely dependent form of (5.7), solving (5.21) with considering a polytope and bounded wheel acceleration $|\dot{\omega}| \leq 800[rad/s^2]$ yields:

$$P(\omega) = \begin{bmatrix} 4.7718 - 0.0070\omega & 154.87 + 0.0038\omega \\ 154.87 + 0.0038\omega & 75627.0 - 0.0013\omega \end{bmatrix}. \tag{5.22}$$

Similar to the longitudinal case, parameter-varying observer gains are obtained using LMI (5.11) for the lateral direction and the outcomes are illustrated in Fig. 5.2-b.

Furthermore, a similarity transformation is used in the following proposition to investigate the boundedness of the estimation error of the longitudinal and lateral velocity estimators with error dynamics matrix A_{e_q} where $q \in \{x, y\}$.

Proposition 1. *Estimation errors in linear time varying error dynamics* (5.6) *and* (5.20) *are bounded.*

Proof. A similarity transformation in the form of $\bar{\mathbf{e}}_q(t) = T\mathbf{e}_q(t)$ is employed on the longitudinal/lateral estimation error states (5.6) and (5.20), which results in $\bar{A}_{e_q} = TA_{e_q}T^{-1}$ and $\bar{B}_{e_q} = TB_{e_q}$. Choosing $T = diag\{\gamma_e, 1\}$ with a design parameter $\gamma_e > 0$, leads to $\bar{A}_{e_q}$ whose stability margin, $\mathcal{SM}_q \triangleq \max_i \lambda_i(\bar{A}_{e_q})$, is close to the stability margin of its symmetric part. Moreover, due to the fact that $||T||$ and $||T^{-1}||$ are bounded, the transformation matrix T preserves the exponential stability and the rate of the convergence [115,116]. The Lyapunov candidate $\mathbf{V}(\bar{\mathbf{e}}_q(t)) = \frac{1}{2}\bar{\mathbf{e}}_q(t)^T\bar{\mathbf{e}}_q(t)$ is then introduced to investigate the stability

of the velocity estimators' error dynamics. The time derivative of the Lyapunov function along the state trajectories leads to

$$\begin{aligned}
\dot{\mathbf{V}} &= \frac{1}{2}\dot{\bar{\mathbf{e}}}_q(t)^T\bar{\mathbf{e}}_q(t) + \frac{1}{2}\bar{\mathbf{e}}_q^T(t)\dot{\bar{\mathbf{e}}}_q(t) \\
&= \bar{\mathbf{e}}_q^T(t)\underbrace{\left(\frac{1}{2}\left(\bar{A}_{e_q}^T + \bar{A}_{e_q}\right)\right)}_{\bar{A}_s}\bar{\mathbf{e}}_q(t) + \frac{1}{2}\left(\mathbf{\Omega}_q^T\bar{B}_{e_q}^T\bar{\mathbf{e}}_q(t) + \bar{\mathbf{e}}_q^T(t)\bar{B}_{e_q}\mathbf{\Omega}_q\right) \\
&\leq \lambda_{\max}(\bar{A}_s)||\bar{\mathbf{e}}_q(t)||^2 + \frac{1}{2}\left(\frac{1}{2\epsilon}\mathbf{\Omega}_q^T\bar{B}_{e_q}^T\bar{B}_{e_q}\mathbf{\Omega}_q + \frac{\epsilon}{2}||\bar{\mathbf{e}}_q(t)||^2\right) \\
&\leq \left(\lambda_{\max}(\bar{A}_s) + \frac{\epsilon}{4}\right)||\bar{\mathbf{e}}_q(t)||^2 + \lambda_{\max}(\bar{B}_{e_q}^T\bar{B}_{e_q})||\mathbf{\Omega}_q||^2 \\
&= 2\left(\lambda_{\max}(\bar{A}_s) + \frac{\epsilon}{4}\right)\mathbf{V} + \lambda_{\max}(\bar{B}_{e_q}^T\bar{B}_{e_q})||\mathbf{\Omega}_q||^2 \\
&\leq \eta_{e_1}\mathbf{V} + \eta_{e_2},
\end{aligned} \tag{5.23}$$

for some $\eta_{e_1} < 0$ and $\eta_{e_2} > 0$. Here $\mathbf{V}$ represents $\mathbf{V}(\bar{\mathbf{e}}_q(t))$ and ϵ is chosen such that $0 < \epsilon \ll |\lambda_{\max}(\bar{A}_s)|$ to have $\lambda_{\max}(\bar{A}_s) + \frac{\epsilon}{4} < 0$; thus, $\eta_{e_1} < 0$. The third line is due to the Young's inequality and the fourth row is due to the fact that $\bar{B}_{e_q}^T\bar{B}_{e_q}$ is a symmetric matrix. Introducing $\mathbf{U}(\bar{\mathbf{e}}_q(t)) = \mathbf{V}(\bar{\mathbf{e}}_q(t)) + \frac{\eta_{e_2}}{\eta_{e_1}}$, based on (5.23) and the Bellman-Gronwall lemma [117], we have $\mathbf{U}(\bar{\mathbf{e}}_q(t)) \leq e^{\eta_{e_1}t}\mathbf{U}(\bar{\mathbf{e}}_q(0))$, which yields:

$$0 \leq \mathbf{V}(\bar{\mathbf{e}}_q(t)) \leq e^{\eta_{e_1}t}\left(\mathbf{V}(\bar{\mathbf{e}}_q(0)) + \frac{\eta_{e_2}}{\eta_{e_1}}\right) - \frac{\eta_{e_2}}{\eta_{e_1}}, \tag{5.24}$$

which results in

$$0 \leq ||\bar{\mathbf{e}}_q(t)||^2 \leq e^{\eta_{e_1}t}\left(||\bar{\mathbf{e}}_q(0)||^2 + \frac{2\eta_{e_2}}{\eta_{e_1}}\right) - \frac{2\eta_{e_2}}{\eta_{e_1}}. \tag{5.25}$$

$\frac{\eta_{e_2}}{\eta_{e_1}} < 0$ proves the exponential stability of the nominal part of the error dynamics (5.6) and (5.20) (without term $\mathbf{\Omega}_q$) and the boundedness of the estimation error $\mathbf{e}_q(t)$. □

As mentioned in Proposition 1, the transformation matrix $\mathbf{T}$ yields a less conservative stability condition for the symmetric part of $\bar{\mathbf{A}}_{e_q}$ compared to the symmetric part of $\mathbf{A}_{e_q}$. Proposition 1 shows the boundedness of the estimation errors. However, in order to have tighter bounds, system $\mathcal{H}_\infty$ norms, defined as $\mathcal{H}_\infty \triangleq \sup_{\omega\in\mathbb{R}}||\mathbf{G}(j\omega)||_\infty$ is studied

for longitudinal/lateral error dynamics. This norm for both longitudinal and lateral velocity estimators is calculated and is $\mathcal{H}_\infty \leq 0.99$ for the wheel speed operating region $0 < \omega \leq 180$[rad/s] and observer gains $\mathbf{L}_x = [0.7 \quad 184]^T, \mathbf{L}_y = [1.1 \quad 16.8]^T$. It should be mentioned that the $\mathcal{H}_\infty$ norm is a conservative system norm and the calculations reveal that even such conservative norms of the error dynamics are non-expansive ($\mathcal{H}_\infty \leq 1$) for the proposed observers.

The sensitivity of the error dynamics stability margin $\mathcal{SM}_q$ to model parameter uncertainties is also investigated in the following for the same set of observer gains. Figs. 5.4, 5.5, and 5.6 show deviation of the stability margins and $\mathcal{H}_\infty$ norms of the error dynamics (5.6) and (5.20) from their nominal values due to model parameter deviation of up to $\pm 20\%$.

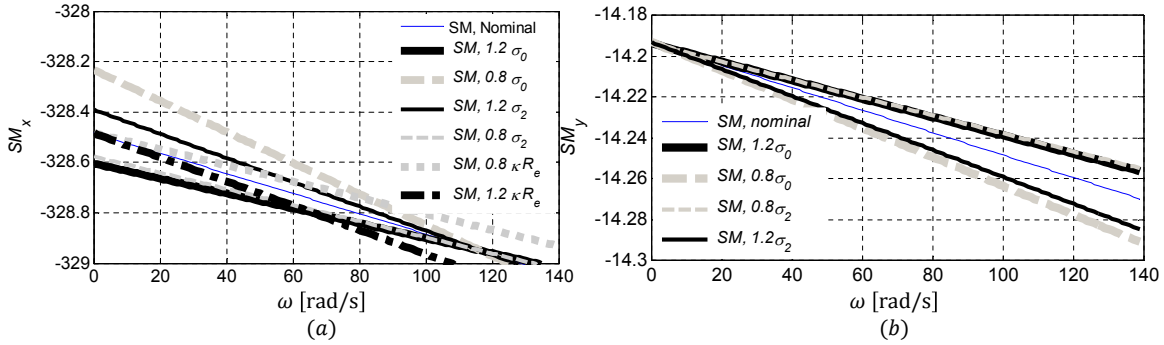

Figure 5.4: Sensitivity of $\mathcal{SM}$ of the Long. and Lat. error dynamics to model parameters.

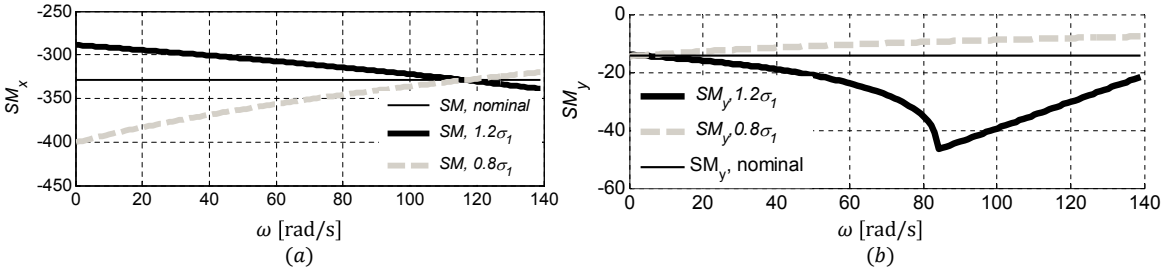

Figure 5.5: Sensitivity of $\mathcal{SM}$ of the longitudinal/lateral error dynamics to σ_{1q}.

These figures confirm that the performance of the developed observers is not very sensitive to the tire parameter variations.

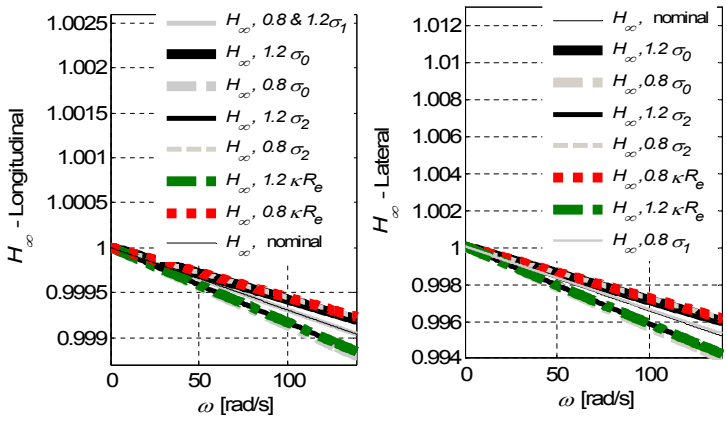

Figure 5.6: Sensitivity of $\mathcal{H}_\infty$ of the Long. and Lat. error dynamics to model parameters.

Analogous to the longitudinal case, each corner's lateral velocity $\hat{v}_{y_{ij}}$ in the body-fixed vehicle coordinates is achievable from:

$$\hat{v}_{y_{ij}} = \hat{v}_{xt_{ij}} \sin\delta + \hat{v}_{yt_{ij}} \cos\delta, \tag{5.26}$$

where $\hat{v}_{yt_{ij}}$ and $\hat{v}_{xt_{ij}}$ are the estimated lateral and longitudinal velocities at the tire coordinates. The lateral velocity in the tire coordinates is $\hat{v}_{yt_{ij}} = -\hat{v}_{ry_{ij}}$ and the relative velocity $\hat{v}_{ry_{ij}}$ is obtained from (5.19) at each corner.

5.3.1 Lateral state estimation for conventional cars

A new algorithm is developed and experimentally tested in this section for the lateral velocity estimation without wheel torques information. This algorithm implements common sensors (IMU, wheel speed, and steering) and addresses uncertainties due to large steering in high traction (or brake) with adaptive covariance matrices and variable weighted track estimates. Therefore, it can be employed for conventional cars and will have a noticeable impact on stability control and autonomous systems.

The effect of longitudinal forces in the planar kinetics (4.2) and (4.4) can be ignored for lateral forces used for lateral velocity estimation in conventional vehicles. Thereby, planar equations become $m\check{a}_x = -F_{y_f}\sin\delta + \mathbf{w}_{f_x}$, $m\check{a}_y = F_{y_f}\cos\delta + F_{y_r} + \mathbf{w}_{f_y}$, and $I_z\dot{r} = F_{y_f}\cos\delta d_f - \bar{F}_{y_f}\sin\delta\frac{T_{r_f}}{2} - F_{y_r}d_r + \mathbf{w}_r$. Uncertainties in the new dynamics can

be handled by modified covariance matrices for the lateral force estimation and modified observer gains of the lateral velocity estimator. An unscented Kalman filter is employed on a new system dynamics to estimate lateral velocities and internal tire states.

Employing internal tire states (2.1a) in the lateral direction, $\bar{z}_y$, and the lateral relative velocity $\dot{v}_{ry} = -\dot{v}_{yt} + \Omega_{ay}$ a Kalman-based observer is developed. The general form of the estimator at each corner ij, which can be addressed by the KF, with $\omega > 0$ is given as follows in which the states are $\mathbf{x}_n = [\bar{z}_y \quad v_{ry} \quad \dot{\bar{z}}_y]^T$ and $\mathbf{\Omega}_n = [\Omega_{zy} \quad \Omega_{ay} \quad \Omega_{\dot{z}y}]^T$:

$$\begin{aligned}
\dot{\mathbf{x}}_n &= A_n(\omega)\mathbf{x}_n + B_n u_y + \mathbf{\Omega}_n \\
&= M^{-1}\begin{bmatrix} -\kappa_y R_e\omega & 1 & 0 \\ 0 & 0 & 0 \\ -\kappa_y R_e\dot{\omega} & 0 & -\kappa_y R_e\omega \end{bmatrix}\begin{bmatrix} \bar{z}_y \\ v_{ry} \\ \dot{\bar{z}}_y \end{bmatrix} + M^{-1}\begin{bmatrix} 0 \\ 1 \\ 0 \end{bmatrix}(-\dot{v}_{yt}) + \mathbf{\Omega}_n, \\
\mathbf{y}_n &= C_n\mathbf{x}_n + \Gamma_n = \sigma_{0y}\bar{z}_y + \sigma_{2y}v_{ry} + \sigma_{1y}\dot{\bar{z}}_y + \Gamma_n,
\end{aligned} \tag{5.27}$$

and $M = [1 \quad 0 \quad 0; 0 \quad 1 \quad 0; 0 \quad -1 \quad 1]$. Process and measurement noises are denoted by $\mathbf{\Omega}_n, \Gamma_n$ respectively. The linear time-varying system (5.27) uses a reduced number of tire parameters: normal force distribution factor κ_y, rubber stiffness σ_{0y}, rubber damping σ_{1y}, and relative viscous damping σ_{2y}. These tire parameters are not related to the road condition and friction parameters. The bounded error covariance and stability of linear time-varying Kalman estimators for both known zero and nonzero initial error covariance were explored in [118, 119]. Observability is a sufficient condition for implementation of an optimal variance filter (such as a Kalman estimator). The discretized from of system (5.27) is:

$$\begin{aligned}
\mathbf{x}_{n_{k+1}} &= \bar{A}_{n_k}\mathbf{x}_{n_k} + \bar{B}_{n_k}u_{y_k} + \mathbf{\Omega}_{n_k}, \\
\mathbf{y}_k &= \bar{C}_{n_k}\mathbf{x}_{n_k} + \Gamma_{n_k},
\end{aligned} \tag{5.28}$$

in which the discretized system matrices $\bar{A}_n, \bar{B}_n, \bar{C}_n$ are obtained by step-invariance method and noise covariance matrices are denoted by $Q_{n_k} = \mathbb{E}[\mathbf{\Omega}_{n_k}, \mathbf{\Omega}_{n_k}{}^T]$ and $R_{n_k} = \mathbb{E}[\Gamma_{n_k}, \Gamma_{n_k}{}^T]$. Process and measurement noises are assumed to be uncorrelated and have zero mean.

Stability of the estimator

Stability of the error dynamics of the Kalman-based observer on system (5.27) is studied in this section with known and uncertain initial conditions. The detectability and stabilizability definitions in (A1) and (A2) are required for the stability analysis of the suggested discrete-time estimators. Uniform detectability leads to bounded error covariance. In addition, stabilizability of the paired state transition matrix and process noise results in exponential stability of the estimator, as proved in [120,121]. The stochastic observability, stability and convergence of the state mean, and bounds on error covariance of the Kalman estimator for linear time-varying (LTV) systems, such as that in (4.18), were studied in [120,122]. These studies were focused on systems with deterministic parameters and known initial state vectors and done in terms of uniform complete observability and controllability grammians. On the other hand, the bounded error covariance and stability of the Kalman estimator for systems with completely uncertain initial covariance/states is investigated in [123]. Uniform detectability and stabilizability conditions are investigated in this section to check the stability and error covariance boundedness of the proposed velocity estimator for two cases: **a**) known zero/nonzero initial states **b**) complete uncertainty of the initial-state statistics.

Proposition 2. *There exists a state estimator such as Kalman having bounded error covariance for time-variant system* (5.28) *with deterministic time-varying parameters and known initial state/covariance.*

Proof. For the system $\mathbf{x}_{n_{k+1}} = \bar{A}_{n_k}\mathbf{x}_{n_k} + \mathbf{\Omega}_{n_k}$, $\mathbf{y}_k = \bar{C}_{n_k}\mathbf{x}_{n_k} + \Gamma_{n_k}$ with uniform detectability of $[\bar{A}_{n_k}, \bar{C}_{n_k}]$, the known initial state/covariance, and the process and measurement noise covariances Q_{n_k}, R_{n_k}, there exists a state estimator such as the Kalman having bounded error covariance [120]. Furthermore, stabilizability of the pair $[\bar{A}_{n_k}, G_k]$ leads to exponential stability of the KF, where G_k is an appropriate matrix obtained by $Q_{n_k} = G_k G_k^T$. Proof is provided in [120]. Therefore, the detectability condition (A1) should be examined for the proposed velocity estimator (5.27). This is experimentally checked for the deterministic time-varying wheel speed of the discrete-time system's matrix $\bar{A}_{n_k}$. The rank of $\mathbb{V}(0, N)$ on several road experiments is 3. It confirms that the suggested estimator has full rank on the observability grammian (A1) for all performed maneuvers, showing the observability of the system for known initial covariances. The stabilizability condition is also required

since states should be affected by the noise such that the optimal Kalman estimator is forced to utilize measurements. This condition is also satisfied and the grammian (A2) has full rank.

Additionally, since the system matrix $A_n(\omega)$ in (5.27) is physically bounded (because of the wheel speed and its derivative characteristics), the conventional observability test (4.16) for time-variant systems is performed here and it is confirmed by holding the full rank condition $rank(\mathcal{O}_3) = 3$ at each fixed time span for operating regions of the wheel speed and its time derivatives. Thus, the suggested parameter-varying lateral state estimator (5.27) is observable. □

In the case of complete uncertainty on the initial state/covariance, the estimated covariance matrices can be unbounded even if the LTV system satisfies the observability criteria (A1). The bounded error covariance and stability of the Kalman filter for the proposed lateral velocity estimator for conventional vehicles applications with completely uncertain initial state/covariance is investigated here in the following.

Proposition 3. *The corner's lateral states $\bar{z}_y, v_{ry}$ of the time-varying system (5.27) can be recovered using measurements $\mu_{y_{ij}}$ and a Kalman estimator with stochastic initial covariance/states.*

Proof. By definition, the system (5.28) is stochastically observable if there exists a finite time t_f, such that the state covariance matrix P_k is bounded [123]:

$$\lambda_{max}(P_k) < \lambda_b, \ t_k \geq t_f, \tag{5.29}$$

where $\lambda_{max}(P_k)$ shows the largest singular value of the matrix P_k and λ_b is a predefined scalar bound. Assuming initial state covariance matrix $P_{0|-1} = \psi I, \psi \in \mathbb{R}, \psi > 0$, one can rewrite the time-varying Riccati equation (4.19) as [123]:

$$P_{k+1|k} = \psi \mathcal{M}_{k+1} + \mathcal{N}_{k+1} + \mathcal{S}_{k+1}, \tag{5.30}$$

where $\mathcal{N}_{k+1} = \mathcal{N}_{k+1}(\mathcal{M}_k, \mathcal{N}_k, \phi_k, \bar{C}_{n_k}, Q_{n_k}, R_{n_k})$, $\mathcal{S}_{k+1} = \mathcal{S}_{k+1}(\psi, \mathcal{S}_k, \mathcal{N}_k, \phi_k, \mathcal{M}_k, \bar{C}_{n_k}, Q_{n_k}, R_{n_k})$, and $\mathcal{M}_{k+1} \triangleq \phi_{k,0} X_{0,k} X_{0,k}^T \phi_{k,0}^T$. The procedure for obtaining $X_{0,k}$ is provided in the Appendix and $\phi_{i,j} = \phi_{i,i-1}\phi_{i-1,j}$ are the state transition matrices for $i \geq j$ with $\phi_{i+1,i} = \bar{A}_{n_i}$. In summary, the following *Lemma* presents two tests for observability of the velocity estimator with stochastic initial conditions.

Lemma 1. *[123] A Kalman estimator on the system (5.28) with an error covariance matrix $P_{k+1|k}$ and stochastic initial state $P_{0|-1} = \psi I, \psi \in \mathbb{R}^+$ is stochastically observable if the condition $\lambda_{max}(\mathcal{M}_f) = 0$ (test 1) holds for a finite time t_f and $\lambda_{max}(\mathcal{N}_{k+1}) < \lambda_b$ for $t_k \geq t_f$ (test 2) with a predefined bound λ_b, where $\mathcal{M}_{k+1}$ is obtained from the modified Riccati equation (5.30) and the procedure provided in (A6), (A7) in the Appendix. Employing the condition $\lambda_{max}(\mathcal{M}_f) = 0$ for a finite time $t_f < \infty$, the modified Riccati equation (5.30) changes to $P_{k+1|k} = \mathcal{N}_{k+1} + \mathcal{S}_{k+1}$ which leads to a simplified form of $\mathcal{N}_{k+1}$ as in:*

$$\mathcal{N}_{k+1} = \bar{A}_{n_k}\mathcal{N}_k\bar{A}_{n_k}^T + Q_{n_k} - \bar{A}_{n_k}\mathcal{N}_k\bar{C}_{n_k}^T\Xi_k^{-1}\Xi_k^{-T}\bar{C}_{n_k}\mathcal{N}_k\bar{A}_{n_k}^T, \tag{5.31}$$

where Ξ_k is expressed in (A7).

Whenever the two criteria on $\mathcal{M}_f, \mathcal{N}_{k+1}$ in Lemma 1 (so called *test1* and *test2*) are met, employed the Kalman observer is stable even if the scalar ψ has infinite values. These two tests and road experiments have been performed on the proposed observer with $Q_n = 2.9e-3$ and $R_n = 7.5e-4$ and results are depicted as follows. Figure 5.7 exhibits $\lambda_{max}(\mathcal{M}_f)$, where $\mathcal{M}_f$ is obtained from (5.30) and the procedure provided in the Appendix. Different experiments such as DLC, brake-in-turn (BiT), sharp turn, and steering on dry and slippery (snow/ice) roads have been performed and results are illustrated in Fig. 5.7.

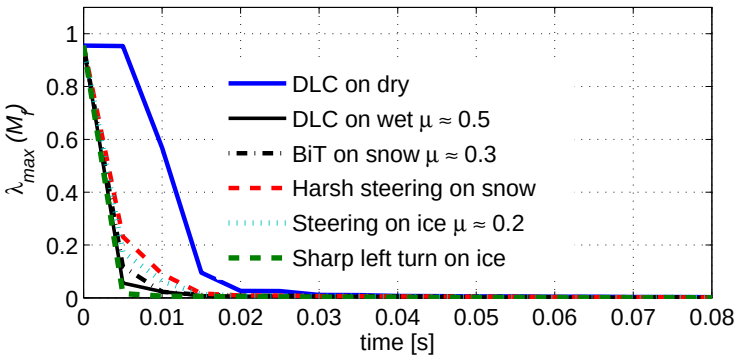

Figure 5.7: *Test1* for various road tests, experimental results

From the plots in Fig. 5.7, it is apparent that the largest singular value of $\mathcal{M}_f$ converges to zero after $t_f = 0.03$ sec. for different experiments. The values of $\lambda_{max}(\mathcal{N}_{k+1})$ with $\mathcal{N}_{k+1}$ from (5.31) are plotted in Fig. 5.8.

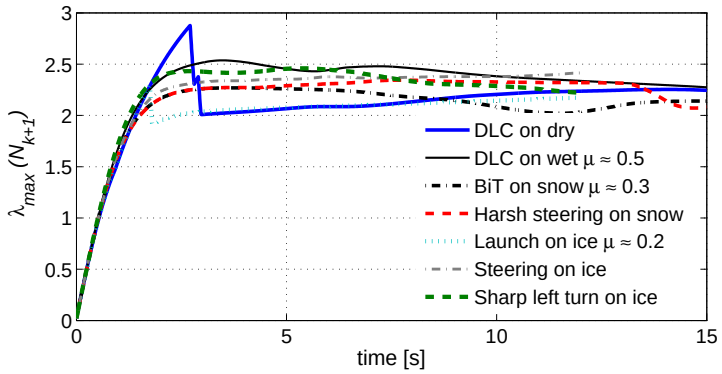

Figure 5.8: *Test2* for different driving scenarios and roads, experimental results

The results on different road conditions and pure/combined slip maneuvers, as shown in Fig. 5.8, indicate that the maximum singular value of $\mathcal{N}_{k+1}$ remains bounded. Thus, the both criteria (*test1* and *test2*) are met and the discretized form of system (5.27) with a KF estimator is stochastically observable. □

Consequently, the presented lateral estimator is stable, and errors of the state mean have bounded variance for both known and stochastic initial covariance.

A high-slip detection algorithm is used to deal with uncertainties associated with ignoring longitudinal forces effect and noises due to high steering and large slip angle conditions. Noise covariance matrices change appropriately upon detection of a high steering or high-slip cases to incorporate changing in the level of reliance on the vehicle kinematics (process) and lateral forces (measurement). Covariance matrices Q_n, R_n change adaptively to avoid errors (caused by nonlinearities/uncertainties) during harsh maneuvers on slippery surfaces.

This algorithm needs a slip angle threshold α_{th} after which the process and measurement covariance matrices change to $Q_n = 3.05e^{-4}$ and $R_n = 2.7e^{-1}$ respectively. Sudden changes in the slip angle (vehicles response) will not be detected in case of large constant high-slip threshold. This leads to more required time for the estimated slip angle to satisfy the threshold (i.e. it requires larger excitations). On the other hand, small constant threshold results in unnecessary detection of the large slip cases. Thus, in the developed high-slip detection module, the threshold changes between the predefined upper and lower bounds

α_u, α_l according to the driving conditions as:

$$\alpha_{th} = \alpha_u - \frac{1}{\varphi_e \sqrt{2\pi}} e^{-\frac{\beta_e \sigma_e}{2\varphi_e^2}}, \tag{5.32}$$

where $\varphi_e = \frac{1}{\sqrt{2\pi}}(\alpha_u - \alpha_l)$ and σ_e represents variance of the vehicle's acceleration a_k over a moving window with size N_a i.e. $\sigma_e = var\{||a_k||_2 : m - N_a \leq k \leq m\}, \forall m \in \mathbb{N}, m \geq N_a$, in which $||a_k||_2 = \sqrt{a_{x_k}^2 + a_{y_k}^2}$ and a_{x_k}, a_{y_k} are measured longitudinal and lateral accelerations. The rate of transition between the predefined upper and lower thresholds α_u, α_l is denoted by β_e. Thus, for $|\alpha| \geq \alpha_{th}$ the covariance matrices Q_n, R_n change to the new values. Finally, the covariance matrices change when each of the slip-based or steering-based criteria at each corner ij are met i.e. $\{|\alpha| \geq \alpha_{th} \vee |\delta| \geq \delta_{th}\}$. This leads to the prompt detection and consequently proper covariance matrix allocation.

In addition to the variable covariance matrices for large steering and high slip conditions, a weighted estimated axle's scheme is incorporated. This is to deal with errors caused by ignoring the effect of longitudinal forces in the planar kinetic model for conventional vehicle's state estimation. The lateral velocities at each corner $\hat{v}_{y_{ij}}$ are utilized for definition of the front and rear axle's lateral velocities $\hat{v}_{y_f}, \hat{v}_{y_r}$ respectively. Each axle's lateral velocities are obtained by $\hat{v}_{y_f} = -rd_f + (\hat{v}_{y_{fL}} + \hat{v}_{y_{fR}})/2$ for the front axle and $\hat{v}_{y_r} = rd_r + (\hat{v}_{y_{rL}} + \hat{v}_{y_{rR}})/2$ for the rear axle. Similar to the longitudinal case, using weighted estimated axles' lateral velocities, the vehicle lateral velocity $\hat{V}_y$ at the CG is expressed as follows:

$$\hat{V}_y = \mathcal{W}_y^f \hat{v}_{y_f} + \mathcal{W}_y^r \hat{v}_{y_r}, \tag{5.33}$$

where $\mathcal{W}_y^f$ and $\mathcal{W}_y^r$ are adaptive weights for each axle and are defined similar to the longitudinal case (5.15), but with respect to the maximum slip angle at each axle as in

$$\mathcal{W}_y^i = \mathcal{W}_{s_y} + \bar{\mathcal{W}}_y \tan^{-1}[\rho_{\mathrm{w}_y}(\alpha_{a_m} - \alpha_{\mathrm{w}_{th}})]. \tag{5.34}$$

with the slip angles threshold $\alpha_{\mathrm{w}_{th}}$. The weight range coefficient for the lateral direction is denoted by $\bar{\mathcal{W}}_y = (\bar{\mathcal{W}}_{u_y} - \bar{\mathcal{W}}_{l_y})/\pi$ with the upper and lower bounds $\bar{\mathcal{W}}_{u_y}, \bar{\mathcal{W}}_{l_y}$. Parameters ρ_{w_y} and $\mathcal{W}_{s_y}$ are introduced to change the shape of the lateral axle's weight function. To address the high slip angle scenarios and provide smooth estimation, the maximum slip angle of axles $\alpha_{a_m} = \max\{\Sigma_i^y, \Sigma_{-i}^y\}$ are utilized to allocate a smaller weight to an axle with higher slip angle. Each axle's slip angle is defined by

$$\Sigma_i^y = |\alpha_{iL}| + |\alpha_{iR}|, \quad \Sigma_{-i}^y = |\alpha_{-iL}| + |\alpha_{-iR}|. \tag{5.35}$$

An opinion dynamic-based distributed estimation [124], which uses level of reliability to each axles based on the slip ratio/angle, can be used instead of the weighted scheme described here. Provided that the current generalized estimation structure can be used for other vehicles with changing the vehicle parameters, the established framework will be evaluated in conventional cars. These estimators has been experimentally tested with aggressive maneuvers such as increasing the longitudinal speed during cornering, acceleration-in-turn, harsh steering, and launch on high and low-friction surfaces. Simulation and experimental results in Section 5.5 confirm the validity of the algorithms on different roads and with various driveline and actuator configurations.

Remark: Reliability analysis of the state estimators is performed by implementing the proposed weighted axle scheme, mapping the estimated corner velocities to the Vehicle's CG to define $\bar{u} := \hat{V}_x, \bar{v} := \hat{V}_y$, and combining the vehicle planar kinematic equations $a_x = \dot{\bar{u}} - r\bar{v}$ and $a_y = \dot{\bar{v}} + r\bar{u}$ as:

$$\begin{bmatrix} \hat{a}_x \\ \hat{a}_y \end{bmatrix} = \begin{bmatrix} 0 & -r \\ r & 0 \end{bmatrix} \begin{bmatrix} \bar{u} \\ \bar{v} \end{bmatrix} + \begin{bmatrix} \dot{\bar{u}} \\ \dot{\bar{v}} \end{bmatrix} \tag{5.36}$$

in which the estimated longitudinal and lateral velocities are correlated to check the reliability. The estimated accelerations, $\hat{a}_x, \hat{a}_y$, from (5.36) are compared by the measured ones to generate the residuals $\tilde{r}_x = |a_x - \hat{a}_x|, \tilde{r}_y = |a_y - \hat{a}_y|$ within a variable time window, which is adaptive based on the vehicle excitation level. A persistence criteria is also used to check repeated large residuals, i.e., $\tilde{r}_x \geq \tilde{r}_{x_{th}}, \tilde{r}_y \geq \tilde{r}_{y_{th}}$ within a certain time window. The reliability measure in each longitudinal and lateral direction is provided based on the value of the residuals.

Since the estimated acceleration produced by the derivatives of the longitudinal and lateral velocities are compared with the measured accelerations, the correlated kinematics (5.36) can be used to detect the drift-type failures/discrepancies (due to differences in slopes), thus to measure the reliability of the estimators. Although the values of velocities, $\bar{u}, \bar{v}$ appear in (5.36) and the approach is expected to provide the reliability of the estimates (not their derivatives), road experiments confirm that only the large bias in the order of derivatives of the velocities can result in high acceleration residuals. This is due to uncertainties in the model and the fact that the states and their derivatives in the correlated characteristics (5.36) may cancel out each other, that leads to inaccurate reliability measure

(or false failure detection). Therefore, failures and deviated estimates, which has bias (specially minor bias), can not be detected by this approach; the author is working on a new failure detection and reliability measure to address the bias-type deviations using additional measurements or dynamics.

5.4 Road Classification based on Lateral Dynamics

In this section the pure and combined-slip LuGre model are incorporated into the vehicle lateral dynamics (4.2), (4.4) and formulae are derived for the linear part of the curves and the saturation/nonlinear regions to check the vehicle response for road classification.

Lateral dynamics with the pure-slip model

Assuming steady state LuGre lateral model ($\dot{\bar{z}}_y = 0$), substituting $\bar{z}_y$ from (2.1a) into the normalized force (2.1b), and defining new variables $\rho = \theta g(v_{ry})$ and $\gamma = \kappa R_e \omega / \sigma_{0y}$, one can write the normalized lateral force of the pure-slip model as follows with the longitudinal speed in tire coordinates v_{xt} and slip angle α at each tire ij:

$$\mu_y = \left(\frac{\rho}{v_{xt}|\alpha| + \gamma\rho} + \sigma_{2y} \right) v_{xt}\alpha. \tag{5.37}$$

To be able to write the state-space form of the lateral dynamics based on the LuGre model, we need to analyze the effect of the slip angle as discussed in the following sections. For the case where $|\alpha| \ll \gamma\rho/v_{xt}$, the normalized lateral force (5.37) will be $\mu_{y_{lin}} = \theta \left(\frac{1}{\gamma} + \sigma_{2y} \right) v_{xt}\alpha$ where θ is employed with direct multiplication as an implication of the effect of road conditions. It helps in making the suggested pure-slip formulation compatible with the real tire model since the slope of the linear region of the force-slip curve is a function of the road condition as studied in the slip-slope method [28, 125] for road identification. Normalized lateral forces of the pure-slip LuGre model and the linear part (that resembles $|\alpha| \ll \gamma\rho/v_{xt}$) are depicted in Fig. 5.9 for various road conditions.

To consider the nonlinear part, disregarding the $|\alpha| \ll \gamma\rho/v_{xt}$ condition, one can rewrite

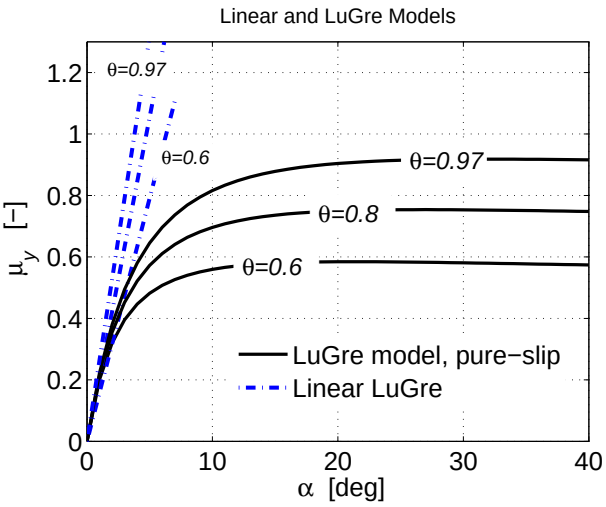

Figure 5.9: Pure-slip LuGre lateral tire model

the normalized lateral force (5.37) at each corner

$$\mu_y = kv_{xt}\alpha - \frac{1}{\gamma\left(1+\frac{\gamma\rho}{v_{xt}|\alpha|}\right)}v_{xt}\alpha, \tag{5.38}$$

where $k = \theta\left(\frac{1}{\gamma}+\sigma_2\right)$, v_{xt} is the longitudinal speed in the tire coordinates that is obtained by vehicle speed, and α is the slip angle at each corner. The term $kv_{xt}\alpha$ represents the linear part, and the second term shows nonlinear behavior of the lateral force with respect to the slip angle. Different stability criteria for the derived lateral dynamics are explored, compared with that of the bicycle model, and speed limit criteria are suggested for the pure and combined-slip cases in [126].

Combined-slip model for the lateral dynamics

The studies in [126] show that the steady-state model provides reasonable accuracy for several lateral tests. This makes it a sound choice for implementation in the derivation of the lateral dynamics based on combined-slip friction model for the road classification with a lateral response checking scheme. Subsequently, the tire-vehicle lateral dynamics with the steady-state combined-slip LuGre model is developed in this section. A practical,

closed form lateral vehicle-tire model that includes combined friction characteristics and consideration of slip ratio on each wheel is also presented as a remark. This is an advantage of the current formulation over conventional lateral vehicle-tire approaches that assume pure-slip and work with tracks' (axles') forces instead of tire forces at each corner.

A general vehicle model, shown in Fig. 4.1, with two conventional degrees of freedom V_y, r along with the longitudinal slip ratio λ at each corner, is utilized in this section and shown in Fig. 4.1. The combined-slip scheme incorporates the effect of the slip ratio, λ, and slip angle, α, simultaneously at each corner, which provides a more practical tire model. The steady-state combined-slip LuGre model with $\omega > 0$ yields

$$\bar{z}_y = \frac{v_{ry}}{\kappa R_e \omega + \frac{||M_c^2 \mathbf{v_r}|| \sigma_{0y}}{\theta g(\mathbf{v_r}) \mu_{cy}^2}}. \tag{5.39}$$

Substituting the longitudinal relative velocity $v_{rx} = R_e\omega - v_{xt}$ and lateral relative velocity $v_{ry} = v_{xt}\alpha$ in (5.39) and using (2.4), one can obtain the following normalized lateral force of the combined-slip LuGre model:

$$\mu_y = \left(\frac{\sigma_{0y}}{\kappa R_e \omega + \frac{\sigma_{0y}\sqrt{\psi}}{\theta g(\mathbf{v_r})}} + \sigma_{2y} \right) v_{xt}\alpha, \tag{5.40}$$

where $\psi = v_{xt}^2\alpha^2 \left[1 + (\eta\lambda R_e\omega / v_{xt}\alpha)^2\right]$ and $\eta = (\mu_{cx}/\mu_{cy})^2$. One can define a metric to measure how far the system is from the pure slip condition. This metric is in terms of the ratio between the *slip ratio* and *slip angle*. More specifically, based on (5.40), we introduce $\lambda R_e\omega / v_{xt}\alpha$ as a metric that can be used to identify this distance. For pure-slip, i.e., $\lambda R_e\omega / v_{xt}\alpha \ll 1$, equation (5.40) changes to (5.37), which was investigated in the previous subsection. On the other hand, when $\lambda R_e\omega / v_{xt}\alpha \gg 1$, (5.40) can be written as $\mu_{y_h} = \left(\frac{\rho}{\epsilon|\lambda| + \gamma\rho} + \sigma_{2y}\right) v_{xt}\alpha = \mathcal{K} v_{xt}\alpha$, in which $\epsilon = \eta R_e\omega$ and μ_{y_h} represents normalized lateral forces for high ratios of $\lambda R_e\omega / v_{xt}$ in the combined-slip model. This represents a linear force-slip angle relationship for the large slip ratios, as illustrated in Fig. 5.10-a by dashed lines and also substantiates the linear characteristics of all combined-slip tire curves for small slip angles α.

The general form of the lateral LuGre tire forces in (5.40) with the combined-slip

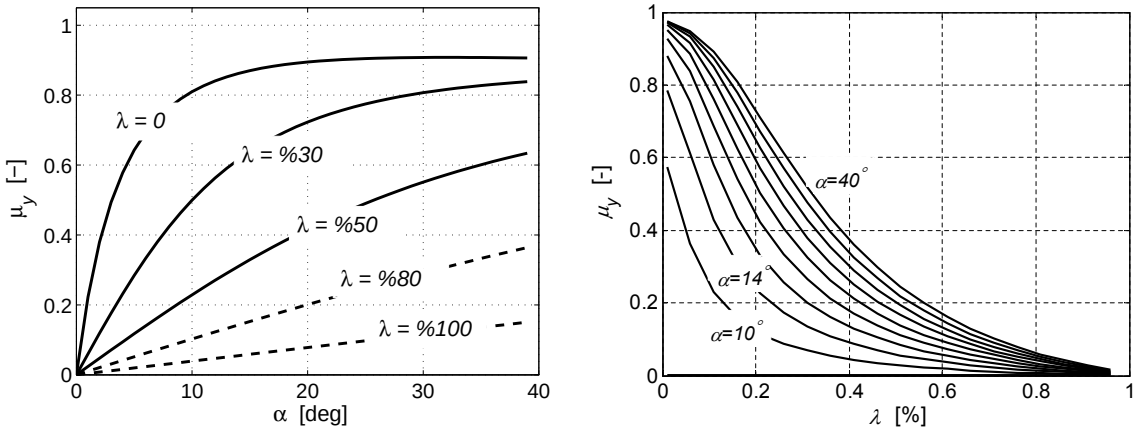

(a) Lat. force vs. slip angle

(b) Lat. force vs. slip ratio

Figure 5.10: Normalized lateral forces, combined-slip model, on a dry road $\theta = 1$ with longitudinal speed $V_x = 20\,[m/s]$.

condition, can be rewritten as (5.41) for each corner ij

$$\mu_y = \left(\frac{\rho}{\sqrt{v_{xt}^2 \alpha^2 + \lambda^2 \epsilon^2} + \gamma\rho} + \sigma_{2y} \right) v_{xt}\alpha \tag{5.41}$$

The linear and nonlinear parts in (5.38) and (5.41) are useful to develop the vehicle lateral dynamics with the yaw rate and lateral velocity as states and will be discussed in at the end of this subsection as concluding remarks. Multiplying the normalized corners' lateral forces (5.38) and (5.41) by calculated vertical forces at each corner $F_{z_{fl}}, F_{z_{fr}}, F_{z_{rl}}, F_{z_{rr}}$ from (4.24), one can get the lateral forces to be used for the vehicle lateral dynamics.

The vehicle yaw rate r and lateral velocity V_y are attainable by the following vehicle lateral dynamics with the track widths Tr_f, Tr_r, vehicle mass m, steering angle δ on the front wheels, and vehicle moment of inertia I_z:

$$\begin{aligned} m(\dot{V}_y + rV_x) &= F_{y_f}\cos\delta + F_{x_f}\sin\delta + F_{y_r}, \\ I_z\dot{r} &= (F_{y_f}\cos\delta + F_{x_f}\sin\delta)d_f + (\bar{F}_{x_f}\cos\delta - \bar{F}_{y_f}\sin\delta)\frac{T_{r_f}}{2} \\ &\quad - F_{y_r}d_r + \bar{F}_{x_r}\frac{T_{r_r}}{2}, \end{aligned} \tag{5.42}$$

in which, d_f, d_r represents axles' distances to CG and the sum of longitudinal/lateral forces at each axle are denoted by $F_{x_i} = \sum_j F_{x_{ij}}$ and $F_{y_i} = \sum_j F_{y_{ij}}$ where $F_{y_{ij}} = \mu_{y_{ij}} F_{z_{ij}}$ are obtained from the pure/combined-slip tire models (5.38) and (5.41) at each corner. As an additional note, the 2DOF bicycle model, a well-known vehicle lateral model, provides vehicle lateral velocity and yaw rate based on axles' longitudinal and lateral forces. The lateral dynamic (5.42) changes to the following form for such bicycle model:

$$\begin{aligned} m(\dot{V}_y + rV_x) &= F_{xf} sin\delta + F_{yf} cos\delta + F_{yr} \\ I_z \dot{r} &= d_f \left(F_{xf} sin\delta + F_{yf} cos\delta\right) - d_r F_{yr}, \end{aligned} \tag{5.43}$$

where V_x is the speed and subscripts f, r symbolize front and rear axles.

The proposed algorithm for road classification solves lateral dynamics (5.42) or (5.43) in discrete-time with known longitudinal speed V_x (and consequently v_{xt} at each corners' tire coordinates) for three various surface friction conditions: dry asphalt ($\theta_d = 1$), wet sealed asphalt ($\theta_w \approx 0.45$), and packed snow ($\theta_s \approx 0.25$) to get the expected vehicle lateral states V_{y_p}, r_p, then $a_{y_p} = \dot{V}_{y_p} + r_p V_x$ where p represents dry, wet, or snow conditions. The measured vehicle responses r and a_y are then checked with the expected values to define the region (road classification) based on minimum response error within a time window. This time window has also variable threshold based on the level of excitation. Majority voting or consensus can then be employed to classify the road friction condition based on the integration of the expected response error. The structure of the road classifier in illustrated in Fig. 5.11 to show interfaces between the estimation modules.

Remark: The lateral dynamics (5.43) with the tire model can be expressed as $m(\dot{V}_y + rV_x) = \mu_{yf} F_{zf} + \mu_{yr} F_{zr}$ and $I_z \dot{r} = d_f \mu_{yf} F_{zf} - d_r \mu_{yr} F_{zr}$ after utilizing the tire forces of each track $F_{yi} = \mu_{yi} F_{zi}$ and ignoring the longitudinal force effect. This leads to a state space notion of the vehicle lateral dynamics which is described in the following. Calculated normal forces on the front and rear axles F_{zf} and F_{zr} from (4.24) and the general normalized lateral forces (5.38) can be employed to form the following dynamics with states $x = [V_y(t) \quad r(t)]^T$ for the front steering case:

$$\dot{x} = A_n(t)x + B_n(t)\delta_f + H_n(t), \tag{5.44}$$

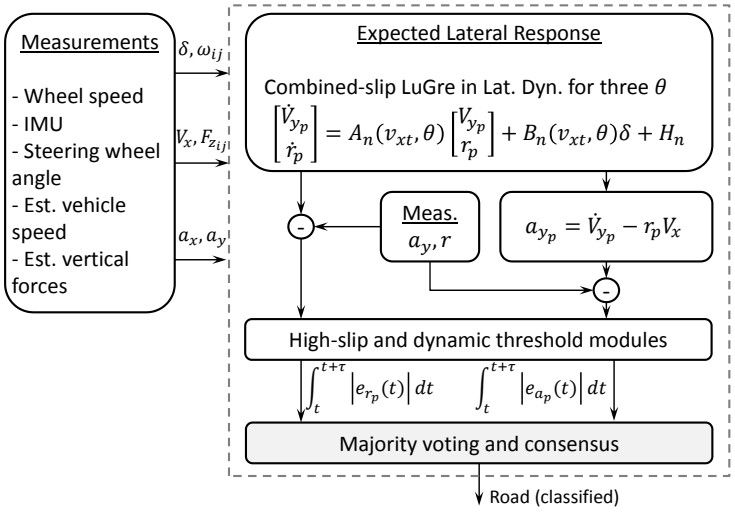

Figure 5.11: The structure of the road classifier based on the vehicle's lateral response.

where $B_n(t) = [\frac{F_{zf}}{m}k_f v_{xt} \quad \frac{d_f F_{zf}}{I_z}k_f v_{xt}]^T$ and $A_n(t)$ is defined by

$$A_n(t) = \begin{bmatrix} -(\frac{F_{zf}}{m}k_f + \frac{F_{zr}}{m}k_r) & \frac{d_r F_{zr}}{m}k_r - \frac{d_f F_{zf}}{m}k_f - v_{xt} \\ \frac{d_r F_{zr}}{I_z}k_r - \frac{d_f F_{zf}}{I_z}k_f & -(\frac{d_r^2 F_{zr}}{I_z}k_r + \frac{d_f^2 F_{zf}}{I_z}k_f) \end{bmatrix} \tag{5.45}$$

Equation (5.45) is based on the LuGre linearized model for small slip angles and is parameter-varying due to the varying wheel speed $\omega(t)$ in γ_f, γ_r and in k_f, k_r consequently. The nonlinear part can be written as:

$$H_n(t) = \begin{bmatrix} \frac{v_{xt}}{m}\left(F_{zf}\phi_f\alpha_f + F_{zr}\phi_r\alpha_r\right) \\ \frac{v_{xt}}{I_z}\left(d_f F_{zf}\phi_f\alpha_f - d_r F_{zr}\phi_r\alpha_r\right) \end{bmatrix}, \tag{5.46}$$

in which $\phi_i = \left(\frac{\rho_i}{v_{xt}|\alpha_i| + \gamma_i\rho_i} - \frac{\theta}{\gamma_i}\right)$ with $i \in \{f, r\}$ and is defined for the front and rear tires, respectively. The linear part, $A(t)$, of system (5.44) is parameter-varying due to the varying wheel speed $\omega(t)$ in γ_f, γ_r and in k_f, k_r consequently. The quadratic stability (QS) of the linear parts of the time-varying pure/combined-slip lateral dynamics are investigated in [126]. The affine quadratic stability (AQS) is also studied in [126] to find a less conservative condition than the QS and concluded that the AQS suggests more practical speed limits guaranteeing the quadratic stability of the proposed tire-vehicle lateral model.

For the combined-slip case, utilizing normal forces, the vehicle lateral dynamics can be expressed as:

$$\dot{x} = A'_n(t)x + B'_n(t)\delta_f + L_n(t), \tag{5.47}$$

where $B'_n(t) = [\frac{v_{xt}}{m}\mathcal{P}_{fn} \quad \frac{av_{xt}}{I_z}\mathcal{P}_{fn}]^T$ and $A'_n(t)$ is described as follows

$$A'_n(t) = \begin{bmatrix} \frac{-1}{m}(\mathcal{P}_{fn} + \mathcal{P}_{rn}) & -(\frac{a}{m}\mathcal{P}_{fn} - \frac{b}{m}\mathcal{P}_{rn} + v_{xt}) \\ \frac{1}{I_z}(d_r\mathcal{P}_{rn} - d_f\mathcal{P}_{fn}) & -\frac{1}{I_z}(d_f^2\mathcal{P}_{fn} + d_r^2\mathcal{P}_{rn}) \end{bmatrix}, \tag{5.48}$$

in which $\mathcal{P}_{fn} = F_{z_{fL}}k'_{fL} + F_{z_{fR}}k'_{fR}$, $\mathcal{P}_{rn} = F_{z_{rL}}k'_{rL} + F_{z_{rR}}k'_{rR}$. The parameters k'_is are defined at each corner $ij \in \{fL, fR, rL, rR\}$ independently:

$$k'_i = \frac{\sigma_{2yi} + \rho_i}{\epsilon_i|\lambda_i| + \gamma_i\rho_i}. \tag{5.49}$$

Subsequently, the nonlinear term $L_n(t)$ changes to:

$$L_n(t) = \begin{bmatrix} \frac{v_{xt}\alpha_f}{m}\mathcal{Q}_{fn} + \frac{v_{xt}\alpha_r}{m}\mathcal{Q}_{rn} \\ \frac{d_f v_{xt}\alpha_f}{I_z}\mathcal{Q}_{fn} - \frac{d_r v_{xt}\alpha_r}{I_z}\mathcal{Q}_{rn} \end{bmatrix}, \tag{5.50}$$

where $\mathcal{Q}_{fn} = F_{z_{fl}}\mathcal{M}_{fl} + F_{z_{fr}}\mathcal{M}_{fr}$ and $\mathcal{Q}_{rn} = F_{z_{rl}}\mathcal{M}_{rl} + F_{z_{rr}}\mathcal{M}_{rr}$ for the front and rear axles. $\mathcal{M}$ is defined as $\mathcal{M} = \frac{1}{N} - k' + \sigma_{2y}$ for each corner ij separately, where $N = \frac{\sqrt{v_{xt}^2\alpha^2 + \epsilon^2\lambda^2}}{\rho+\gamma}$. one significant advantage of the suggested model is that it can be used whenever normal forces at each corner are available.

The expected vehicle's response from the linear part of the combined-slip model $\dot{x}_p = A'_n(t)x_p + B'_n(t)u(t)$ to the steering input $u(t) := \delta_f$, with three known road conditions $\theta_p, p \in \{d, w, s\}$ is $x_p(t) = \Phi(t,0)x_p(0) + \int_0^t \Phi(t,\tau)B'_n(\tau)u(\tau)d\tau$ with state transition matrix $\Phi(t,0) = e^{A'_n t}$. This results in three sets of responses x_p (for dry, wet, and snowy roads), which is used to generate road classifier errors. Comparing with the measured vehicle yaw rate r, one can write the road classifier yaw rate error as

$$e_{r_p}(t) = r(t) - [0 \quad 1]\left(\Phi(t,0)x_p(0) + \int_0^t \Phi(t,\tau)B'_n(\tau)u(\tau)d\tau\right). \tag{5.51}$$

Similarly, by taking time derivatives of the expected lateral velocity response $V_{y_p}(t) = [1 \quad 0]\left(\Phi(t,0)x_p(0) + \int_0^t \Phi(t,\tau)B_n'(\tau)u(\tau)d\tau\right)$ on three different roads, the expected acceleration $a_{y_p} = \dot{V}_{y_p} + r_p V_x$ is compared with the actual measured lateral acceleration to calculate the road classifier acceleration error $e_{a_p}(t) = a_y(t) - a_{y_p}(t)$. Then the classified road opinions θ_r, θ_a, to be used for the consensus or majority voting, is calculated based on the minimum error of three models over a time window (with variable size τ) as

$$\theta_r = \arg\min_{\theta_p} E_{r_p}, \quad \theta_a = \arg\min_{\theta_p} E_{a_p}, \tag{5.52}$$

where $E_{r_p} = |\int_t^{t+\tau} e_{r_p}(t)dt|$ and $E_{a_p} = |\int_t^{t+\tau} e_{a_p}(t)dt|$. Majority voting or consensus on opinions θ_r, θ_a can then be implemented to classify the road friction condition based on the minimum error.

Finally, the general structure of the developed corner-based vehicle state estimator, road angle estimator, and road condition classifier is illustrated in Fig. 5.12 to show interfaces between the estimation modules.

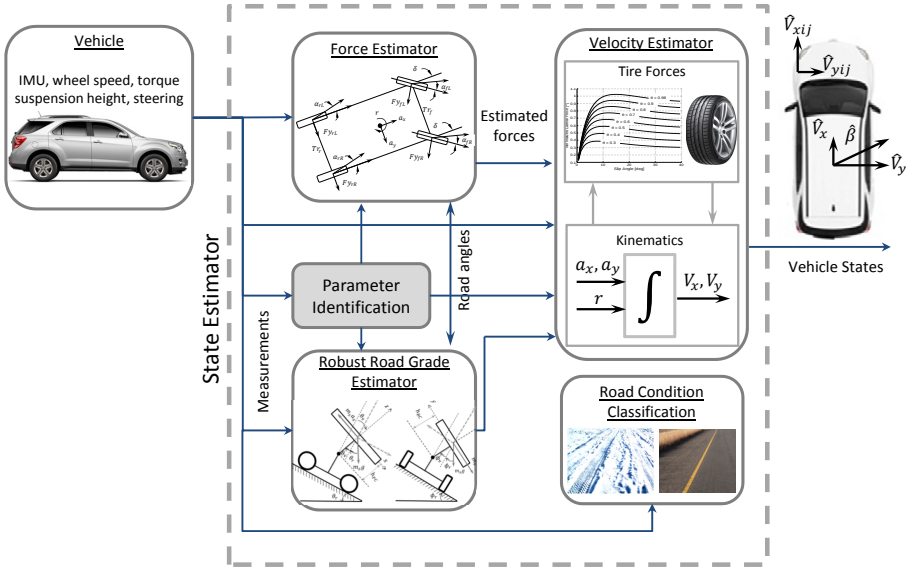

Figure 5.12: The general structure of the vehicle state and road angle/condition estimation

5.5 Simulation and Experimental Results

This section includes simulation and experimental tests for validation of the longitudinal and lateral velocity estimators on the SUV test vehicle shown in Fig 3.4-b with different driveline (AWD and FWD) configurations and the parameters given in in Table 3.1. In addition to this AWD test platform (with the capability of being used as a FWD vehicle), another test vehicle (Fig. 5.13-b) with RWD configuration, differential braking on front wheels as the stability control actuation, and specification in Table 3.1 is used to verify the proposed velocity estimators.

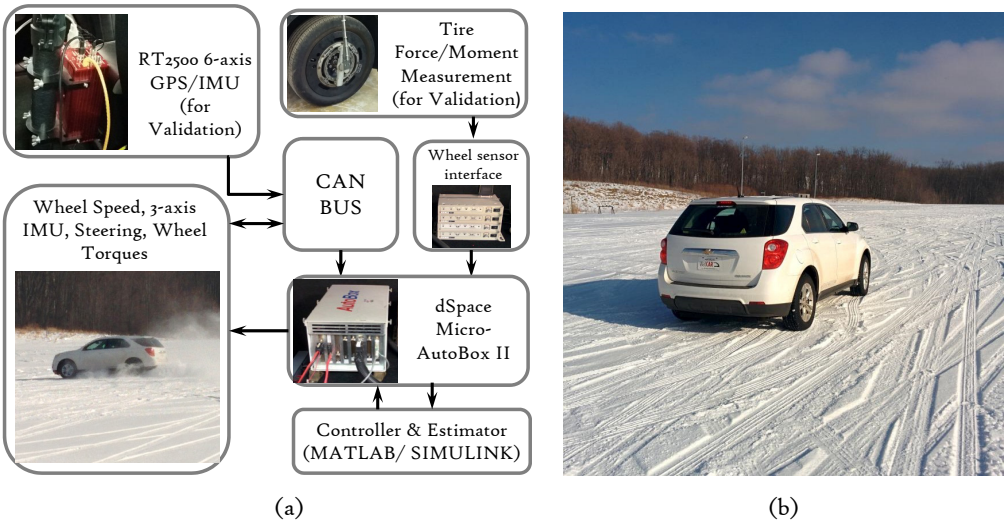

Figure 5.13: Experimental setup (a) hardware layout (b) RWD test vehicle

In the following, several driving scenarios such as launch on ice, lane change (LC) with harsh steering, double lane change (DLC), acceleration-in-turn (AiT), brake-in-turn (BiT), full turn with low excitation (FT), and acceleration with large left turn (TL) are examined on various roads and simulation/experimental results of the proposed velocity estimators (5.5), (5.19), and (5.27) are presented. For the road experiments, all season tires with the following approximate values identified by nonlinear least square, are used for both test vehicles. The rubber stiffness for the longitudinal and lateral directions are $\sigma_{0x} = 632.1, \sigma_{0y} = 181.5\,[1/\mathrm{m}]$, the rubber damping is assumed as $\sigma_{1x} = 0.76, \sigma_{1y} = 0.81\,[\mathrm{s/m}]$, relative viscous damping is $\sigma_{2x} = 0.0016, \sigma_{2y} = 0.001\,[\mathrm{s/m}]$, and load distribution factor is

$\kappa_x = 8.32, \kappa_y = 12.84$ for the velocity estimators. It should be mentioned that non of these tire parameters is changed during road experiments on diverse road conditions, which have different excitation levels, minor tire pressure changes, tire stiffness variation, and changes in the load distribution factor.

5.5.1 Longitudinal and lateral velocity estimators

To verify the proposed velocity estimator, a step steer (SS) scenario is simulated in CarSim with the initial speed $V_{x0} = 60\,[\text{kph}]$. Fig. 5.14 illustrates longitudinal velocity estimates for this SS case on dry road with steering wheel angle $\delta_{sw} = 2\,[\text{rad}]$ at $t = 2\,[\text{s}]$. The simulation confirms that the newly proposed corner-based velocity estimator provides accurate results in maneuvers with both longitudinal and lateral slips on dry road conditions.

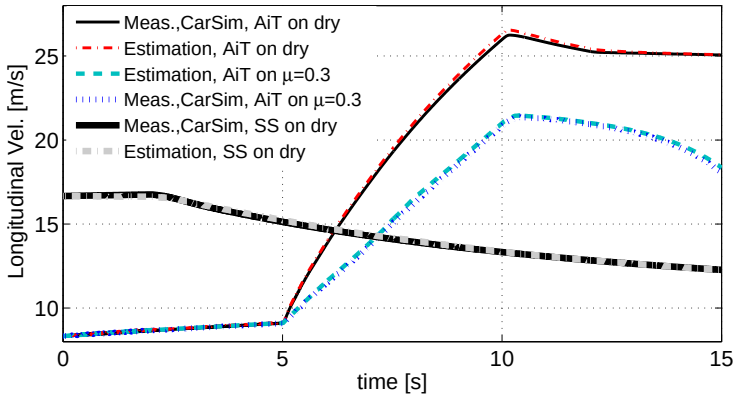

Figure 5.14: Estimated Long. velocity in SS and AiT on dry/slippery roads, CarSim.

The second set of analysis on the velocity estimator examines the suggested approach in co-simulation with MATLAB/Simulink and CarSim packages for an acceleration-in-turn (AiT) maneuver. Figure 5.14 demonstrates an AiT test with the initial velocity of $V_{x0} = 30\,[\text{kph}]$ and maximum steering wheel angle $\delta_{sw} = 1\,[\text{rad}]$ at $t = 2\,[\text{s}]$ on dry and slippery ($\mu = 0.3$) roads. Accelerator is applied to 100% at $t = 5\,[\text{s}]$ and continues till $t = 10\,[\text{s}]$. Simulation results reveal that the proposed estimator performs well on various road conditions for maneuvers with both longitudinal and lateral excitations.

Outcomes of the road experiments on the fully electrified SUVs (shown in Fig. 3.4-b and 5.13-b) are presented in the followings under three types of main maneuvers on various roads and with different driveline configurations.

Longitudinal Maneuvers

One of the main objectives of state estimators is to provide reliable longitudinal velocity $\hat{v}_{x_{ij}}$ at each corner for traction control systems during launch (or hard acceleration) on slippery roads. The proposed longitudinal velocity estimator is examined in a severe launch on a split-μ surface, which have different friction conditions on the left and right sides and the results are illustrated in Fig. 5.15. The right wheels are on ice with $\mu \approx 0.2$, the left wheels are on dry asphalt, and the powertrain configuration is AWD.

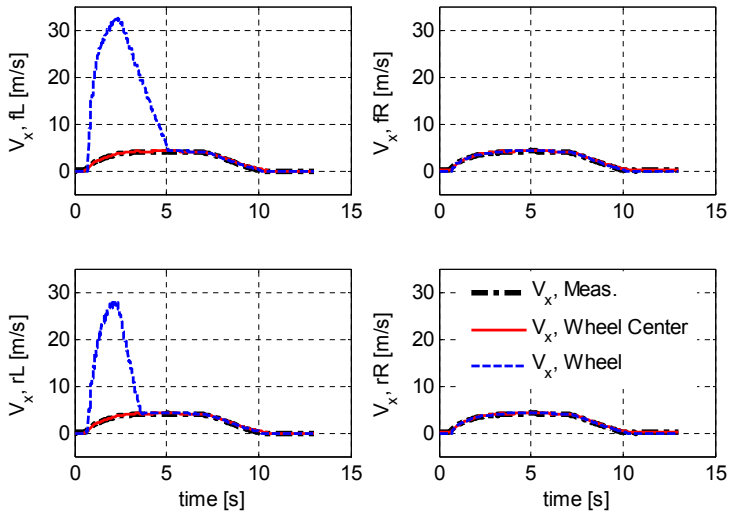

Figure 5.15: Estimated velocities and wheel speeds for AWD, split-μ on ice and dry.

Figure 5.15 demonstrates good performance of the estimator validated by the measurement from an accurate GPS at the vehicle's CG. It also shows wheel speeds on dry and icy roads. Proper time-varying observer gains lead to the observed smooth and accurate velocity estimation at corners for such high-slip conditions.

Another launch test with AWD configuration and torque vectoring (as the stability control method) is performed on a wet topped sealed asphalt with the friction coefficient

$\mu \approx 0.45$. The longitudinal velocity estimation results are provided in Fig. 5.16 and several wheel speed jumps due to high-slip cases are observed at each corner, but the suggested method with the incorporated weighted axles' estimation scheme (5.15) exhibit good performance.

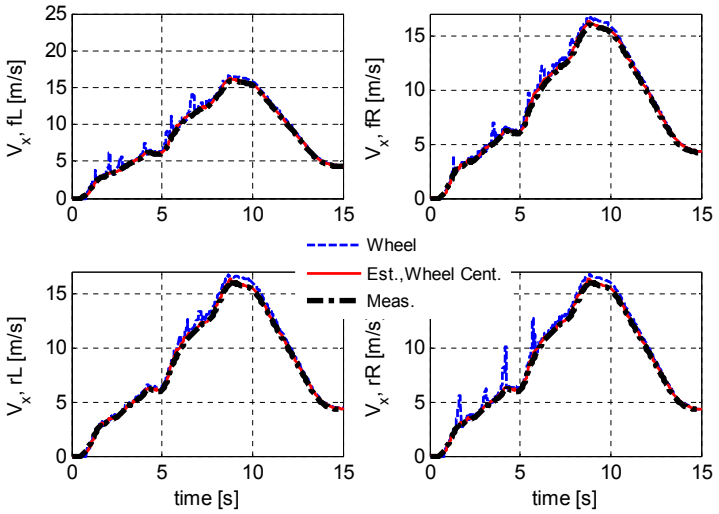

Figure 5.16: Estimated velocities and wheel speeds for AWD, launch on a wet sealer.

Furthermore, the developed longitudinal velocity estimator is examined in a harsh lane change (LC) scenario on snow with AWD configuration and acceleration/deceleration. The estimation results are compared to the measured wheel speeds and wheel center velocities in Fig. 5.17.

Figure 5.17 shows high-slip conditions at all tires, but the developed longitudinal velocity estimator provides reliable and accurate outcomes.

Steering on Dry and Slippery Roads

Steering on dry and slippery roads are conducted to examine the performance of the velocity estimators and the results are provided in this subsection. Fig. 5.18 demonstrates velocity estimation results in an LC on packed snow and ice with $\mu \approx 0.3$ for the AWD configuration.

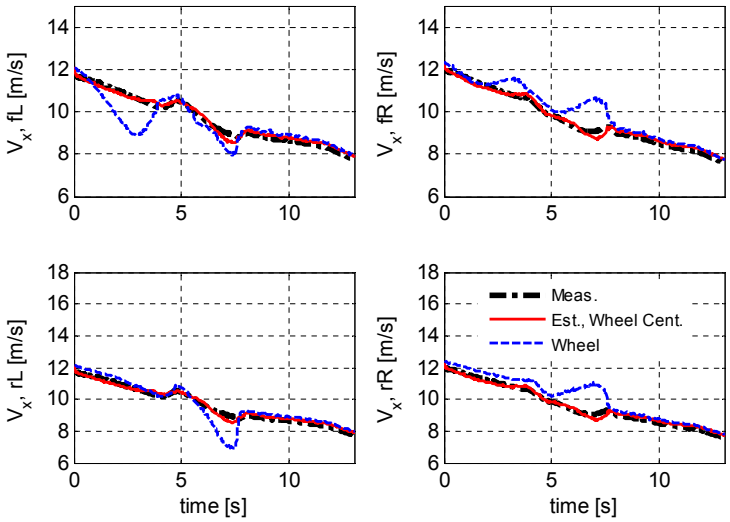

Figure 5.17: Longitudinal velocity estimates for the AWD case, LC and steering on snow.

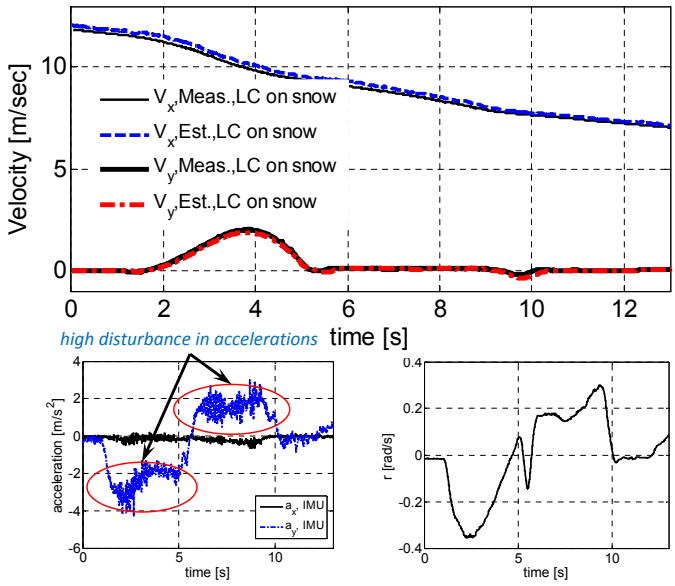

Figure 5.18: Velocity estimates for LC on snow/ice, for AWD configuration.

Fluctuations of the measured lateral acceleration and sudden changes of the vehicle yaw rate in Fig. 5.18 substantiates arduous characteristics of the driving scenario. Although the nominal vehicle total and sprung mass is used in the estimators, this test has been done

with four passengers in the vehicle and longitudinal/lateral velocity estimators' results show correspondence with the measured GPS data for such severe maneuver on a slippery surface.

The proposed estimator can also be utilized on vehicles with different driving axle configurations i.e. rear and front-wheel-drive (RWD, FWD). In order to evaluate the outcomes of the velocity estimator for a RWD configuration with torque vectoring for rear wheels and differential breaking for front wheel, a maneuver on a dry road with an oval shape has been performed on the RWD test vehicle with specifications in Table 3.1. The velocity estimation results are then validated with the measured GPS data in Fig. 5.19

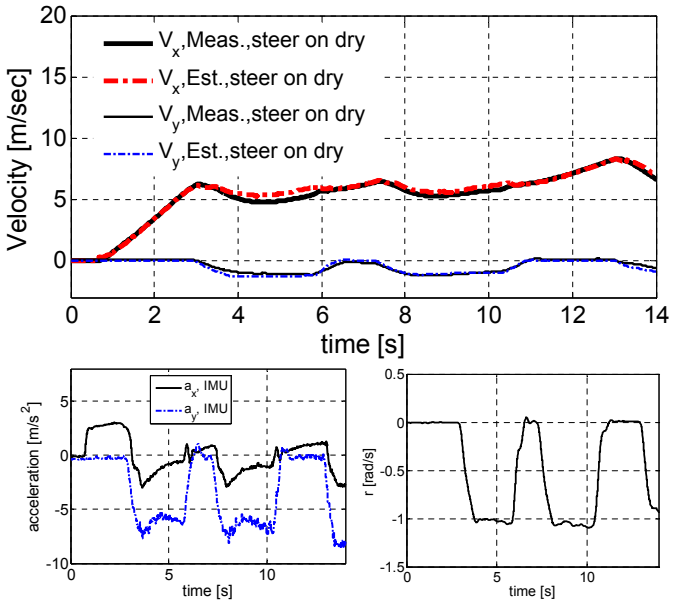

Figure 5.19: Velocity estimates for oval steering with pulsive traction on dry, RWD.

The measured accelerations and yaw rate in Fig. 5.19 resemble a harsh combined-slip maneuver with several oval steering and acceleration/deceleration, however the estimation outcome is accurate. Moreover, for this test, all tires' inflation pressure reduced 4psi intentionally to check the effect of tire properties and effective radius on the developed algorithm; the results confirm that the method is not sensitive to such reasonable changes in the tire inflation pressure. A harsh lane change on a surface with combined dry and wet conditions is performed on the RWD test vehicle with differential braking on front tires

as the stability control system and the results are presented in Fig. 5.20. The maneuver includes passing through wet to dry surfaces which leads to fluctuations in the accelerations and quick changes of the vehicle yaw rate as shown in Fig. 5.20, but the developed lateral velocity estimator exhibit good performance in presence of such disturbances.

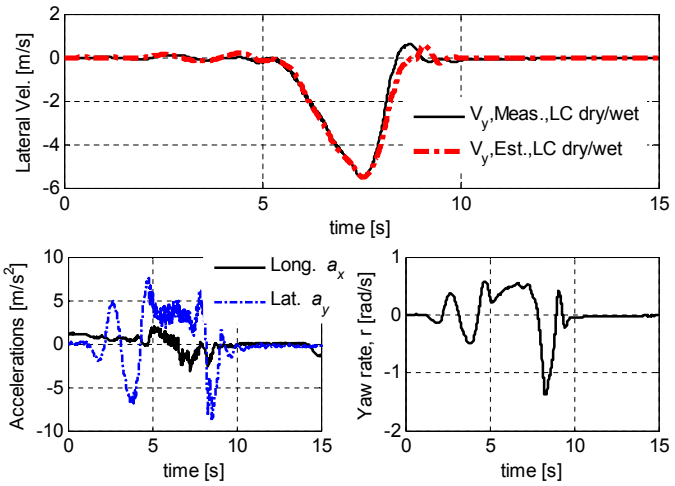

Figure 5.20: Lateral velocity estimates for RWD test vehicle, LC on combined dry/wet.

Acceleration and Brake-in-Turn on Dry and Slippery Roads

To study the velocity estimators' performance in combined-slip conditions, an acceleration-in-turn (AiT) scenario with AWD driveline configuration and torque vectoring on all wheels is done on dry asphalt with four passengers in the vehicle and results of the lateral velocity estimator are provided in Fig. 5.21

As can be seen from Fig. 5.21, high oscillations exist both in the lateral and longitudinal accelerations because of large requested toque by the driver in such severe maneuver, load transfer, and consequent high-slip regions which reduce the lateral tire capacities significantly.

The wheel speed at each corner is shown in Fig. 5.22 for this AiT on dry asphalt to demonstrate the slip condition during load transfer with additional requested torque from the driver. The wheel speed and consequently the slip ratio increases significantly

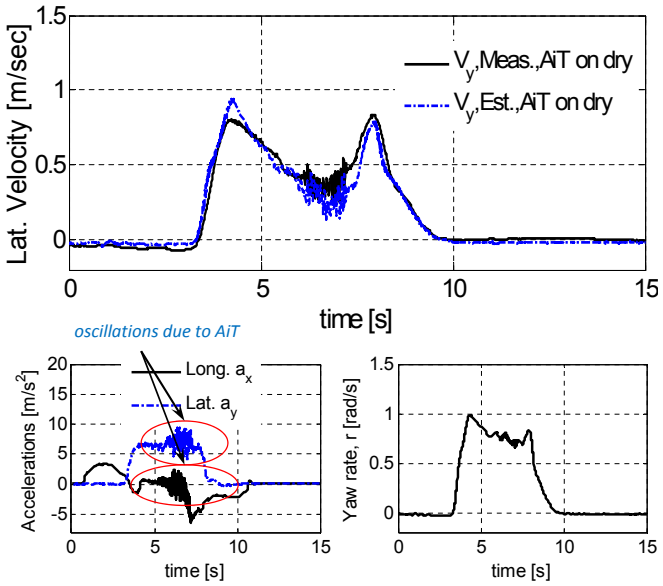

Figure 5.21: Lateral velocity estimates for AiT on dry asphalt, AWD configuration.

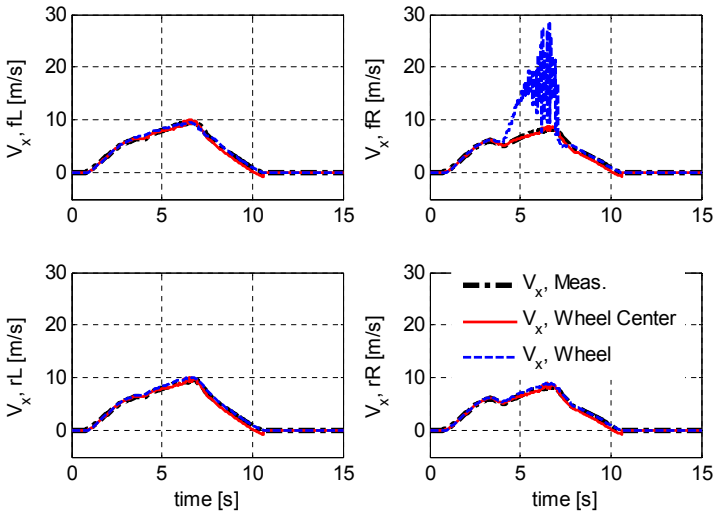

Figure 5.22: Wheel speed and estimated/measured velocities at wheel centers, AiT on dry.

between $t = 5$ and $t = 7$ [s], but the proposed state estimation methodology handles these situations and exhibit smooth and accurate outcomes even with uncertainties and changes

in the vehicle total and sprung mass.

Fig. 5.23 shows performance of the proposed longitudinal velocity estimator for the FWD case with torque vectoring in an AiT maneuver on a combined wet/dry surface with $\mu \approx 0.5$ which ended on a dry surface with a break. Moreover, a launch with a break on a highly slippery wet topped sealed asphalt with $\mu \approx 0.4$ was performed and the estimation results are provided in the same Fig. 5.23.

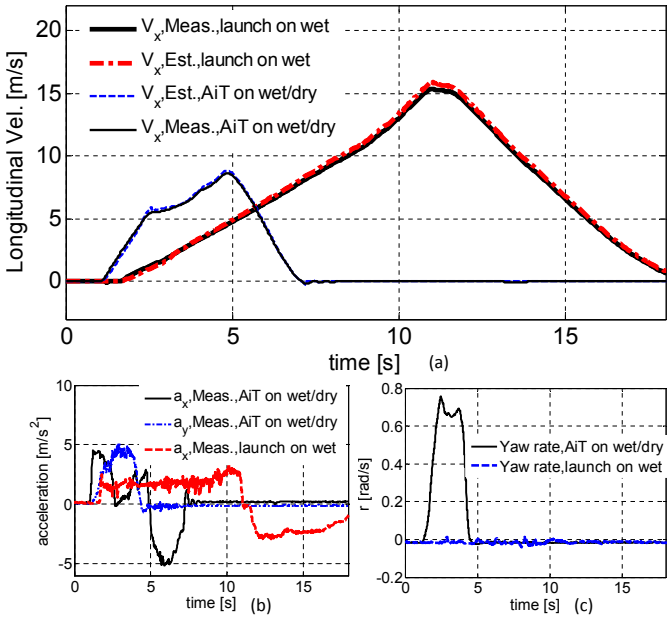

Figure 5.23: Launch and AiT on wet sealer and wet asphalt with transition to dry for FWD (a) estimated speed (b) accelerations (c) yaw rate.

The input torque from the driver for these launch and AiT scenarios on such slippery surfaces brings the tire up to their longitudinal capacity. The measured longitudinal acceleration shown in Fig. 5.23-b for the launch is bellow 3.7 $[m/s^2]$ which confirms slippery conditions based on the required accelerator pedal by the driver up to the tires' limits. For both tests, the stability (torque vectoring) and traction control systems were activated, but intentionally set to have a poor performance, which leads to sudden increase in the wheel speed and subsequently slip ratio increase at each corner.

At the beginning of these launch and AiT maneuvers, front tires loose grip due to the

drop in the vertical force on the front track by the load transfer. Therefore, high slip ratio for the front tires is a concern for traction control systems in such maneuvers. To confirm the high-slip condition on front tires, wheel speed for the front tires (fL, fR) are shown in Fig. 5.24 for these launch and AiT scenarios and compared with the estimated and measured velocities.

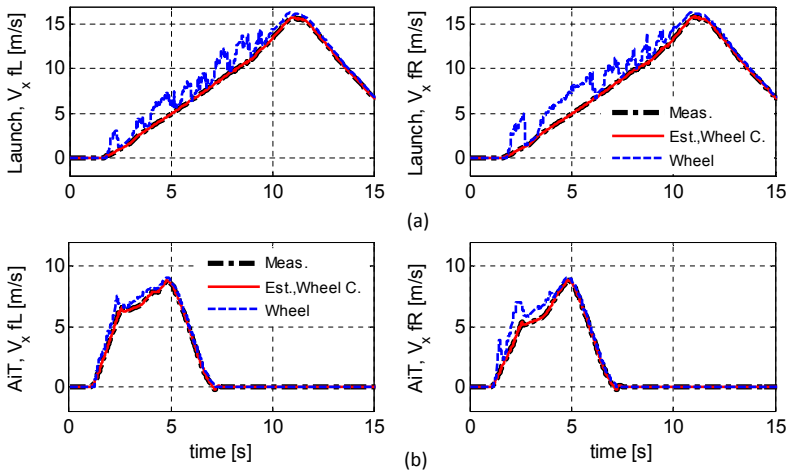

Figure 5.24: Wheel speed and estimated/measured velocities at wheel centers (Wheel C.) for (a) launch on wet sealer then dry (b) AiT on wet/dry, FWD.

The next test is an acceleration during a large left steering with RWD configuration from a wet and slippery surface with $\mu \approx 0.45$ to dry asphalt. This test is done to explore the performance of the longitudinal and lateral velocity estimators with incorporation of weighted axles' estimates schemes (5.15), (5.34) on a combined dry/wet surface. Validated estimation results with the GPS data, measured accelerations, and yaw rate are shown in Fig. 5.25.

The maneuver is demanding because of the reducing effect of the longitudinal slip on the tire lateral capacity and the transition between the dry and slippery surfaces, but the longitudinal and lateral estimators provide smooth results because of time-varying observer gains and the weighted estimated axles' velocities.

In order to evaluate the proposed approach in road experiments with combined-slip characteristics during break (with negative longitudinal slip), a brake-in-turn (BiT) ac-

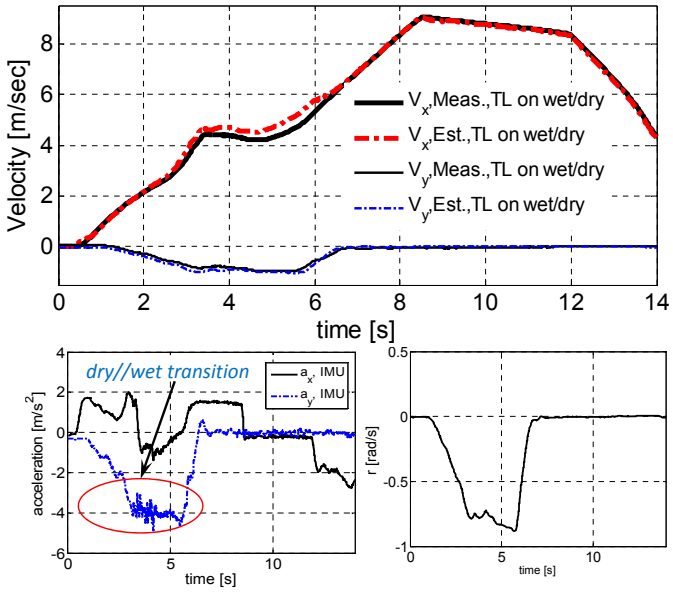

Figure 5.25: Large left turn (TL) with acceleration in RWD configuration on wet/dry.

companied by quick acceleration on packed snow (with $\mu \approx 0.35$) is done and the estimated longitudinal speed results for the AWD configuration are illustrated in Fig. 5.26. Another experiment with harsh steering on ice covered by packed snow (with $\mu \approx 0.25$) was executed and the outcomes are also demonstrated in Fig. 5.26.

Measured accelerations and the yaw rate for these BiT and harsh steering scenarios are also provided in Fig. 5.26 that shows the weak grip condition for both tests. As can be seen from Fig. 5.26-a, the developed algorithm with the high-slip detection module provides accurate velocity estimates in maneuvers with combined-slip characteristics on highly slippery surfaces. Wheel speed and estimated/measured wheel center's speed of the front tires for these BiT and steering maneuvers are illustrated in Fig. 5.27. The longitudinal velocity estimates by the proposed corner-based approach have correspondence with the measurement in spite of the large-slip cases around $t = 6\,[\mathrm{s}]$ and after $t = 11\,[\mathrm{s}]$ for the harsh steer on packed snow/ice and in $4 \leq t \leq 7.8\,[\mathrm{s}]$ for BiT on snow.

Results of such arduous maneuvers corroborates that even with presence of high slips, the proposed estimator provides accurate and reliable longitudinal and lateral velocity estimates $\hat{v}_{xt_{ij}}, \hat{v}_{yt_{ij}}$ at each tire (wheel center) and subsequently at the vehicle CG i.e.

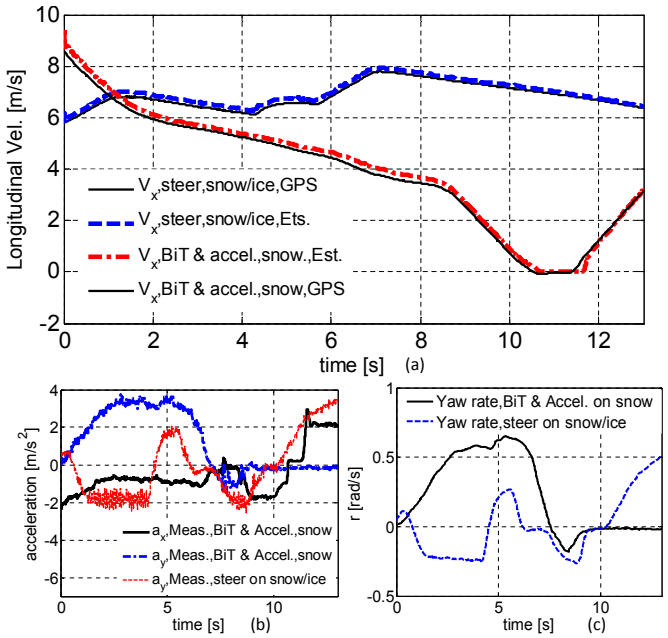

Figure 5.26: Velocity estimates for AWD, BiT on snow and steering on packed snow/ice.

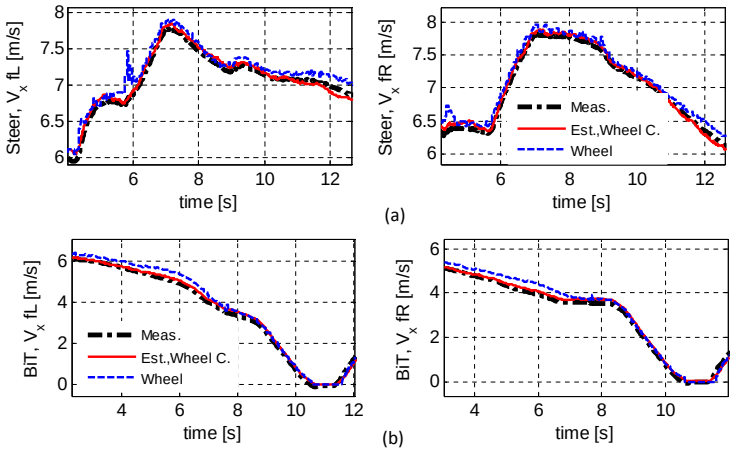

Figure 5.27: Wheel speed and estimated/measured velocities at wheel centers (Wheel C.) for (a) steering on packed snow/ice (b) BiT and acceleration on snow

$\hat{V}_x, \hat{V}_y$.

5.5.2 Lateral velocity estimator for conventional vehicles

In order to assess the proposed torque-independent lateral velocity estimation approach for conventional vehicle applications, several driving scenarios are conducted and results of three main tests are provided in this subsection. The high-slip detection module changes the covariance matrices of the Kalman-based estimator (5.27) based on the methodology and threshold discussed in (5.32) or large steering cases. This significantly improves the outcomes by defining the level of reliance on the forces for the lateral velocity estimation correction.

To check the performance of the lateral velocity estimator with different tire properties and effective radius, a severe lane change maneuver with AWD configuration and several acceleration on packed snow and ice ($\mu \approx 0.2$) is performed. Winter tires are used in this test and the controller is set to torque vectoring scheme on all wheels. The experimental results of the new lateral velocity estimator as well as the measured accelerations and the yaw rate are depicted in Fig. 5.28 for this lane change scenario.

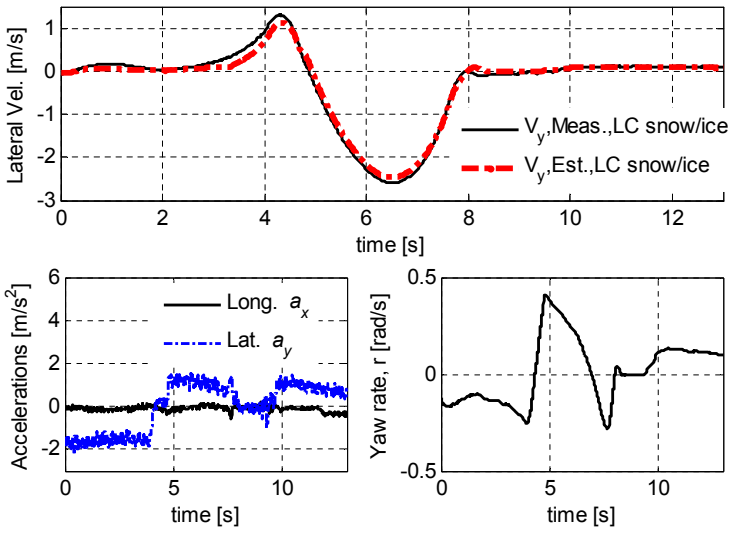

Figure 5.28: Lateral velocity estimates for AWD in an LC on packed snow and ice.

Fluctuations of the measured lateral acceleration and sudden changes of the vehicle yaw rate in Fig. 5.28 substantiate the arduous characteristics of the driving scenario. The

developed algorithm for lateral velocity estimation, without using wheel torques (and longitudinal forces), performs well by using high-slip detection modules even with different tire properties (winter-type) and effective radius ($R_e = 0.352\,[\mathrm{m}]$).

The performance of the new torque-independent approach in low excitation maneuvers is evaluated in a full turn maneuver on a surface with varying friction type from dry to wet and the results are depicted in Fig. 5.29. The powertrain is set to RWD with differential braking on front wheels.

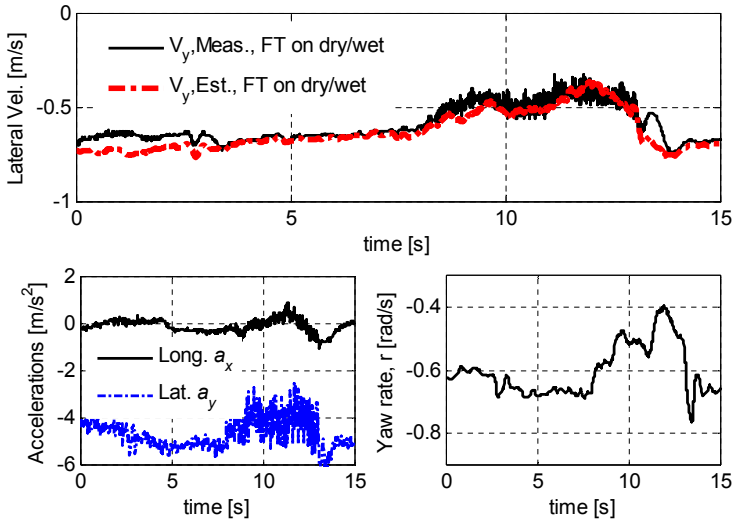

Figure 5.29: Lateral velocity estimates for FT on dry/wet, RWD

In spite of low excitation, which is challenging for current lateral state estimators in production vehicles, and the observed oscillations in the measured lateral acceleration due to several passing through dry and wet surfaces, the new algorithm exhibits accurate estimates that is promising.

A double lane change scenario is also done on snow with $\mu \approx 0.45$ for the AWD case with four passengers, torque vectoring as the stability control scheme, and all-season tires; results are shown in Fig. 5.30 that confirm accuracy of the lateral state estimator.

The covariance matrix changes in high slip/steering cases and weighted track's estimates lead to the observed smooth and accurate lateral velocities at the vehicle CG and corners

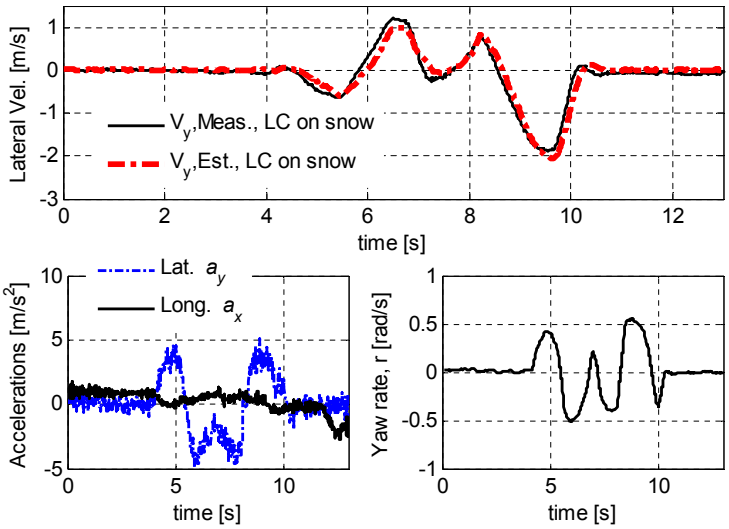

Figure 5.30: Lateral velocity estimates for DLC on snow, AWD

for conventional vehicle applications without having the wheel torques and accurate vehicle mass even in maneuvers with high-slip conditions.

Accuracy of the developed estimators are evaluated in different maneuvers with the normalized root mean square of the error, *NRMS*, defined by $\varsigma = \frac{\sqrt{\sum_{i=1}^{N_p}(\hat{p}_i - p_i)^2/N_s}}{p_m}$ similar to the criteria for the force estimators. Over 170 and 140 road tests have been done for the electric AWD and RWD vehicles, respectively. The lateral state estimator for conventional cars has been experimentally tested with AWD and RWD configurations over 120 times to check the accuracy and reliability of the algorithm. The number of collected signal samples during a driving scenario is denoted by N_p and the estimated and measured signals are denoted by $\hat{p}$ and p respectively. The maximum value of measured signals is $p_m = \max_{i=1...N_p} |p_i|$. Performance of the longitudinal and lateral velocity estimators are investigated in Table 5.1 for two test vehicles with AWD and RWD powertrain configurations in different driving conditions (* shows tests with four passengers in the car).

The velocity estimators for both electric and conventional vehicles exhibit reliable performance in various driveline configurations and stability control schemes for the maneuver with the pure-slip characteristics (i.e. launch, normal driving, lane change, acceleration/deceleration) as well as the combined-slip ones (i.e. acceleration-in-turn and brake-in-

Table 5.1: Velocity Estimators' Error *NRMS* for AWD and RWD Configurations

Maneuvers	Estimated Vx		Estimated Vy	
	$\varsigma_x[\%]$	$p_m[\mathrm{m/s}]$	$\varsigma_y[\%]$	$p_m[\mathrm{m/s}]$
AWD				
Launch on ice/dry, split μ	2.64	4.14	0.2	0.08
AiT on dry *	4.61	9.1	6.3	0.83
Steering & Accel./Deccel., snow	3.38	9.98	4.11	4.04
LC on snow	1.6	11.86	3.29	2.02
RWD				
Oval steering on dry	3.15	8.38	7.6	1.24
Accel. & left turn dry/wet	2.07	9.06	5.91	0.95
Full turn on dry	0.65	9.01	7.15	0.52
Full turn on dry/wet	0.79	7.51	6.21	0.74
Conv. Lateral Estimator	AWD		RWD	
	$\varsigma_y[\%]$	$p_m[\mathrm{m/s}]$	$\varsigma_y[\%]$	$p_m[\mathrm{m/s}]$
LC on snow/ice *	4.8	2.86	2.9	3.27
Full turn on dry/wet	5.1	1.01	6.4	1.2
AiT on packed snow	6.9	1.17	7.8	1.32

turn), in which the tire capacities reduces significantly both in the lateral and longitudinal directions. The simulation and experimental results provided in this section show that the suggested method can provide longitudinal/lateral state estimates with various controller schemes, in the absence of road friction details, wheel torques, and uncertainties in the tire (type, radius, inflation pressure) and vehicle mass.

5.5.3 Road classification based on vehicle lateral response

Several driving scenarios are performed and results are provided in this subsection to verify the proposed road classifier during maneuvers with high and low excitation levels, which are challenging for the current road identification approaches.

To show the performance of the road classification approach in low excitation maneu-

vers, a full turn scenario is done on dry asphalt for the AWD case with torque vectoring as the stability controller. Results of the errors between the measured and the expected lateral response of the vehicle with combined-slip model are shown in Fig. 5.31 that confirm accuracy of the model with dry asphalt parameters. Measured longitudinal/lateral accelerations and the vehicle yaw rate are also provided in Fig. 5.31, which shows low excitation without reaching the lateral limit (i.e. $a_y = 6$ that is significantly less than $10\,[\mathrm{m/s^2}]$).

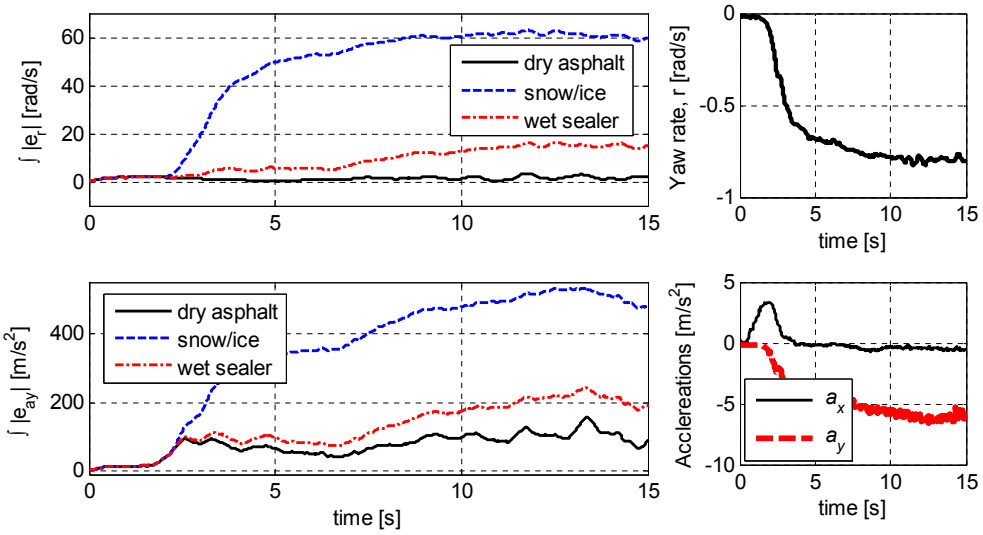

Figure 5.31: Road classifier results and measurements for a full turn on dry asphalt, AWD

The lateral dynamics model (5.47) with the combined-slip effect is utilized for comparison between the expected and the measured responses in the road experiments of this subsection. A harsh acceleration-in-turn maneuver on dry asphalt is conducted and results are shown in Fig. 5.32 to evaluate the approach in cases with reduced lateral tire capacities due to the high slip ratio. This scenario is demanding because of fluctuations in the measured accelerations and high slip ratio.

The wheel speeds for this AiT scenario are illustrated in Fig. 5.22, which shows extreme slip on the front-right tire due to the load transfer. As can be seen from Fig. 5.32, the error norm over a time window for the dry road is less than the snow and wet classifiers and the approach exhibits correct outcomes even in presence of high slip at a corner.

A lane-change with several high slip cases at each corner is done on a surface with

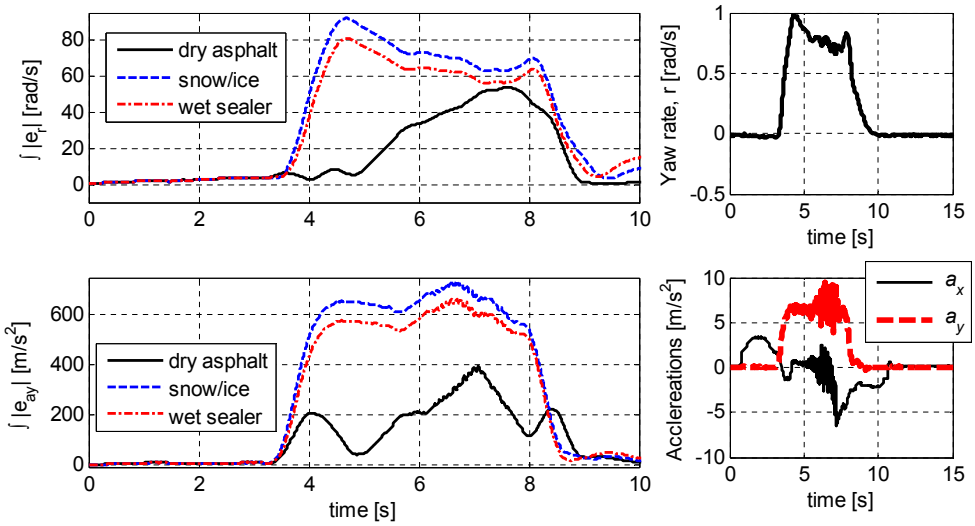

Figure 5.32: AiT with high slip on dry asphalt, road classification for AWD

packed snow and ice and the road classifier results together with the acceleration/yaw rate measurements are illustrated in Fig. 5.33.

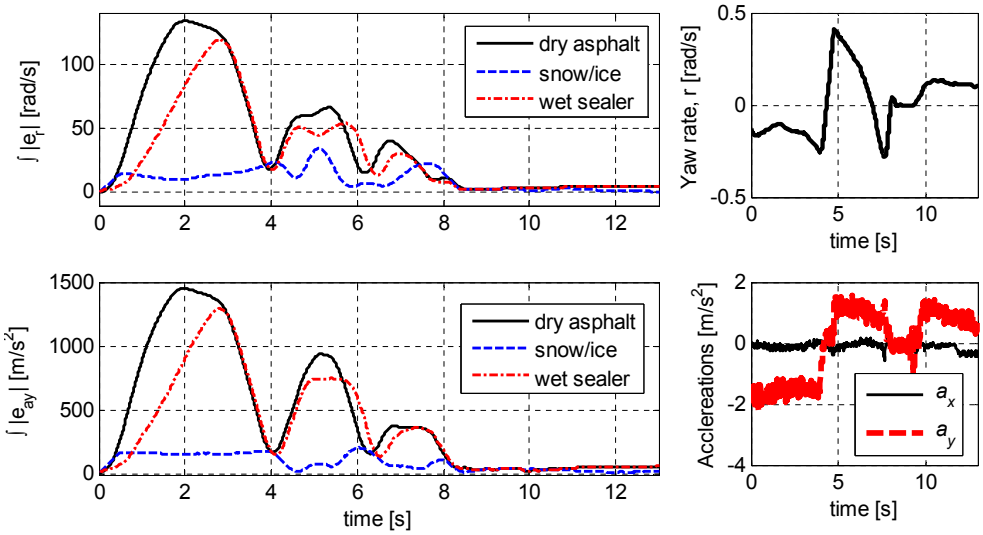

Figure 5.33: Road classification results for AWD case in an LC on packed snow and ice

Fig. 5.17 demonstrates wheel speeds during this maneuver and shows several high slip

cases from $t = 1$ to $t = 8$ [s]. The algorithm shows good performance for such lane change with high slip ratio episodes. To check the outcome of the proposed approach in maneuvers on surfaces with varying surface friction, a harsh full turn with pushing the vehicle up to its lateral tire capacities is performed on a surface with half dry and half wet conditions and the results are shown in Fig. 5.34.

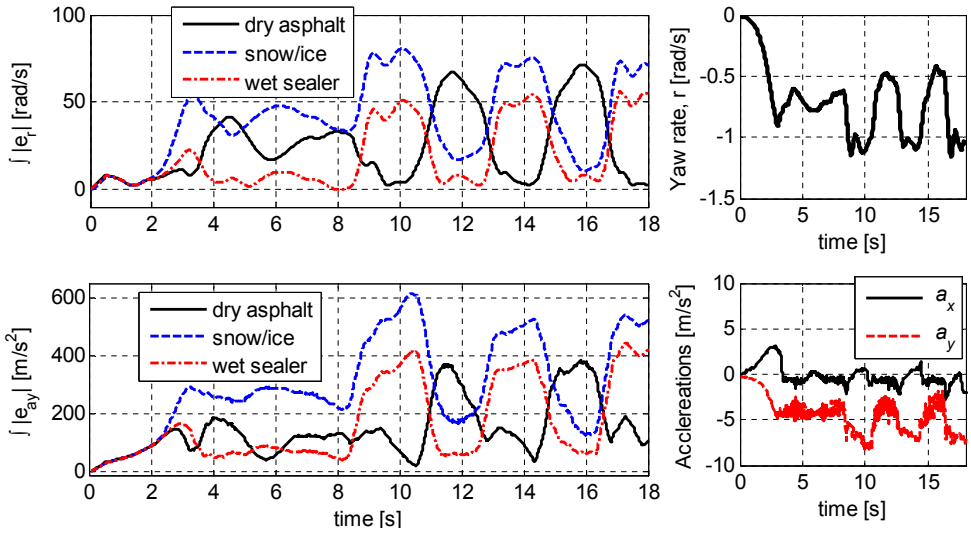

Figure 5.34: Full turns on dry/wet with the AWD vehicle, road classification results

This driving scenario is arduous because of its low excitation characteristics and changing surface friction as shown in Fig. 5.35, but the developed estimator works well and can detect various surface condition. As can be seen from Fig. 5.34, during $3 < t < 8.5$ [s], $11 < t < 13$ [s], and $15 < t < 17$ [s] the detected surface is wet sealer and it has correspondence with the measured lateral acceleration of the vehicle, that is brought to its lateral stability edge, during the mentioned periods.

One difficult test for evaluation of road classifiers is mild driving on dry surfaces, which may be interpreted as the low-friction surface. The same has been done during a mild sine steering on dry asphalt for the AWD test vehicle and results are presented in Fig. 5.36.

The results confirm correct classification of the road friction during such a mild maneuver on dry asphalt.

Figure 5.35: AWD vehicle in full turns on dry/wet sealer

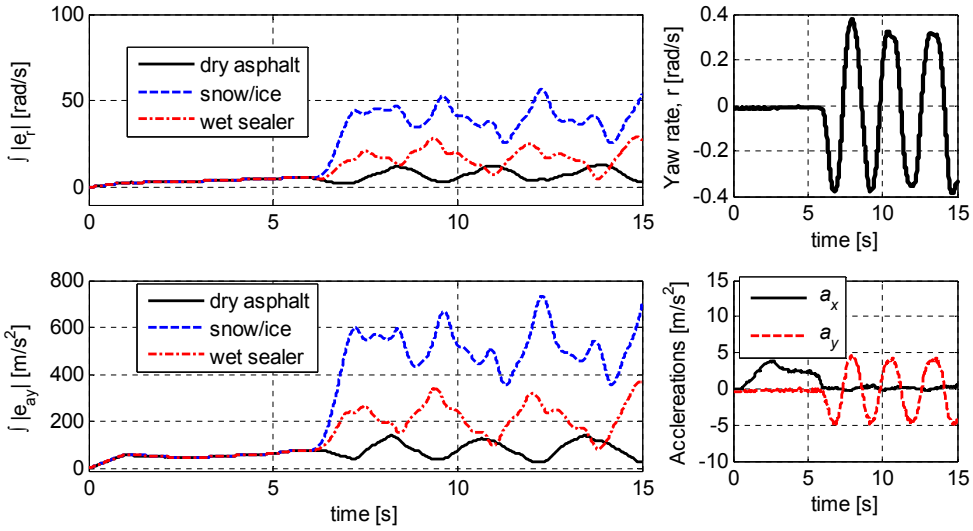

Figure 5.36: Road classification for a mild sine steering on dry asphalt, AWD

5.6 Summary

A method to estimate longitudinal and lateral velocities at vehicle's CG and each corner robust to road conditions were provided in this chapter. The developed structure can be integrated with road angle estimators and active safety systems, to ensure reliable performance of such systems in presence of model uncertainties (such as vehicle mass), tire

parameter changes (type and radius), and road friction changes.

To tackle the limitations of the kinematic and dynamic-based velocity estimation approaches, the average Lumped LuGre model and the kinematics were coupled at each corner to estimate the longitudinal and lateral velocities using a linear parameter-varying model with the road friction as uncertainties. The stability and robustness of the velocity estimators' error dynamics was investigated with the affine quadratic stability approach.

A lateral observer was also designed with variable weighted axles' estimates for large steering and high slip cases for conventional vehicle applications. The developed estimator was tested in different maneuvers and driveline configurations and can be transferred from one vehicle to another.

Furthermore, the pure and combined-slip models, which consider reduction in the tire capacities due to slip ratio/angle, are incorporated into the vehicle lateral dynamics to monitor the vehicle response for road classification. A road friction classifier, which employs the vehicle lateral response with pure and combined-slip friction models, is developed in this chapter. The proposed method calculates expected vehicle's lateral response for various surface frictions and compares the expected values with the measured ones to define the region based on minimum response error. The algorithm was validated in low-excitation, near-saturation, and nonlinear regions of tire forces.

Several road experiments with normal and harsh driving conditions were conducted on dry and slippery roads to validate the approach. The results of the road experiments substantiate that the vehicle state estimation and road classification algorithms can handle various friction conditions with AWD, FWD, and RWD powertrain configurations and with different tire properties such as type (winter/all-season), effective radius and inflation pressure.

Chapter 6

Conclusions and Future Work

6.1 Conclusions and Summary

In this thesis, a holistic corner-based estimation of the vehicle states robust to road friction conditions regardless of the vehicles driveline configuration was proposed. Two observers were also designed for road angles and road friction conditions.

The first objective of this thesis is met and an unknown input observer was developed in this thesis on the roll and pitch dynamics of the vehicle and experimentally validated in real-time to estimate the road bank and grade angles. The proposed road angle estimation algorithm worked for different types of separate and combined banked/graded roads in various driving conditions. The approach does not require any information about the road friction, tire forces, and tire parameters. This enables the algorithm to perform reliably on different road conditions without any sensitivity to the tire and friction parameters. Road disturbances and outliers are isolated in the provided method using a variable threshold based on the longitudinal and lateral excitations of the vehicle.

Incorporating road-body kinematics helped to achieve more accurate vehicle angle measurements. Road angle estimation in maneuvers with high excitation on banked/graded roads, fast convergence, and robustness against road disturbances and outliers are main advantages of the proposed methodology. The current vehicle state estimators on the instrumented test platform is robust to errors in the road angle estimation up to 2 [deg]

and the developed UIO exhibits errors less than this value. Moreover, the proposed algorithm can be integrated with various vehicle state estimators and active safety systems (e.g. stability control and roll-over prevention systems) to enhance the performance of such systems in the presence of accelerations, roll rate and pitch rate measurements affected by road inclinations.

This thesis presented a novel integrated force estimation method to monitor tire capacities required for the traction and stability control systems. This is essential for more advanced vehicle stability control systems in autonomous vehicles during harsh maneuvers on slippery surfaces. The longitudinal, lateral, and vertical force estimators require available measurements on production vehicles (acceleration, wheel speeds, yaw rate, and steering angle), were experimentally tested in several maneuvers on different roads, and the results confirmed the accuracy and robustness of the method. A Kalman filter and a nonlinear observer were utilized for estimation of the lateral and longitudinal tire forces without road friction information. The lateral force estimator can address the cases in which tires are on surfaces with various road friction since the UKF-based lateral force estimator is developed without any assumption on the lateral force distribution and tire parameters. The presented corner-based tire force estimation has the advantage over methods using double track models because it can exhibit saturation and capacity conditions of all tires. In addition, it uses conventional measurements in production vehicles, does not implement any tire model, can be transferred from one vehicle to another, and is independent from changes in the road friction or tire parameters due to wear, inflation pressure, temperature, etc., thus, the second objective of this thesis is met. The proposed Kalman filter with adaptive covariance matrices based on the wheel's rotational acceleration can handle dry and slippery roads with the normalized RMS less than 7.1% for the lateral forces in demanding maneuvers. Moreover, the longitudinal force estimator deals with the model uncertainties using robust observer design, which leads to normalized RMS less than 6.4%. The stability and performance of the estimators are also studied and it is shown that the proposed integrated structure is robust to model uncertainties.

A generic velocity estimation method using the average Lumped LuGre model at each corner was proposed in this thesis, and its performance was studied. To address the limitations of the dynamic and kinematic-based velocity estimators, the LuGre tire model and the vehicle kinematics were combined at each corner to estimate the longitudinal and

lateral velocities. Utilizing the dynamics of the LuGre's internal deflection states, the velocity estimators form a linear parameter-varying model with the road friction conditions under each tire as uncertainties. In addition, an unscented Kalman filter was proposed and experimentally verified for estimation of lateral velocities and tire slip angles in conventional vehicles. Stochastic observability of the developed lateral velocity estimator for conventional vehicles was also investigated. The developed longitudinal and lateral velocity estimators require conventional measurement in production vehicles and can be transferred from one vehicle to another.

The velocity estimation algorithm detects large slip ratio cases with an adaptive high-slip threshold, based on the excitation level. This is to use the weighted estimated velocities at each corner for the LPV approach or to allocate adaptive covariance matrices and tackle the noises associated with harsh maneuvers in the Kalman-based state estimator for conventional vehicles.

One significant advantage of the suggested velocity estimator is that a unidirectional lumped LuGre model could be used instead of the combined one since the term containing the combined friction model, i.e. $\frac{\sigma_{0q}|V_{rq}|}{\theta g(V_{rq})}\bar{z}_q$, was considered as uncertainty.

The velocity estimator can be integrated with road angle estimators, stability control systems, traction control systems, and roll over prevention, to ensure reliable performance of such systems with model uncertainties and road friction changes. In addition, while preserving the overall structure of the estimation, one can replace or modify velocity estimators independently because of the modularity of the developed structure.

The proposed algorithm for road classification calculates vehicle lateral response in discrete-time with known longitudinal speed for three various surface friction conditions: dry asphalt, wet sealed asphalt, and packed snow to get the expected vehicle lateral states and lateral acceleration. The measured yaw rate and lateral acceleration are then checked with the expected values to define the region (road classification) based on minimum response error within a time window. This time window has also variable threshold based on the level of excitation. Sensitivity of the model-based classification to the tire model parameters, inflation pressure, and effective rolling radius is not an issue in this approach since the expected lateral response is calculated for all three surface frictions with the same model parameters.

Software co-simulations were utilized to test the proposed state estimation methods using MATLAB/Simulink and high-fidelity models of the available electric SUVs in the CarSim packages. The performance of the tire force and velocity estimators were evaluated on various road conditions such as dry, wet, and snowy and in different scenarios such as launch and brake, acceleration-in-turn, and step steer. The simulations demonstrate the effectiveness of the estimation approach on several roads and in diverse driving scenarios with pure and combined-slip conditions.

Road experiments were also conducted with different vehicles, driving conditions, vehicle powertrain configurations, and tire types/properties. The proposed velocity, tire force, and road condition estimation schemes were implemented in real-time on dSPACE® MicroAutobox and tested on two electric vehicles with AWD, RWD, and FWD cases. Various surface friction conditions such as dry asphalt, wet top-sealed asphalt, packed snow, and ice were also used to examine the robustness of the estimators. The vehicle state and road condition estimators were observed to provide reliable outcomes in various driving scenarios with two types of tires for the available stability control systems. This preeminence of the algorithm makes it appropriate for a wide range of vehicles' traction configurations. The simulation and experimental results confirm robustness and accuracy of the designed LPV observers, thus the third objective of the thesis is met. The real-time pure and combined-slip road classification algorithm based on the vehicle lateral dynamics also exhibits good accuracy for high and low-excitation maneuvers.

6.2 Future Work

A few suggestions are made in this section for future works to enhance the accuracy of the developed vehicle state and road angle estimators, and to continue the work done in this thesis.

- Improve the model of the unknown input observer for combined bank and grade cases: Road-body kinematics has been investigated in this thesis to increase the accuracy of the measurement in the road angle estimator by defining the correlation between the road angle rates and the pitch/roll rates of the vehicle. However, there are some errors for the combined bank and grade cases which stems from separated vehicle

roll and pitch dynamics in the observer model. Therefore, considering the coupled roll and pitch dynamics in the unknown input observer structure can improve the accuracy of the estimator.

- Using road friction information for the road angle estimator: Tire forces and the vehicle lateral (or longitudinal) dynamics have not been integrated into the roll (or pitch) dynamics for the bank (or grade) angle estimation because of unavailability of road friction information. Employing road classification data in the tire forces and the expected vehicle responses (from the predefined tire curves) facilitates estimation of the road angles. This is because of distinguishing between the measured accelerations due to road angles and the ones due to the vehicle kinematics in various maneuvers. Consequently, by including tire forces, which are obtained from road friction information, the road angles can be estimated more accurately.

- Considering camber angle: In order to design a reliable tire force estimator to address demanding cases with combined longitudinal and lateral excitations, a precise vehicle model is needed. The imprecision of the vehicle dynamics can be rooted in an inaccurate tire forces due to not considering the camber angle at each corner. The current corner-based force estimation does not include the camber angle effect, but the tire forces and consequently the vehicle's planar and roll dynamics are affected by this angle at each corner. Hence, incorporation of the tires' camber angles into the vehicle planar kinetics can result in better performance of the current force estimators.

- Designing an integrated state estimation: The accuracy of the proposed corner-based velocity estimation approach can be enhanced by employing a general chassis model. The main purpose of such model is to estimate corner velocities more accurately with implementation of an integrated force/velocity observer to overcome estimation errors due to uncertainties in the road friction. The mentioned methodology provides kinematic estimates of all tires simultaneously and incorporates other corners longitudinal/lateral forces in the estimates of each corner states (relative velocities) using an additional observer on the measured accelerations and yaw rate. However, this will increase the computational load of the state estimators. Moreover, the author is working on a new failure detection and reliability measure to address the bias-type as

well as slope-type failures (discrepancies) of the estimated velocities using additional measurements or dynamics

- Estimation of wheel torques for conventional vehicles: By implementing slip ratio from GPS (or a torque-independent longitudinal velocity estimation [114]) and slip angle from GPS (or the lateral velocity estimator discussed in Section 5.3.1) into the vehicle and wheel dynamics, the proposed integrated force estimation equations can be rewritten in terms of wheel torques. Nonlinear or Kalman observers then can be used to estimate the wheel torques at each corner. The same approach can be used for vehicles with electronic limited slip differential (eLSD). Therefore, the integrated force estimation structure proposed in this thesis can be used to estimate wheel torques by including eLSD dynamics and total torque data from the engine/powertrain.

- Road classification in the longitudinal direction: The road classification method in this thesis is designed to classify the road friction condition based on the lateral response of the vehicle. An avenue for future work in this direction is to use the vehicle's longitudinal response and stability of each wheel based on the wheel acceleration and slip ratio to develop an algorithm, which classifies road friction conditions during maneuver with longitudinal excitations. Therefore, the velocity estimates from the proposed methods in this thesis together with wheel speed measurement and IMU data can be employed to design an accurate observer for road classification in the longitudinal direction.

- The closed-form lateral dynamics with combined-slip model for the stability controllers: The suggested general forms of the tire-vehicle lateral models in Section 5.4 provide a framework to achieve analytical solutions for vehicle's optimal stability control problems. This has a significant advantage over the cascaded methods that need slip ratio/angles to calculate forces (in a tire model) and then to calculate vehicle states by solving lateral dynamics and tire forces. This is more pronounced for designing stability controllers in performance cars because of severity of maneuvers, over-steering characteristics of the vehicle, and several high-slip cases.

References

[1] Alena Erke. Effects of electronic stability control (esc) on accidents: A review of empirical evidence. *Accident Analysis & Prevention*, 40(1):167–173, 2008.

[2] Alena Høye. The effects of electronic stability control (esc) on crashesan update. *Accident Analysis & Prevention*, 43(3):1148–1159, 2011.

[3] Transport Canada. Electronic stability control, 2013.

[4] Allan Lyckegaard, Tove Hels, and Inger Marie Bernhoft. Effectiveness of electronic stability control on single-vehicle accidents. *Traffic injury prevention*, 16(4):380–386, 2015.

[5] Nicholas S Johnson and Hampton C Gabler. Reduction in fatal longitudinal barrier crash rate due to electronic stability control. *Transportation Research Record: Journal of the Transportation Research Board*, (2521):79–85, 2015.

[6] M Starnes. Estimating lives saved by electronic stability control, 2008–2012. Technical report, 2014.

[7] H.B. Pacejka and R.S. Sharp. Shear Force Development by Pneumatic Tyres in Steady State Conditions: A Review of Modelling Aspects. *Vehicle System Dynamics*, 20(3-4):121–175, 1991.

[8] H. B. Pacejka and I. J. M. Besselink. Magic Formula Tyre Model with Transient Properties. *Vehicle System Dynamics*, 27:234–249, 1997.

[9] RT Uil. *Tyre Models for Steady-State Vehicle Handling Analysis*. PhD thesis, Eindhoven University of Technology, 2007.

[10] CL Clover and JE Bernard. Longitudinal tire dynamics. *Vehicle System Dynamics*, 29(4):231–260, 1998.

[11] Joško Deur, Jahan Asgari, and Davor Hrovat. A 3D Brush-Type Dynamic Tire Friction Model. *Vehicle System Dynamics*, 42(3):133–173, 2004.

[12] Wei Liang, Jure Medanic, and Roland Ruhl. Analytical Dynamic Tire Model. *Vehicle System Dynamics*, 46:197–227, 2008.

[13] C. Canudas-De-Wit and Panagiotis Tsiotras. Dynamic Tire Friction Models for Vehicle Traction Control. In *proceedings of the 38th Conference on Decision & Control*, pages 3746–3751, 1999.

[14] C. Canudas-De-Wit, M.L. Petersen, and A. Shiriaev. A New Nonlinear Observer for Tire/Road Distributed Contact Friction. In *42nd IEEE International Conference on Decision and Control (IEEE Cat. No.03CH37475)*, volume 3, pages 2246–2251, 2003.

[15] Panagiotis Tsiotras, Efstathios Velenis, and Michel Sorine. A LuGre Tire Friction Model With Exact Aggregate Dynamics. *Vehicle System Dynamics*, 42(3):195–210, 2004.

[16] E. Velenis, P. Tsiotras, C. Canudas-de Wit, and M. Sorine. Dynamic tyre friction models for combined longitudinal and lateral vehicle motion. *Vehicle System Dynamics*, 43(1):3–29, 2005.

[17] K. J. Astrom and C. Canudas-de Wit. Revisiting the LuGre Model. *IEEE Control Systems Magazine*, 6:101–114, 2008.

[18] Carlos Canudas-de Wit, Panagiotis Tsiotras, Efstathios Velenis, Michel Basset Gissinger, and Gerard Gissinger. Dynamic Friction Models for Road/Tire Longitudinal Interaction. *Vehicle System Dynamics*, 39:189–226, 2003.

[19] M. Burckhardt. *Fahrwerktechnik: Radschlupfregelsysteme*. Germany, 1993.

[20] Yan Chen and Junmin Wang. Adaptive vehicle speed control with input injections for longitudinal motion independent road frictional condition estimation. *Vehicular Technology, IEEE Transactions on*, 60(3):839–848, 2011.

[21] GA Magallan, Cristian H. De Angelo, and Guillermo O. García. Maximization of the traction forces in a 2WD electric vehicle. *Vehicular Technology, IEEE Transactions on*, 60(2):369–380, 2011.

[22] Ehsan Hashemi, Alireza Kasaiezadeh, Saeid Khosravani, Amir Khajepour, Nikolai Moshchuk, and Shih-Ken Chen. Estimation of longitudinal speed robust to road conditions for ground vehicles. *Vehicle System Dynamics*, 54(8):1120–1146, 2016.

[23] Ehsan Hashemi, Saeid Khosravani, Amir Khajepour, Alireza Kasaiezadeh, Shih-Ken Chen, and Bakhtiar Litkouhi. Longitudinal vehicle state estimation using nonlinear and parameter-varying observers. *Mechatronics*, 43:28–39, 2017.

[24] Luis Alvarez, Jingang Yi, Roberto Horowitz, and Luis Olmos. Dynamic friction model-based tire-road friction estimation and emergency braking control. *Journal of dynamic systems, measurement, and control*, 127(1):22–32, 2005.

[25] N Patel, C Edwards, and SK Spurgeon. Tyreroad friction estimationa comparative study. *Proceedings of the Institution of Mechanical Engineers, Part D: Journal of Automobile Engineering*, 222(12):2337–2351, 2008.

[26] Jingang Yi, Luis Alvarez, and Roberto Horowitz. Adaptive emergency braking control with underestimation of friction coefficient. *Control Systems Technology, IEEE Transactions on*, 10(3):381–392, 2002.

[27] Raymond Ghandour, Alessandro Victorino, Moustapha Doumiati, and Ali Charara. Tire/road friction coefficient estimation applied to road safety. In *Control & Automation (MED), 2010 18th Mediterranean Conference on*, pages 1485–1490. IEEE, 2010.

[28] Rajesh Rajamani, Gridsada Phanomchoeng, Damrongrit Piyabongkarn, and Jae Y Lew. Algorithms for real-time estimation of individual wheel tire-road friction coefficients. *Mechatronics, IEEE/ASME Transactions on*, 17(6):1183–1195, 2012.

[29] Yung-Hsiang Judy Hsu. *Estimation and control of lateral tire forces using steering torque*. PhD thesis, Stanford University, 2009.

[30] Moustapha Doumiati, Alessandro Correa Victorino, Ali Charara, and Daniel Lechner. Onboard real-time estimation of vehicle lateral tire–road forces and sideslip angle. *IEEE/ASME Transactions on Mechatronics*, 16(4):601–614, 2011.

[31] Yung-Hsiang Judy Hsu, Shad M Laws, and J Christian Gerdes. Estimation of tire slip angle and friction limits using steering torque. *IEEE Transactions on Control Systems Technology*, 18(4):896–907, 2010.

[32] Xiaojie Gao and Zhuoping Yu. Vehicle sideslip angle estimation by using high gain observer. In *AVEC 9th International Symposium on Advanced Vehicle Control*, pages 509–514, 2008.

[33] Guillaume Baffet, Ali Charara, and Gerald Dherbomez. An observer of tire-road forces and friction for active security vehicle systems. *Mechatronics, IEEE/ASME Transactions on*, 12(6):651–661, 2007.

[34] Guillaume Baffet, Ali Charara, and Daniel Lechner. Estimation of vehicle sideslip, tire force and wheel cornering stiffness. *Control Engineering Practice*, 17(11):1255–1264, 2009.

[35] Moustapha Doumiati, A Victorino, Daniel Lechner, G Baffet, and A Charara. Observers for vehicle tyre/road forces estimation: experimental validation. *Vehicle System Dynamics*, 48(11):1345–1378, 2010.

[36] SJ Julier and JK Uhlmann. A New Extension of the Kalman Filter to Nonlinear Systems. In *The 11th International Symposium on Aerospace/Defense Sensing, Simulation and Controls*, 1997.

[37] Wanki Cho, Jangyeol Yoon, Seongjin Yim, Bonyeong Koo, and Kyongsu Yi. Estimation of tire forces for application to vehicle stability control. *Vehicular Technology, IEEE Transactions on*, 59(2):638–649, 2010.

[38] Yan Wang, David M Bevly, and Shih-ken Chen. Longitudinal tire force estimation with unknown input observer. In *ASME 2012 5th Annual Dynamic Systems and Control Conference joint with the JSME 2012 11th Motion and Vibration Conference*, pages 523–530. American Society of Mechanical Engineers, 2012.

[39] Yan Wang, David M Bevly, and Shih-ken Chen. Lateral tire force estimation with unknown input observer. In *ASME 2012 5th Annual Dynamic Systems and Control Conference joint with the JSME 2012 11th Motion and Vibration Conference*, pages 531–538. American Society of Mechanical Engineers, 2012.

[40] Ehsan Hashemi, Alireza Kasaiezadeh, Amir Khajepour, Nikolai Moshchuk, and Shih-Ken Chen. Robust estimation and experimental evaluation of longitudinal friction forces in ground vehicles. In *ASME 2014 International Mechanical Engineering Congress and Exposition*, pages –. American Society of Mechanical Engineers, 2014.

[41] Fei Sun, Kostyantyn Lolenko, and Joachim Rudolph. Nonlinear observer design for state estimation during antilock braking. *Proceedings of the Institution of Mechanical Engineers, Part I: Journal of Systems and Control Engineering*, 228(2):78–86, 2014.

[42] J. Ryu. *State and Parameter Estimation for Vehicle Dynamics Control using GPS*. PhD thesis, Stanford University, 2004.

[43] Jihan Ryu and J Christian Gerdes. Integrating inertial sensors with global positioning system (gps) for vehicle dynamics control. *Journal of Dynamic Systems, Measurement, and Control*, 126(2):243–254, 2004.

[44] Lars Imsland, Tor A Johansen, Thor I Fossen, HåVard FjæR Grip, Jens C Kalkkuhl, and Avshalom Suissa. Vehicle velocity estimation using nonlinear observers. *Automatica*, 42(12):2091–2103, 2006.

[45] Jay A Farrell, Han-Shue Tan, and Yunchun Yang. Carrier phase gps-aided ins-based vehicle lateral control. *Journal of Dynamic Systems, Measurement, and Control*, 125(3):339–353, 2003.

[46] David M Bevly. Global positioning system (gps): A low-cost velocity sensor for correcting inertial sensor errors on ground vehicles. *Journal of dynamic systems, measurement, and control*, 126(2):255–264, 2004.

[47] David M Bevly, Jihan Ryu, and J Christian Gerde. Integrating ins sensors with gps measurements for continuous estimation of vehicle sideslip, roll, and tire cornering stiffness. *Intelligent Transportation Systems, IEEE Transactions on*, 7(4):483–493, 2006.

[48] Jong-Hwa Yoon and Huei Peng. A cost-effective sideslip estimation method using velocity measurements from two gps receivers. *Vehicular Technology, IEEE Transactions on*, 63(6):2589–2599, 2014.

[49] Jong-Hwa Yoon and Huei Peng. Robust vehicle sideslip angle estimation through a disturbance rejection filter that integrates a magnetometer with gps. *IEEE Transactions on Intelligent Transportation Systems*, 15(1):191–204, 2014.

[50] Y. Fukada. Slip-angle estimation for vehicle stability control. *Vehicle System Dynamics*, 32(4):375–388, 1999.

[51] Aleksander Hac and Melinda D Simpson. Estimation of vehicle side slip angle and yaw rate. Technical report, SAE Technical Paper, 2000.

[52] Lars Imsland, Håvard Fjær Grip, Tor A Johansen, Thor I Fossen, Jens C Kalkkuhl, and Avshalom Suissa. Nonlinear observer for vehicle velocity with friction and road bank angle adaptation-validation and comparison with an extended kalman filter. Technical report, SAE Technical Paper, 2007.

[53] M. Satria and M. Best. Comparison between Kalman Filter and Robust Filter for Vehicle Handling Dynamics State Estimation. In *SAE Technical Paper 2002-01-1185*, 2002.

[54] T. a. Wenzel, K. J. Burnham, M. V. Blundell, and R. a. Williams. Dual Extended Kalman Filter for Vehicle State and Parameter Estimation. *Vehicle System Dynamics*, 44(2):153–171, 2006.

[55] L. Tong. An Approach for Vehicle State Estimation Using Extended Kalman Filter. In *Syst. Simul. Sci. Comput.*, volume 1, pages 56–63, 2012.

[56] Xiaoyu Huang and Junmin Wang. Robust Sideslip Angle Estimation for Lightweight Vehicles Using Smooth Variable Structure Filter. In *ASME Dynamic Systems and Control Conference*, pages 1–8, 2013.

[57] S Antonov, A Fehn, and A Kugi. Unscented kalman filter for vehicle state estimation. *Vehicle System Dynamics*, 49(9):1497–1520, 2011.

[58] Mark Wielitzka, Matthias Dagen, and Tobias Ortmaier. State estimation of vehicle's lateral dynamics using unscented kalman filter. In *Decision and Control (CDC), 2014 IEEE 53rd Annual Conference on*, pages 5015–5020. IEEE, 2014.

[59] Xiangwen Zhang, Yong Xu, Ming Pan, and Fenghua Ren. A vehicle ABS adaptive sliding-mode control algorithm based on the vehicle velocity estimation and tyre/road friction coefficient estimations. *Vehicle System Dynamics*, 52(4):475–503, 2014.

[60] Fei Sun, Xuhui Huang, Joachim Rudolph, and Kostyantyn Lolenko. Vehicle state estimation for anti-lock control with nonlinear observer. *Control Engineering Practice*, 43:69–84, 2015.

[61] Kanghyun Nam, Hiroshi Fujimoto, and Yoichi Hori. Lateral stability control of in-wheel-motor-driven electric vehicles based on sideslip angle estimation using lateral tire force sensors. *Vehicular Technology, IEEE Transactions on*, 61(5):1972–1985, 2012.

[62] Alexander A Brown and Sean N Brennan. Lateral vehicle state and environment estimation using temporally previewed mapped lane features. *IEEE Transactions on Intelligent Transportation Systems*, 16(3):1601–1608, 2015.

[63] M Gadola, D Chindamo, M Romano, and F Padula. Development and validation of a kalman filter-based model for vehicle slip angle estimation. *Vehicle System Dynamics*, 52(1):68–84, 2014.

[64] Lars Imsland, Tor A Johansen, Thor I Fossen, HåVard FjæR Grip, Jens C Kalkkuhl, and Avshalom Suissa. Vehicle velocity estimation using nonlinear observers. *Automatica*, 42(12):2091–2103, 2006.

[65] Ling-Yuan Hsu and Tsung-Lin Chen. Vehicle full-state estimation and prediction system using state observers. *Vehicular Technology, IEEE Transactions on*, 58(6):2651–2662, 2009.

[66] Hongtei Eric Tseng. Dynamic estimation of road bank angle. *Vehicle System Dynamics*, 36(4-5):307–328, 2001.

[67] Jihan Ryu and J Christian Gerdes. Estimation of vehicle roll and road bank angle. In *American Control Conference, 2004. Proceedings of the 2004*, volume 3, pages 2110–2115. IEEE, 2004.

[68] Lin-Hui Zhao, Zhi-Yuan Liu, and Hong Chen. Sliding mode observer for vehicle velocity estimation with road grade and bank angles adaptation. In *Intelligent Vehicles Symposium, 2009 IEEE*, pages 701–706. IEEE, 2009.

[69] Lghani Menhour, Daniel Lechner, and Ali Charara. Design and experimental validation of linear and nonlinear vehicle steering control strategies. *Vehicle System Dynamics*, 50(6):903–938, 2012.

[70] Havard Faer Grip, Lars Imsland, Tor A Johansen, Jens C Kalkkuhl, and Avshalom Suissa. Vehicle sideslip estimation: Design, implementation, and experimental validation. *IEEE control systems*, 29(5):36–52, 2009.

[71] Håvard Fjær Grip, Lars Imsland, Tor Johansen, Jens C Kalkkuhl, Avshalom Suissa, et al. Estimation of road inclination and bank angle in automotive vehicles. In *American Control Conference, 2009. ACC'09.*, pages 426–432. IEEE, 2009.

[72] Jin-oh Hahn, Rajesh Rajamani, S You, and K Lee. Road bank angle estimation using disturbance observer. In *Proceedings of AVEC 6th International Symposium*, 2002.

[73] Lars Imsland, Tor A Johansen, Håvard Fjær Grip, and Thor I Fossen. On non-linear unknown input observers–applied to lateral vehicle velocity estimation on banked roads. *International Journal of Control*, 80(11):1741–1750, 2007.

[74] Jihwan Kim, Hyeongcheol Lee, and Seibum Choi. A robust road bank angle estimation based on a proportional–integral h filter. *Proceedings of the Institution of Mechanical Engineers, Part D: Journal of automobile engineering*, page 0954407011430919, 2012.

[75] Christopher R Carlson and J Christian Gerdes. Optimal rollover prevention with steer by wire and differential braking. In *ASME 2003 International Mechanical Engineering Congress and Exposition*, pages 345–354. American Society of Mechanical Engineers, 2003.

[76] Jihan Ryu, Eric J Rossetter, and J Christian Gerdes. Vehicle sideslip and roll parameter estimation using gps. In *Proceedings of the AVEC International Symposium on Advanced Vehicle Control*, 2002.

[77] Ling-Yuan Hsu and Tsung-Lin Chen. Estimating road angles with the knowledge of the vehicle yaw angle. *Journal of dynamic systems, measurement, and control*, 132(3):031004, 2010.

[78] Håvard Fjær Grip, Lars Imsland, Tor A Johansen, Thor I Fossen, Jens C Kalkkuhl, and Avshalom Suissa. Nonlinear vehicle side-slip estimation with friction adaptation. *Automatica*, 44(3):611–622, 2008.

[79] Seung-Han You, Jin-Oh Hahn, and Hyeongcheol Lee. New adaptive approaches to real-time estimation of vehicle sideslip angle. *Control Engineering Practice*, 17(12):1367–1379, 2009.

[80] ISO. Road vehicles – vehicle dynamics and road-holding ability – vocabulary, 2011.

[81] Ehsan Hashemi, Reza Zarringhalam, Amir Khajepour, William Melek, Alireza Kasaiezadeh, and Shih-Ken Chen. Real-time estimation of the road bank and grade angles with unknown input observers. *Vehicle System Dynamics*, 55(5):648–667, 2017.

[82] Mohamed Darouach, Michel Zasadzinski, and Shi Jie Xu. Full-order observers for linear systems with unknown inputs. *IEEE transactions on automatic control*, 39(3):606–609, 1994.

[83] Maria Elena Valcher. State observers for discrete-time linear systems with unknown inputs. *Automatic Control, IEEE Transactions on*, 44(2):397–401, 1999.

[84] Shreyas Sundaram and Christoforos N Hadjicostis. Delayed observers for linear systems with unknown inputs. *Automatic Control, IEEE Transactions on*, 52(2):334–339, 2007.

[85] Andrea Cristofaro and Tor Arne Johansen. Fault tolerant control allocation using unknown input observers. *Automatica*, 50(7):1891–1897, 2014.

[86] CL Robinson and PR Kumar. Sending the most recent observation is not optimal in networked control: Linear temporal coding and towards the design of a control specific transport protocol. In *Decision and Control, 2007 46th IEEE Conference on*, pages 334–339. IEEE, 2007.

[87] Shreyas Sundaram and Christoforos N Hadjicostis. Partial state observers for linear systems with unknown inputs. *Automatica*, 44(12):3126–3132, 2008.

[88] Saeed Ahmadizadeh, Jafar Zarei, and Hamid Reza Karimi. Robust unknown input observer design for linear uncertain time delay systems with application to fault detection. *Asian Journal of Control*, 16(4):1006–1019, 2014.

[89] E Hashemi, M Pirani, A Khajepour, B Fidan, A Kasaiezadeh, SK Chen, and B Litkouhi. Integrated estimation structure for the tire friction forces in ground vehicles. In *Advanced Intelligent Mechatronics (AIM), 2016 IEEE International Conference on*, pages 1657–1662. IEEE, 2016.

[90] M Gadola, D Chindamo, M Romano, and F Padula. Development and validation of a kalman filter-based model for vehicle slip angle estimation. *Vehicle System Dynamics*, 52(1):68–84, 2014.

[91] Ehsan Hashemi, Mohamamd Pirani, Amir Khajepour, Alireza Kasaiezadeh, Shih-Ken Chen, and Bakhtiar Litkouhi. Corner-based estimation of tire forces and vehicle velocities robust to road conditions. *Control Engineering Practice*, 61:28–40, 2017.

[92] Gene F Franklin, J. David Powell, and Michael L Workman. *Digital Control of Dynamic Systems*. Addison Wesley Longman, Menlo Park, 1998.

[93] Alan S Willsky. On the invertibility of linear systems. *IEEE Transactions on Automatic Control*, 19(3):272–274, 1974.

[94] Shih-Ken Chen, Amir Khajepour, William Melek, Reza Zarringhalam, and Ehsan Hashemi. Detection and reconstruction of suspension height sensor faults, 2016. US Pending Patent.

[95] Milad Jalali, Amir Khajepour, Shih-ken Chen, and Bakhtiar Litkouhi. Integrated stability and traction control for electric vehicles using model predictive control. *Control Engineering Practice*, 54:256–266, 2016.

[96] Milad Jalaliyazdi. Integrated vehicle stability control and power distribution using model predictive control. 2016.

[97] Saïd Mammar, Sébastien Glaser, and Mariana Netto. Vehicle lateral dynamics estimation using unknown input proportional-integral observers. In *American Control Conference, 2006*, pages 6–pp. IEEE, 2006.

[98] Ai-Guo Wu, Guang-Ren Duan, and Yan-Ming Fu. Generalized pid observer design for descriptor linear systems. *Systems, Man, and Cybernetics, Part B: Cybernetics, IEEE Transactions on*, 37(5):1390–1395, 2007.

[99] Jing Yang Peng and Xiong Biao Chen. Integrated pid-based sliding mode state estimation and control for piezoelectric actuators. *Mechatronics, IEEE/ASME Transactions on*, 19(1):88–99, 2014.

[100] Sanghyun Hong, Tim Smith, Francesco Borrelli, and J Karl Hedrick. Vehicle inertial parameter identification using extended and unscented kalman filters. In *Intelligent Transportation Systems-(ITSC), 2013 16th International IEEE Conference on*, pages 1436–1441, Hague, Netherlands, 2013. IEEE.

[101] Sanghyun Hong, Chankyu Lee, Francesco Borrelli, and J Karl Hedrick. A novel approach for vehicle inertial parameter identification using a dual kalman filter. *Intelligent Transportation Systems, IEEE Transactions on*, 16(1):151–161, 2015.

[102] Editor Haykin, Simon. *Kalman Filtering and Neural Networks*, volume 47. John Wiley & Sons, Inc., New York, 2004.

[103] Leonard M Silverman and HE Meadows. Controllability and observability in time-variable linear systems. *SIAM Journal on Control*, 5(1):64–73, 1967.

[104] Roland Tóth. *Modeling and identification of linear parameter-varying systems*, volume 403. Springer, 2010.

[105] Rudolph Van Der Merwe and EA Wan. Efficient Derivative-Free Kalman Filters for Online Learning. In *European Symposium on Artificial Neural Networks, ESANN*, pages 205–210, 2001.

[106] Fredrik Gustafsson and Gustaf Hendeby. Some Relations Between Extended and Unscented Kalman Filters. *Signal Processing, IEEE Transactions on*, 60(2):545–555, 2012.

[107] Ansgar Rehm. Estimation of vehicle roll angle. In *Communications, Control and Signal Processing (ISCCSP), 2010 4th International Symposium on*, pages 1–4. IEEE, 2010.

[108] Changsun Ahn, Huei Peng, and Hongtei Eric Tseng. Robust estimation of road frictional coefficient. *Control Systems Technology, IEEE Transactions on*, 21(1):1–13, 2013.

[109] Rongrong Wang and Junmin Wang. Tire–road friction coefficient and tire cornering stiffness estimation based on longitudinal tire force difference generation. *Control Engineering Practice*, 21(1):65–75, 2013.

[110] Yan Wang and David Bevly. Longitudinal Vehicle State Estimation; General Motors Summary Report. Technical report, General Motors Summary Report, 2010.

[111] Pascal Gahinet, Pierre Apkarian, and Mahmoud Chilali. Affine Parameter-Dependent Lyapunov Functions and Real Parametric Uncertainty. *IEEE Transactions on Automatic Control*, 41(3):436–442, 1996.

[112] Johan Lofberg. Yalmip: A toolbox for modeling and optimization in matlab. In *Computer Aided Control Systems Design, 2004 IEEE International Symposium on*, pages 284–289. IEEE, 2004.

[113] Mohammad Pirani, Ehsan Hashemi, Amir Khajepour, Baris Fidan, Alireza Kasaiezadeh, Shih-Ken Chen, and Bakhtiar Litkouhi. Resilient corner-based vehicle velocity estimation. *IEEE Transactions on Control Systems Technology*, 2017.

[114] Alireza Kasaiezadeh, Ehsan Hashemi, Amir Khajepour, Bakhtiar Litkouhi, and Shih-Ken Chen. Corner-based longitudinal speed estimation, 2016. US Pending Patent.

[115] A. Czornik, A. Nawrat, M. Niezabitowski, and A. Szyda. On the lyapunov and bohl exponent of time-varying discrete linear system. *20th Mediterranean Conference on Control Automation (MED)*, pages 194–197, 2012.

[116] T. Berger. Bohl exponent for time-varying linear differential-algebraic equations. *Int. J. Control*, 85:1433–1451, 2012.

[117] H. Khalil. *Nonlinear systems*. Prentice hall, 1996.

[118] Arthur Earl Bryson and Yu-Chi Ho. *Applied optimal control: optimization, estimation and control*. Taylor Francis, Levittown, PA, 1975.

[119] Panqanamala Ramana Kumar and Pravin Varaiya. *Stochastic systems: estimation, identification and adaptive control*. Prentice-Hall, Inc., New York, 1986.

[120] BDO Anderson and John B Moore. Detectability and stabilizability of time-varying discrete-time linear systems. *SIAM Journal on Control and Optimization*, 19(1):20–32, 1981.

[121] Robert F Stengel. *Optimal control and estimation*. Courier Corporation, New York, 2012.

[122] Bernard Delyon. A note on uniform observability. *Automatic Control, IEEE Transactions on*, 46(8):1326–1327, 2001.

[123] Vibhor L Bageshwar, Demoz Gebre-Egziabher, William L Garrard, and Tryphon T Georgiou. Stochastic observability test for discrete-time kalman filters. *Journal of Guidance, Control, and Dynamics*, 32(4):1356–1370, 2009.

[124] E Hashemi, M Pirani, B Fidan, A Khajepour, SK Chen, and B Litkouhi. Distributed robust vehicle state estimation. In *IEEE Intelligent Vehicles Symposium (IV)*, pages – . IEEE, 2017.

[125] Changsun Ahn, Huei Peng, and H.E. Tseng. Robust Estimation of Road Friction Coefficient. In *American Control Conference (ACC)*, number 3, pages 3948–3953, 2011.

[126] Ehsan Hashemi, Mohammad Pirani, Amir Khajepour, and Alireza Kasaiezadeh. A comprehensive study on the stability analysis of vehicle dynamics with pure/combined-slip tyre models. *Vehicle system dynamics*, 54(12):1736–1761, 2016.

Appendix A

Parameter Identification and Proofs

LuGre parameter identification

The LuGre tire parameters are obtained by fitting to the experimental tire curves with the Nonlinear Least Square method and the result is shown in Fig. A.1 for the normal force of $F_z = 4.5[kN]$ on a dry road. Identified parameters are also listed in Section 5.5

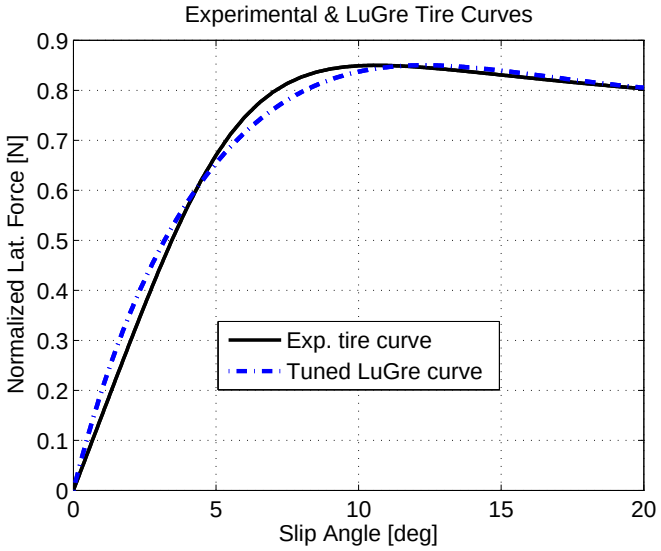

Figure A.1: Tuned lateral LuGre tire curve based on tire data from CarSim

Detectability and stabilizability

Definition 1. *The pair $[A_k, C_k]$ in the linear time-varying discrete-time system with state update $x_{k+1} = A_k x_k + B_k u_k$ and output equation $y_k = C_k x_k$ is uniformly detectable if $\exists 0 \leq c_1 \leq 1, c_2 \in \mathbb{R}^+$ and $q, k_2 \geq 0$, such that in case $||\phi_{k_1+q,k_1}\vartheta|| \geq c_1||\vartheta||$ for some ϑ, k_1, then $\vartheta^T \mathbb{V}(k_1, k_2)\vartheta \geq c_2 \vartheta^T \vartheta$, which necessitates the observability grammian $\mathbb{V}(k_1, k_2)$ to be $\mathbb{V}(k_1, k_2) \geq d_1 I > 0$ for some d_1 [120]:*

$$\mathbb{V}(k_1, k_2) = \sum_{k=k_1}^{k_2} \phi_{k,k_1}^T C_k^T C_k \phi_{k,k_1}, \tag{A1}$$

where $\phi_{i,j} = \phi_{i,i-1}\phi_{i-1,j}$ and $\phi_{i+1,i} = A_i$ as the state transition matrices for $i \geq j$. In addition, the pair $[A_k, B_k]$ in the linear time-varying discrete-time system (4.17) without process and measurement noise effect is stabilizable if $\exists 0 \leq c_1 \leq 1, c_2 \in \mathbb{R}^+$ and $q, k_2 \geq 0$, such that in case $||\phi_{k2,k2-q}\vartheta|| \geq c_1||\vartheta||$ for some ϑ, then $\vartheta^T \mathbb{W}(k_1, k_2 - 1)\vartheta \geq c_2 \vartheta^T \vartheta$, which necessitates the controllability grammian $\mathbb{W}(k_1, k_2 - 1)$ to be full rank

$$\mathbb{W}(k_1, k_2 - 1) = \sum_{k=k_1}^{k_2-1} \phi_{k_2,k+1} B_k B_k^T \phi_{k_2,k+1}^T, \tag{A2}$$

Bounded error covariance for the Kalman filter:

This characteristic for the time-invariant KF has been proved before, but provided here for convenience. Detectability condition on (A, C) leads to a linear estimator with matrix K^*:

$$x_{k+1|k}^* = A x_{k|k-1}^* + K^*(y_k - C x_{k|k-1}^*), \tag{A3}$$

where $(A - K^*C)$ is stable. Thus, the error covariance matrix for such estimator is defined by $\bar{P}_{k+1|k}^* \triangleq \mathbb{E}\left[(x_{k+1} - \hat{x}_{k+1|k}^*)(x_{k+1} - \hat{x}_{k+1|k}^*)^T\right]$ that yields::

$$\bar{P}_{k+1|k}^* = (A - K^*C)\bar{P}_k^*(A - K^*C)^T + K^* R K^{*T}, \tag{A4}$$

which can be written as:

$$\bar{P}^*_{k+1|k} = (A - K^*C)^{k+1}\bar{P}^*_{0|-1}\left((A - K^*C)^{k+1}\right)^T + \sum_{i=0}^{k}(A - K^*C)^i(K^*RK^{*T} + Q)\left((A - K^*C)^i\right)^T \tag{A5}$$

The first term vanishes and the second term is also bounded because of the stability of $(A-K^*C)$. Therefore, the error covariance $\bar{P}^*_{k+1|k}$ of such linear estimator is bounded. This results in bounded error covariance $\bar{P}_k$ for the Kalman estimator because of the optimality of the KF.

Defining $\mathcal{M}_{k+1}$ and $\mathcal{N}_{k+1}$ for completely uncertain initial covariance/states [123]:

The initial $\mathcal{M}_1, \mathcal{N}_1$ are attainable by the initial measurement error covariance R_0 as $\Xi_0^T\Xi_0 = \bar{R}_0$, which yields the projector Φ of a vector onto the orthogonal complement of the range space Σ :

$$\begin{aligned}
\Sigma_0 &= C_0^T\Xi_0^{-1} \\
\Phi_0 &= I - \Sigma_0(\Sigma_0^T\Sigma_0)^*\Sigma_0^T \\
X_0X_0^T &= \Phi_0 \\
\mathcal{M}_1 &= A_0X_0X_0^TA_0^T \\
\mathcal{N}_1 &= \bar{Q}_0 + A_0\Sigma_0((\Sigma_0^T\Sigma_0)^*)^2\Sigma_0^TA_0^T,
\end{aligned} \tag{A6}$$

where $(.)^*$ represents pseudo inverse of the matrix $(.)$ and full rank factorization of Φ_0 is denoted by X_0. The matrix $\mathcal{M}_{k+1}$ is then defined using the fresh C_k and the measurement noise R_k as the following procedure:

$$\begin{aligned}
\Xi_k^T\Xi_k &= \bar{R}_k + C_k\mathcal{N}C_k^T \\
\Sigma_k &= X_{0,k-1}^T\phi_{k,0}^TC_k^T\Xi_k^{-1} \\
\Phi_k &= I - \Sigma_k(\Sigma_k^T\Sigma_k)^*\Sigma_K^T \\
X_kX_k^T &= \Phi_k \\
\mathcal{M}_{k+1} &= \phi_{k,0}X_{0,k}X_{0,k}^T\phi_{k,0}^T
\end{aligned} \tag{A7}$$

in which X_k is the full rank factorization of Φ_k and $X_{0,k} \triangleq X_0 X_1 ... X_k$. Employing the condition $\lambda_{max}(\mathcal{M}_f) = 0$ for a finite time, $\mathcal{N}_{k+1}$ is related to $\mathcal{N}_k$ as in (5.31). In addition, the $\mathcal{S}_{k+1}$ matrix in the simplified Riccati equation $\bar{P}_{k+1|k} = \mathcal{N}_{k+1} + \mathcal{S}_{k+1}$ can be written as:

$$\begin{aligned}
\mathcal{S}_{k+1} = {} & A_k \mathcal{S}_k A_k^T - A_k \mathcal{N}_k C_k^T \Xi_k^{-1} \left(\frac{\mathcal{T}_{k,1}}{\psi} + ... \right) \Xi_k^{-T} C_k \mathcal{N}_k A_k^T \\
& - A_k \mathcal{N}_k C_k^T \Xi_K^{-1} \left(I - \frac{\mathcal{T}_{k,1}}{\psi} + ... \right) \Xi_k^{-T} C_k \mathcal{S}_k A_k^T \\
& - A_k \mathcal{S}_k C_k^T \Xi_K^{-1} \left(I - \frac{\mathcal{T}_{k,1}}{\psi} + ... \right) \Xi_k^{-T} C_k \mathcal{N}_k A_k^T \\
& - A_k \mathcal{S}_k C_k^T \Xi_K^{-1} \left(I - \frac{\mathcal{T}_{k,1}}{\psi} + ... \right) \Xi_k^{-T} C_k \mathcal{S}_k A_k^T
\end{aligned} \tag{A8}$$